UNIVERSIDADE ESTADUAL DE CAMPINAS
Faculdade de Engenharia Civil, Arquitetura e Urbanismo

Thiago Dias dos Santos

Adaptive Mesh Refinement Applied to Marine Ice Sheet Simulation

Malhas Adaptativas Aplicadas em Simulação Numérica de Manto de Gelo Marinho

CAMPINAS
2019

Thiago Dias dos Santos

Adaptive Mesh Refinement Applied to Marine Ice Sheet Simulation

Malhas Adaptativas Aplicadas em Simulação Numérica de Manto de Gelo Marinho

Thesis presented to the School of Civil Engineering, Architecture and Urban Design of the University of Campinas in partial fulfillment of the requirements for the degree of Doctor in Civil Engineering, in the area of Structures and Geotechnics.

Tese apresentada à Faculdade de Engenharia Civil, Arquitetura e Urbanismo da Universidade Estadual de Campinas como parte dos requisitos para a obtenção do título de Doutor em Engenharia Civil, na área de Estruturas e Geotécnica.

Supervisor/Orientador: Prof. Dr. Philippe Remy Bernard Devloo

ESTE EXEMPLAR CORRESPONDE À VERSÃO FINAL DA TESE DEFENDIDA PELO ALUNO THIAGO DIAS DOS SANTOS, E ORIENTADA PELO PROF. DR. PHILIPPE REMY BERNARD DEVLOO.

CAMPINAS
2019

Ficha catalográfica
Universidade Estadual de Campinas
Biblioteca da Área de Engenharia e Arquitetura
Rose Meire da Silva - CRB 8/5974

Sa59a

Santos, Thiago Dias dos, 1984-
Adaptive mesh refinement applied to marine ice sheet simulation / Thiago Dias dos Santos. – Campinas, SP : [s.n.], 2019.

Orientador: Philippe Remy Bernard Devloo.
Tese (doutorado) – Universidade Estadual de Campinas, Faculdade de Engenharia Civil, Arquitetura e Urbanismo.

1. Geração numérica de malhas (Análise numérica). 2. Método dos elementos finitos. 3. Geleiras. 4. Glaciologia. I. Devloo, Philippe Remy Bernard, 1958-. II. Universidade Estadual de Campinas. Faculdade de Engenharia Civil, Arquitetura e Urbanismo. III. Título.

Informações para Biblioteca Digital

Título em outro idioma: Malhas adaptativas aplicadas em simulação numérica de manto de gelo marinho
Palavras-chave em inglês:
Mesh generation
Finite element method
Glaciers
Glaciology
Área de concentração: Estruturas e Geotécnica
Titulação: Doutor em Engenharia Civil
Banca examinadora:
Philippe Remy Bernard Devloo [Orientador]
José Luiz Antunes de Oliveira e Sousa
Euclides de Mesquita Neto
Jandyr de Menezes Travassos
Fabrício Simeoni de Sousa
Data de defesa: 27-03-2019
Programa de Pós-Graduação: Engenharia Civil

Identificação e informações acadêmicas do(a) aluno(a)
- ORCID do autor: https://orcid.org/0000-0001-8257-1314
- Currículo Lattes do autor: http://lattes.cnpq.br/3618128074442916

UNIVERSIDADE ESTADUAL DE CAMPINAS
Faculdade de Engenharia Civil, Arquitetura e Urbanismo

Thiago Dias dos Santos

Adaptive Mesh Refinement Applied to Marine Ice Sheet Simulation

Malhas Adaptativas Aplicadas em Simulação Numérica de Manto de Gelo Marinho

Tese de Doutorado aprovada pela Banca Examinadora, constituída por:

Prof. Dr. Philippe Remy Bernard Devloo
Presidente e Orientador / FEC/UNICAMP

Prof. Dr. José Luiz Antunes de Oliveira e Sousa
FEC/UNICAMP

Prof. Dr. Euclides de Mesquita Neto
FEM/UNICAMP

Prof. Dr. Jandyr de Menezes Travassos
Universidade Federal do Pará

Prof. Dr. Fabrício Simeoni de Sousa
ICMC/USP

A Ata da defesa com as respectivas assinaturas dos membros encontra-se no SIGA/Sistema de Fluxo de Dissertação/Tese e na Secretaria do Programa da Unidade.

Campinas, 27 de março de 2019

Aos meus avós:
Iracy e Vicente, Aparecida e Pedro.

Acknowledgements

This thesis has the support of many minds and hands. Special thanks to Flávia, my wife, to whom I owe emotional, physical and philosophical support; to my parents, Benedita and Gervazio, for the huge support in all my academic life; to my brothers, Jack and Kevin, and Felipe, for the funny Friends' (and Stranger Things') sessions on weekends; to Phil, for all patience and critical reviews of my steps; to Jefferson C. Simões, for showing me the curious and beautiful field of Glaciology; in fact, Jefferson is the co-supervisor of this thesis; to Luiz Vieira, the all-situation friend (whose MacBook I still use to write these lines); to Luiz Carlos, the wizard of linux systems (yes, the Intel's compiler has several tricks); to Eric Larour, our first JPL/UCI/ISSM contact; to Mathieu and Hélène (the French guys whose lifestyles are admirable), for all technical and financial (and English) supports; to my colleagues at LabMeC and Galileu laboratories, for several conversations and coffee times; and to Kowalski, the best custom-machine that I built to compile C++ codes (faster and cheaper than several HPC nodes).

I also would like to thank FEC/UNICAMP, Galileu laboratory and ESS/UCI, for the computational resources used (daily, nightly and "weekendly") during this work. Also thanks to FEC/UNICAMP, CPC/UFRGS and ESS/UCI for all supports.

This thesis was financed in part by the Conselho Nacional de Desenvolvimento Científico e Tecnológico - Brasil (CNPq) - Finance Code 140186/2015-8; by FAEPEX/UNICAMP; and by a financial support under a contract with National Aeronautics and Space Administration (NASA) Cryospheric Sciences Program (no. NNX14AN03G).

All my thanks to God, for the life, and for giving us the desire to discover the Universe.

Resumo

Projeções acuradas da evolução de mantos de gelo marinho e suas contribuições ao aumento do nível dos mares sob mudanças climáticas requerem alta resolução de malha/grade em modelos numéricos para capturar corretamente processos físicos fundamentais, tais como a evolução da linha de aterramento, a região onde o gelo apoiado sobre o embasamento rochoso começa a flutuar. A evolução da linha de aterramento desempenha um papel importante na dinâmica dos mantos de gelo marinho, já que exerce um controle fundamental sobre a estabilidade do manto de gelo apoiado. A modelagem numérica da dinâmica da linha de aterramento requer recursos computacionais significativos, pois a exatidão de sua posição depende da resolução da malha ou grade. Uma técnica numérica que contribui para a exatidão com custo computacional reduzido é o refinamento adaptativo de malhas. Apresentamos aqui a implementação de malhas adaptativas no Ice Sheet System Model para simular a dinâmica da linha de aterramento sob dois diferentes benchmarks: MISMIP3d e MISMIP+. Testamos diferentes critérios de refinamento baseados em: (a) distância ao redor da linha de aterramento, (b) estimador de erro a posteriori, o estimador de erro Zienkiewicz-Zhu e (c) diferentes combinações de (a) e (b). Em ambos benchmarks, os estimadores de erro apresentam valores altos em torno da linha de aterramento. Particularmente para o MISMIP+, o estimador também apresenta valores altos na parte apoiada do manto de gelo, seguindo as principais feições da geometria do leito rochoso. O emprego do estimator de erro orienta o procedimento de refinamento de forma que o desempenho das malhas adaptativas é otimizado. Nossos resultados mostram que o tempo computacional utilizando malhas adaptativas depende da acurácia requerida, mas em todos os casos, é significativamente menor em comparação com o tempo necessário ao empregar malhas uniformemente refinadas. Concluímos que o emprego de malhas adaptativas em simulação numérica de mantos de gelo marinho sem um estimador de erro associado deve ser evitado, especialmente em mantos de gelo reais em que o leito rochoso apresenta feições mais complexas.

Abstract

Accurate projections of the evolution of marine ice sheets and their contribution to sea level rise in a changing climate require a fine mesh/grid resolution in ice sheet models to correctly capture fundamental physical processes, such as the evolution of the grounding line, the region where grounded ice starts to float. The evolution of the grounding line indeed plays a major role in marine ice sheet dynamics, as it is a fundamental control on marine ice sheet stability. Numerical modeling of a grounding line requires significant computational resources since the accuracy of its position depends on grid or mesh resolution. A technique that improves accuracy with reduced computational cost is the adaptive mesh refinement approach. We present here the implementation of the adaptive mesh refinement technique in the parallel finite element Ice Sheet System Model to simulate grounding line dynamics under two different benchmarks: MISMIP3d and MISMIP+. We test different refinement criteria: (a) distance around the grounding line, (b) a posteriori error estimator, the Zienkiewicz–Zhu error estimator, and (c) different combinations of (a) and (b). In both benchmarks, the error estimator presents high values around the grounding line. In the MISMIP+ setup, this estimator also presents high values in the grounded part of the ice sheet, following the complex shape of the bedrock geometry. The error estimator helps guide the refinement procedure such that the mesh adaptivity performance is improved. Our results show that computational time with adaptive mesh depends on the required accuracy, but in all cases, it is significantly shorter than for uniformly refined meshes. We conclude that the use of adaptive mesh refinement in marine ice sheet simulations without an associated error estimator should be avoided, especially for real glaciers that have a complex bed geometry.

List of Figures

List of Tables

Contents

Chapter 1

Introduction

1.1 The Cryosphere and the climate system

Approximately, 10% of the Earth's surface is covered by water in solid state: snow, freshwater, ice in lakes and rivers, sea ice, mountain glaciers and ice caps, ice sheets and subsoil ice (permafrost). This entire set is known as 'Cryosphere'[1]. The largest bulk is present in Antarctica Ice Sheet, a continent with $24.7 \times 10^6\ km^3$ of ice volume[2], meaning $60.9\ m$ of sea level rise[3], followed by the Greenland Ice Sheet, the largest island on the Earth, with an ice volume equal to $2.9 \times 10^6\ km^3$ ($7.1\ m$ of sea level rise) [91, p.342]. The remaining ice present on the Earth means $\sim$ 3% of the Cryosphere ($\sim 0.9 \times 10^6\ km^3$ of ice volume). Considering only glaciers and ice caps, the equivalent sea level rise is estimated between $0.15 - 0.37\ m$ [91, p.342]. Figure 1.1 shows the spatial view and the time scales of the cryospheric components.

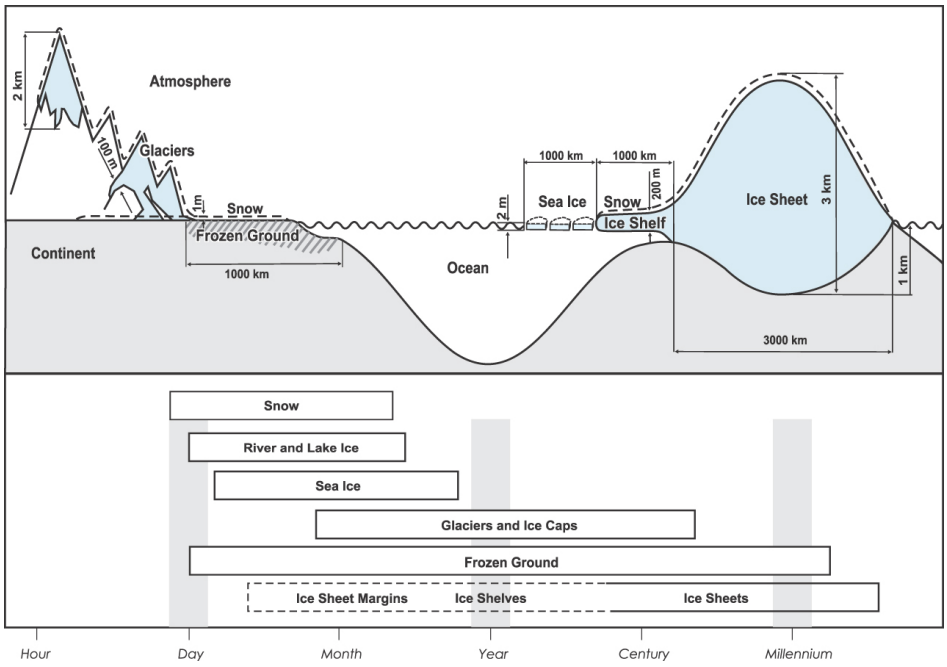

Figure 1.1: Spatial and temporal scales of the Cryosphere's components. From [91, p.341].

[1] 'Cryos', from the Greek, means glacial or cold [143].

[2] Excluding the attached ice shelves.

[3] For $3.62 \times 10^8\ km^2$ of oceanic area, and $917\ kg/m^3$ and $1,028\ kg/m^3$ for the ice and seawater densities, resp.

How does a glacier flow? Glaciers and ice sheets are masses of ice that deform and slide under the gravitational force. In their upper portions, called 'accumulation zone', they accumulate ice mass due to the annual snow precipitation. In their lower portions, the 'ablation zone', they lose ice mass due to melting, sublimation and/or iceberg calving[4]. Where there is no accumulation neither ablation is called as the Equilibrium Line Altitude (ELA). The ice flows from the upper part to the lowest point following the (negative) gradient of the ice surface. A schematic view of the flows of glaciers and ice sheets are presented in Figure 1.2.

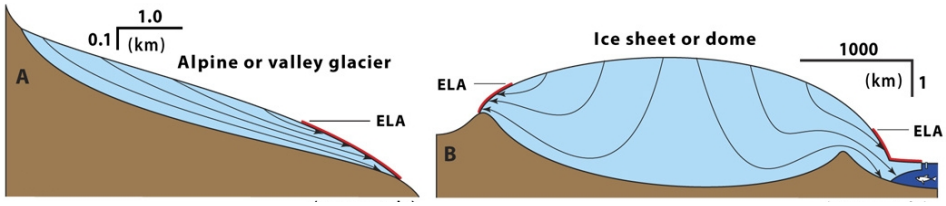

Figure 1.2: (A) Alpine glacier and (B) ice sheet with terrestrial and marine ice margins. The ice flows are represented by the arrows. The ablation zone is represented in red. ELA is the Equilibrium Line Altitude. Adapted from [71] (here we are using only the upper part of the original figure). ©The Authors, some rights reserved; exclusive licensee American Association for the Advancement of Science. Distributed under a Creative Commons Attribution Non-Commercial License 4.0 (CC BY-NC) http://creativecommons.org/licenses/by-nc/4.0/.

The Cryosphere is an important and active component of the Earth's climate system due to the energy and mass exchanges carried out with the atmosphere and oceans. Figure 1.3 highlights the interactions between the Cryosphere and the climate system. The cryospheric components are extremely sensitive to climatic variations (e.g. [95, 30, 131, 140]), and in its turn, changes in these components may affect the atmospheric and ocean circulation patterns [26, 83]. Recently, an increasing in ice discharges and ice front retractions of glaciers have been reported [145, 159, 142, 128], and a number of studies correlate these recent changes with atmospheric temperature increasing or with relatively warmer ocean circulations [78, 84, 121, 131].

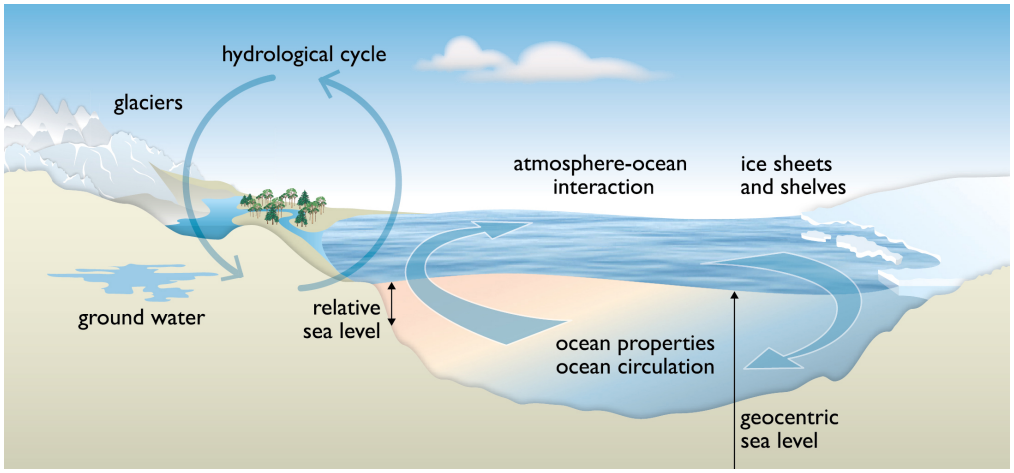

Figure 1.3: The Cryosphere interactions with the Earth's climate system. From [24, p.1143].

[4]Ablation is the process by which snow, ice or water is lost by a glacier, floating ice or seasonal snow cover. It includes melting, evaporation, detachment, wind erosion and avalanches [143].

1.2 The risk: sea level rise

The projections of impacts, vulnerabilities and adaptations due to the climate change has been a continuous effort of the scientific community since the 1st Intergovernmental Panel on Climate Change report (IPPC AR1/1990). Among several impacts, the sea level rise is a great concern: among the 600 million people living in coastal areas below of 10 m of altitude, about 150 million live in regions up to 1 m above the sea level, and the cost of damage and adaptation in these areas are enormous [93, 63, 69]. Any planning of adaptation and risk management depend heavily on the projections of the sea level rise, as well as the impacts associated with each projection [107]. However, these projections present large variability because there are several difficulties to accurately estimate the contributions from the Greenland and mainly from the Antarctica [108]. In particular, the collapse of the West Antarctica Ice Sheet (WAIS) represents a potential fast sea level rise [12, 58, 43] by the end of the 21st century, above the upper limit presented by the latest IPCC report (AR5) [79].

The collapse of WAIS is related to the Marine Ice Sheet Instability hypothesis (MISI). Marine ice sheets are those that rest on bedrock below of sea level. Ice shelves are commonly attached to these ice sheets. Confined ice shelves[5] may hold back ice sheets, 'buttressing' them. The ice flows from the grounded part to the ocean, where the ice mass is lost by melting and iceberg calving. The point where the grounded ice begins to float is called 'grounding line'. Figure 1.5(a) shows a typical marine ice sheet and the grounding line position. The grounding line may migrate according to the local balance between the weight of ice and displaced ocean water and this balance depends on the ablation and accumulation rate along the marine ice sheet.

The MISI hypothesis states that the grounding line does not stabilize on a bedrock with inland-deepening slope, as represented in Figure 1.5. The most recent ice sheet theory says that the ice flux at the grounding line, Figure 1.5(b), is a positive function of the ice thickness at the grounding line. In marine ice sheets resting on a bedrock that deepens towards the ice-sheet interior, the ice flux increases as the grounding line retreats inland, Figure 1.5(c), which in its turn, induces further the grounding line retraction, Figure 1.5(d). A positive feedback is then triggered, where a self-sustaining grounding line retreat carries on until a stable region is reached (a seaward-sloping bedrock). The MISI hypothesis, emerged in the 1970s [156, 96, 148], has gained attention in recent years with in-situ and satellite observations, analytical studies and numerical simulations [72, 152, 136, 159, 114, 128, 41, 43].

In particular, the Pine Island Glacier, the glacier with the largest discharge in WAIS, has undergone rapid changes in recent decades: satellite data has shown an increase in ice velocities by more than of 40% and a grounding line retraction at a rate of $\sim 1\ km/year$ [104, 128]. The location and profiles of the ice surface and bedrock elevations of Pine Island Glacier are shown in Figure 1.4. The panel in Figure 1.6 summarizes the observed changes in the Cryosphere and sea level equivalent of ice loss from ice sheets (Greenland and Antarctica) and glaciers worldwide (except those present around the ice sheets).

[5] Confined means that the ice shelves are surrounded by a bay, excluding the ice front, which reaches the ocean.

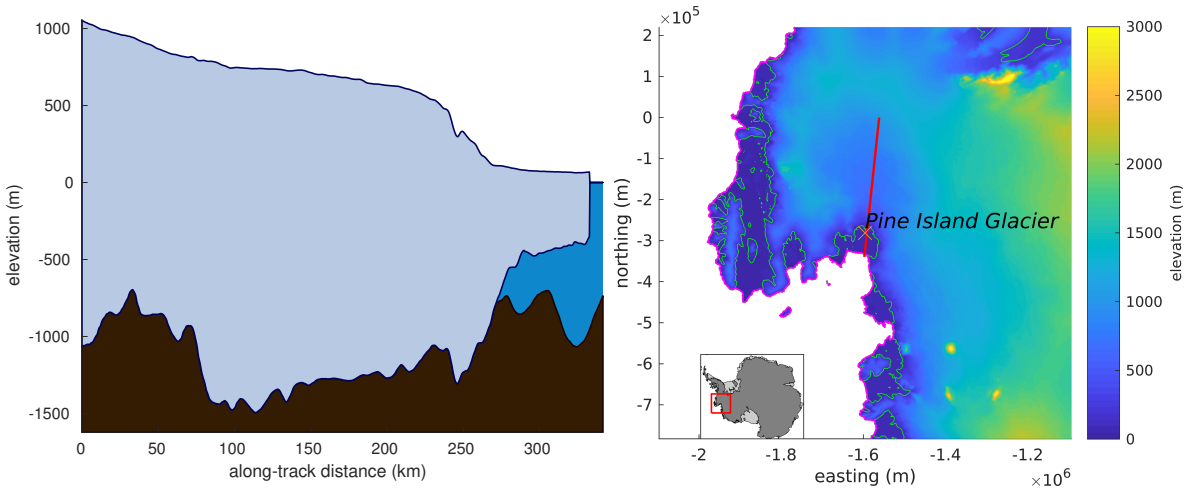

Figure 1.4: Ice surface and bedrock elevations along the flowline of Pine Island Glacier (left). The Pine Island Glacier location (red box) and flowline (red line) are highlighted, and the ice surface elevation is colored (right). Ice fronts are in magenta, grounding lines are in green. Data from the BedMap2 project [45]. Both figures are created with the Antarctic Mapping Tools [48].

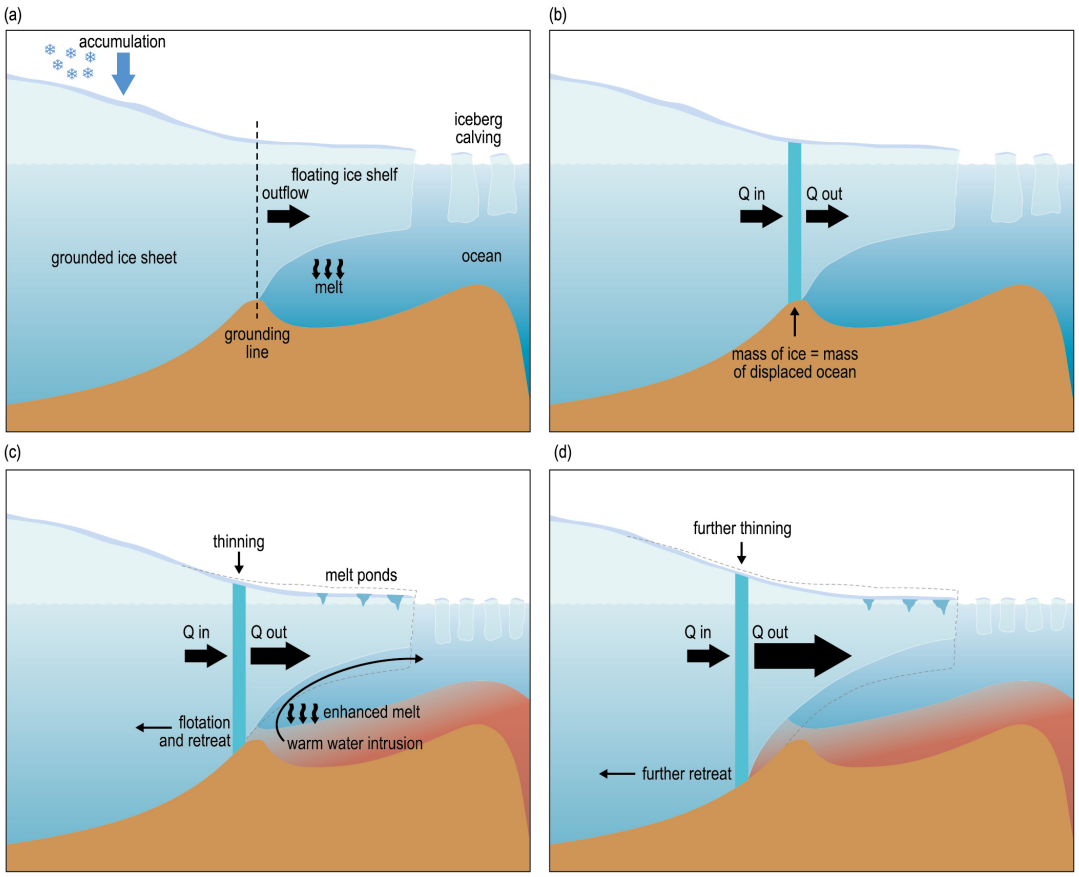

Figure 1.5: The Marine Ice Sheet Instability process. (a) Schematic ice mass balance (accumulation, melting, calving). (b) The ice flux at the grounding line depends on the ice thickness at the grounding line. (c) Perturbation in the melting rate below the ice shelf induces the grounding line retreat. (d) A positive feedback is triggered: the new position inland of the grounding line is associated with a thicker ice, which increases the ice flux, and, consequently, induces further the grounding line migration landward. From [24, p.1175].

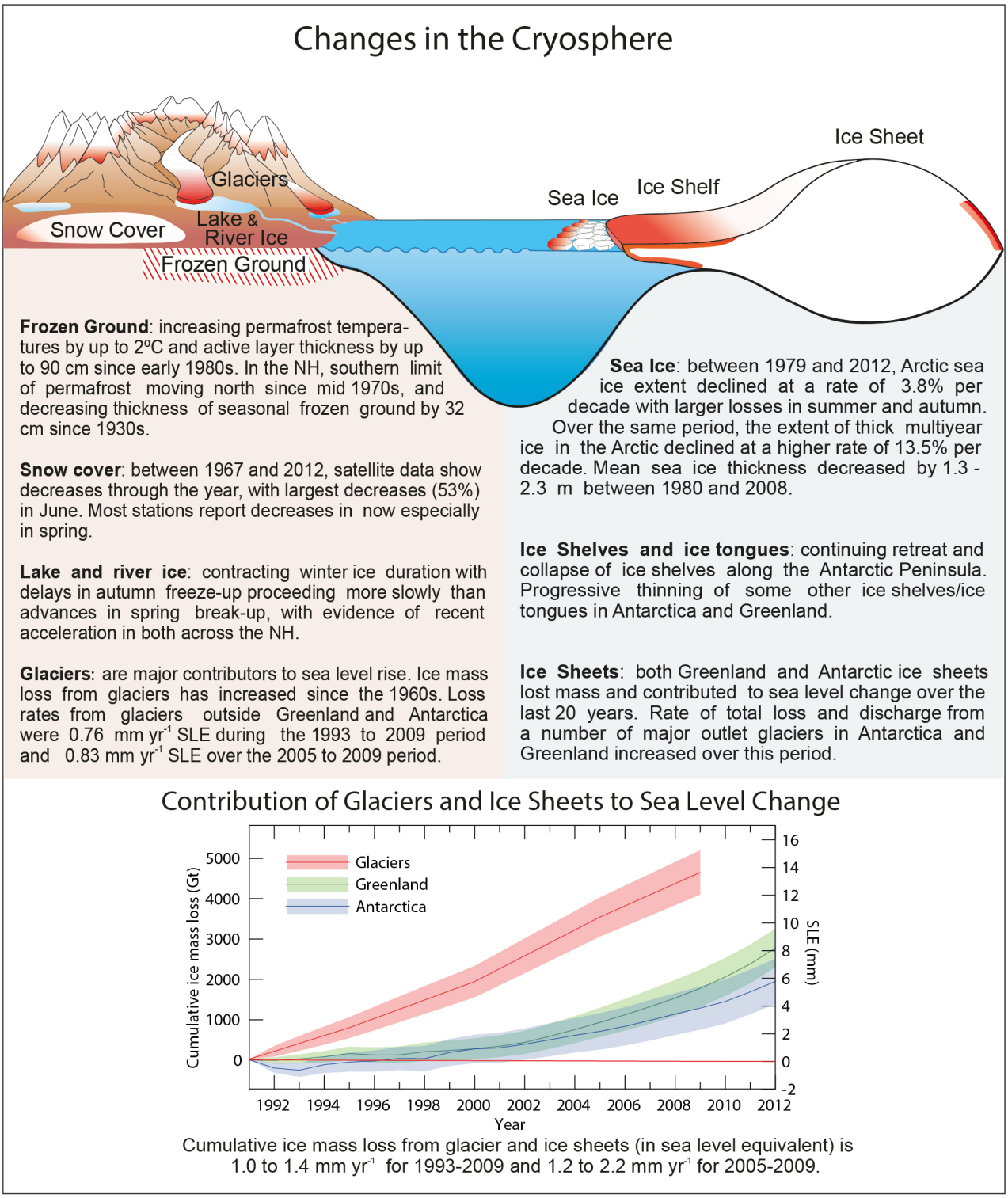

Figure 1.6: Summary of the observed changes in the Cryosphere and estimates of sea level equivalent of ice loss from Greenland and Antarctica, and from all glaciers (except those present around the ice sheets). From [151, p.367].

1.3 Marine ice sheet numerical modeling: challenges

The numerical modeling of ice sheets and glaciers represents a numerical challenge since there are different physical processes involved: distribution of internal forces, non-linear ice rheology, mass balance (accumulation, ablation), heat transfer with atmosphere and bedrock, basal friction, contact with the ocean, grounding line dynamics, etc. In particular, the grounding line represents a discontinuity in the basal friction[6], and the accuracy of its position depends on high mesh or grid resolutions [153, 39, 119].

Meshes or grids with high resolution represent higher computational cost, mainly in uncertainty analyses and sensitivity studies. The generation of meshes or grids with different resolutions may overcome the computational cost: high resolution is employed only in the vicinity of the grounding line. Nevertheless, in transient simulations, the grounding line is free to move and, therefore, the mesh may not be more suitable. The adaptive refinement technique is more appropriate in this case [33, 15]: the mesh is dynamically refined in order to follow the grounding line movement. Basically, there are two types of adaptive mesh refinement: *r*-adaptivity and *h*-adaptivity [112]. The *r*-adaptivity, also known as moving mesh method, moves progressively a fixed number of vertices in a given direction or region [6, p.533], while the *h*-adaptivity method splits edges and/or elements, inserting new vertices into the mesh where high resolution is required [33, 15]. A number of works applying these techniques show promising results: reduction of the error in the grounding line position with reduced computational cost in comparison to uniformly refined meshes [153, 57, 54, 27, 81, 53].

Nowadays there are several ice sheet models dedicated to continental scale simulations (e.g., participants of the ice sheet model intercomparison project [119, 118]) but, unfortunately, the adaptive mesh refinement is not widely applied by these models. For example, the Ice Sheet System Model (ISSM, [88]), developed by the Jet Propulsion Laboratory (JPL/NASA) and University of California at Irvine (UCI), is a parallel finite element-based model dedicated to large-scale simulations. The main goal of the ISSM's team is to model the evolution of Greenland and Antarctic ice sheets. Several techniques are employed in ISSM: parallelism based on the Message Passing Interface (MPI), generation of anisotropic meshes, data assimilation, inverse methods, tools for sensitivity analysis, etc [88, 103]. We highlight that the ISSM mesher only produces static adapted meshes and, therefore, an effort is necessary to tune it to dynamic mesh refinement.

Since each ice sheet model employs a specific numerical method to solve the ice flux equations, some benchmarks have been suggested by the community with the purpose of comparing the models' behavior and understanding the marine ice sheet dynamics, like WAIS (e.g., [119, 118, 7]. These benchmarks reproduce the main aspects of the bedrock topography and climate forcings of real marine ice sheets in idealized model setups. The most recent project is the Marine Ice Sheet-Ocean Model Intercomparison Project (MISOMIP) [7]. The novelty of MISOMIP is the comparison of coupled ice sheet and ocean models. This effort is motivated by recent observations of relative warmer ocean circulation below WAIS ice shelves [78, 40, 86].

[6]The friction at the base of the ice shelf is negligible. See Section 2.6

1.4 Brazilian Antarctic research

In terms of Brazilian Antarctic research, the 'INCT da Criosfera'[7], led by professor Jefferson Cardia Simões, integrates seven (7) national laboratories dedicated to variability analyses of different cryospheric components[8] and their responses to climate changes [144, 145, 126, 35]. Studies include King George Island, where is located the Brazilian station Commander Ferraz[9], Antarctic Peninsula, part of the Antarctic ice sheet [10], as well as the Southern Ocean. A demand of the group is the numerical modeling of glaciers and ice sheets. The last work in this sense was carried out in 2004 [14].

1.5 Goal and contribution of this work

The reduction of numerical errors in marine ice sheet modeling increases the results' accuracy reliability. The goal of this work is to improve the numerical accuracy of marine ice sheet simulations by better capturing grounding line dynamics, while maintaining a low computational cost. To achieve this goal, we implement the adaptive mesh refinement technique and different refinement criteria in the Ice Sheet System Model. We analyze adaptive mesh simulations with uniformly refined meshes using two different benchmarks.

The contributions of this work are summarized below:

- Implementation of an adaptive mesh refinement technique in the Ice Sheet System Model;
- Participation in the Marine Ice Sheet-Ocean Model Intercomparison Project (MISOMIP);
- Performance analysis of the adaptive mesh refinement implementation.

The publications and presentations related to this work are summarized below:

- **dos Santos, T. D.**, Morlighem, M., Seroussi, H., Devloo, P. R. B., and Simões, J. C.: Implementation and performance of adaptive mesh refinement in the Ice Sheet System Model (ISSM v4.14), Geosci. Model Dev., v. 12, p. 215-232, https://doi.org/10.5194/gmd-12-215-2019, 2019.
- **Santos, T. D.**, Devloo, P. R. B., Simões, J. C., Morlighem, M. and Seroussi, H. h-Adaptivity Applied to Ice Sheet Simulation. In: CNMAC 2018 XXXVIII Congresso Nacional de Matemática Aplicada e Computacional, Campinas, SP, Proceeding Series of the Brazilian Society of Computational and Applied Mathematics v. 6 n. 2, https://doi.org/10.5540/03.2018.006.02.0280, 2018.
- **Santos, T. D.**, Devloo, P. R. B., Simões, J. C., Morlighem, M. and Seroussi, H. Adaptive Mesh Refinement Applied to Grounding Line and Ice Front Dynamics. In: European Geosciences Union General Assembly 2018, Viena. Geophysical Research Abstracts, 2018, v. 20., EGU2018-1886.

[7] Instituto Nacional de Ciência e Tecnologia da Criosfera, http://www.ufrgs.br/inctcriosfera/index.html.

[8] Antarctic sea ice, glaciers and Antarctic ice sheet, Andean glaciers, and permafrost.

[9] The operation of the station started in 1984, and in 2012 it was destroyed by a fire. Temporary station modules were installed until the end of the reconstruction, planned for 2018.

[10] Where is installed the Brazilian remote station Criosfera I, https://www.criosfera1.com.

- **Santos, T. D.**, Morlighem, M., Seroussi, H., Larour, E., Simões, J. C., Devloo, P. R. B. h-Adaptivity Applied to Ice Sheet Simulation. In: Numerical Challenges in PDE II, Campinas, 2016

- Seroussi, H., Nakayama, Y., Menemenlis, D., Larour, E., **Santos, T. D.**, Morlighem, M., Cornford, S., Feldmann, J. Marine Ice-sheet and Ocean Model Intercomparison Projects ISSM-MITgcm results. In: Rising Coastal Seas On A Warming Earth II Workshop, New York University Abu Dhabi, United Arab Emirates, 2016.

1.6 Thesis structure

This thesis is organized as follows: in Chapter 2 we outline fundamental physical aspects of marine ice sheet dynamics such as the non-linear behavior of glacial ice, stress balance, grounding line dynamics, etc. In Chapter 3 we summarize the main features of ISSM's architecture and the strategies used to implement an efficient adaptive mesh refinement technique for transient simulations. In Chapter 4 we describe both MIMISP3d and MISMIP+ (a branch of MISOMIP) experiments and the results in terms of grounding line position and processing time. Discussions of our results are also shown in Chapter 4. We finish this thesis with conclusions and future work descriptions in Chapter 5.

Chapter 2

Marine ice sheet dynamics

2.1 Introduction

The dynamics of a glacier is dictated by internal viscous deformation (creep deformation) and basal slip. The driving force is the gravitational force such that the ice flows from a higher point to a lower one, following the gradient of the ice surface. On ice shelves, the floating portions of glaciers or ice sheets, the glacial ice flows continually towards to the open ocean/water, also driven by the gravitational force. The elastic deformation is negligible in time scales greater than days [61, p.60]. The ice flow is modeled by the Stokes equations and the glacial ice is considered incompressible [28, p.12]. The constitutive law relates the strain rate and stress tensors from a non-linear viscosity-type defined by the Glen's law [56]. The evolution of the glacier/ice sheet geometry is computed through a transport-type equation.

The typical spatial scales of glaciers and ice sheets allow some simplifications in the Stokes equations, reducing drastically the computational effort mainly in continental-scale simulations. These simplified models are known as 'approximations' and are widely used in centennial to millennial ice sheet and paleoclimatic reconstruction, sensitivity analysis and future sea level rise projections under climate scenarios [75, 130, 122, 129, 116].

The following sections present the typical scales of ice sheets and the equations commonly used in ice sheet modeling. The equations are derived from conservation laws considering the mechanics of continuous medium. A special emphasis is given to the set of equations used in marine ice sheet simulation, the purpose of this work.

2.2 Typical scale values

Figure 1.1 in Chapter 1 outlines the general components of the Cryosphere, as well as the spatial and temporal scales of each one. Table 2.1 brings together some typical values found in ice sheets and ice shelves. Table 2.2 presents typical values for some dimensionless numbers obtained with the values of Table 2.1. These dimensionless numbers are used in the following sections.

Table 2.1: Typical spatial and temporal scales of ice sheets[61, p.63] and ice shelves [61, p.111].

Parameter	Symbol [unit]	Ice sheets	Ice shelves
ice density	$\rho_0\ [kg/m^3]$	910	910
ice viscosity*	$\mu_0\ [Pas]$	10^{15}	10^{15}
gravitational acceleration	$g_0\ [m/s^2]$	9.81	9.81
angular velocity of the Earth	$\Omega_0\ [rad/s]$	7.2921×10^{-5}	7.2921×10^{-5}
horizontal extent	$L_0\ [km]$	1000	500
vertical extent	$H_0\ [km]$	1	0.5
horizontal velocity	$U_0\ [m/yr]$	100	1000
vertical velocity	$W_0\ [m/yr]$	0.1	1
pressure	$P_0 = \rho_0 g_0 H_0\ [MPa]$	≈ 10	≈ 5
time-scale	$T_0 = L_0/U_0 = H_0/W_0\ [yr]$	10000	500

*At $T = -20°C$ and with $\sigma_e = 50\,kPa$ [61, p.54].

Table 2.2: Dimensionless numbers obtained with the typical scales of ice sheets and ice shelves.

Dimensionless number	Symbol	Ice sheets	Ice shelves
Strouhal	$St = L_0 U_0^{-1} T_0^{-1}$	1	1
Reynolds	$Re = \rho_0 U_0 L_0 \mu_0^{-1}$	$\approx 10^{-12}$	$\approx 10^{-11}$
Froude	$Fr = U_0 g_0^{-1/2} L_0^{-1/2}$	$\approx 10^{-9}$	$\approx 10^{-8}$
Rossby	$Ro = U_0 L_0^{-1} (2\,\Omega_0)^{-1}$	$\approx 10^{-8}$	$\approx 10^{-7}$

Table 2.2 allows us to write the aspect ratio between the vertical and horizontal extents, as well as the respective vertical and horizontal velocities:

$$\epsilon = \frac{H_0}{L_0} = \frac{W_0}{U_0} = 10^{-3}. \tag{2.1}$$

Aspect ratio 2.1 is the 'core number' in glacier/ice sheet dynamics theory. As shown in the following sections, this number also appears in the ratio between internal forces of an ice sheet, which reduces the three-dimensional flow description to simpler formulations.

The aspect ratio ϵ for glaciers differs from that found in ice sheets, assuming a higher value[1]. Therefore, some simplifications applied to ice sheets could generate inaccurate values in numerical simulation of glaciers, where a more complex flow could be present.

[1]Typically some orders higher than the aspect ratio 2.1; even so, as an upper bound, the value $\epsilon \leq \tan 30°$ is virtually fulfilled by all glaciers on the Earth [28, p.296][61, p.152].

2.3 Linear momentum equations

Figure 2.1 presents an idealized marine ice sheet geometry and the coordinate system used throughout this thesis.

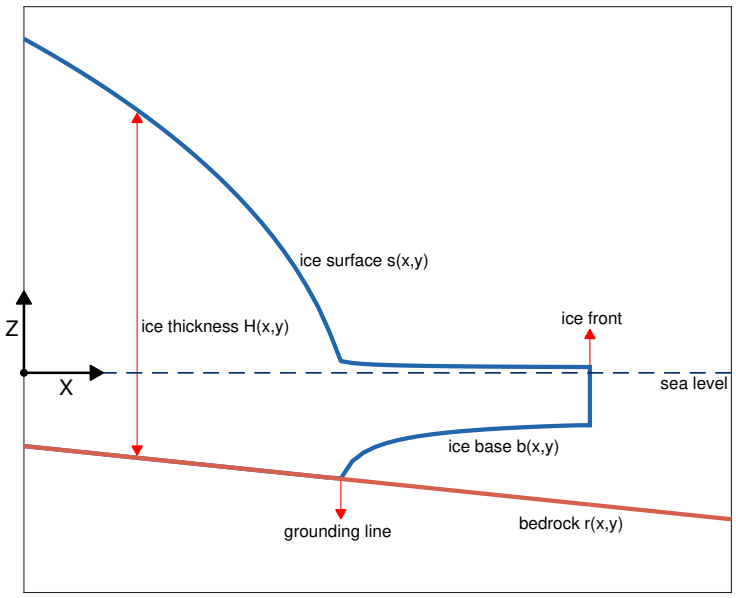

Figure 2.1: Schematic overview of an ice sheet with the coordinate system used in this work.

The glacial ice is considered incompressible [28, p.12]. Then, the equations that represents the conservation of linear momentum are written as:

$$\rho \frac{\partial \mathbf{u}}{\partial t} + \rho \left(\mathbf{u} \cdot \nabla\right) \mathbf{u} - \operatorname{div} \boldsymbol{\sigma} = \mathbf{f}, \tag{2.2}$$

with the incompressibility condition:

$$\operatorname{div} \mathbf{u} = 0, \tag{2.3}$$

where $\mathbf{u}$ $(=\left[u_x\, u_y\, u_z\right]^{\mathsf{T}})$ is the ice velocity, ρ is the ice density and $\mathbf{f}$ are body forces. Body forces acting on a mass of ice on the Earth's surface are the gravitational and Coriolis forces, this last due to the Earth's rotation. Considering these two body forces, Eqs. 2.2 are rewritten as:

$$\rho \frac{\partial \mathbf{u}}{\partial t} + \rho \left(\mathbf{u} \cdot \nabla\right) \mathbf{u} - \operatorname{div} \boldsymbol{\sigma} = \rho \mathbf{g} - 2\rho \boldsymbol{\Omega} \times \mathbf{u}, \tag{2.4}$$

where $\boldsymbol{\Omega}$ is the angular velocity vector.

2.4 Stokes equations

Each variable in the linear momentum equations (Eqs. 2.4) can be rewritten as $x = x^* X_0$, where $x^* = O(1)$ and X_0 has a typical value of the variable x. Then, Eqs. 2.4 are rewritten as:

$$\left(\frac{\rho_0 U_0}{T_0}\right)\rho^*\frac{\partial \mathbf{u}^*}{\partial t^*} + \left(\frac{\rho_0 U_0^2}{L_0}\right)\rho^*\left(\mathbf{u}^*\cdot\nabla\right)\mathbf{u}^* - \left(\frac{\sigma_0}{L_0}\right)\operatorname{div}\boldsymbol{\sigma}^* = \left(\rho_0 g_0\right)\rho^*\mathbf{g}^* - \left(\rho_0\Omega_0 U_0\right)2\rho^*\boldsymbol{\Omega}^*\times\mathbf{u}^*. \tag{2.5}$$

Multiplying both sides of Eqs. 2.5 by $L_0/\left(\rho_0 U_0^2\right)$, we have:

$$\left(\frac{L_0}{U_0 T_0}\right)\rho^*\frac{\partial \mathbf{u}^*}{\partial t^*} + \rho^*\left(\mathbf{u}^*\cdot\nabla\right)\mathbf{u}^* - \left(\frac{\sigma_0}{L_0 U_0^2}\right)\operatorname{div}\boldsymbol{\sigma}^* = \left(\frac{g_0 L_0}{U_0^2}\right)\rho^*\mathbf{g}^* - \left(\frac{L_0 2\Omega_0}{U_0}\right)\rho^*\boldsymbol{\Omega}^*\times\mathbf{u}^*. \tag{2.6}$$

We can crudely define the typical value for the stress as $\sigma_0 = \mu_0 U_0 L_0^{-1}$. Then, using the dimensionless numbers (Table 2.2) and dividing Eqs. 2.6 by ρ^*, we obtain:

$$St\frac{\partial \mathbf{u}^*}{\partial t^*} + \left(\mathbf{u}^*\cdot\nabla\right)\mathbf{u}^* - \frac{1}{Re\,\rho^*}\operatorname{div}\boldsymbol{\sigma}^* = \frac{1}{Fr^2}\mathbf{g}^* - \frac{1}{Ro}\boldsymbol{\Omega}^*\times\mathbf{u}^*, \tag{2.7}$$

such that St, Re, Fr and Ro are the Strouhal, Reynolds, Froude and Rossby numbers, respectively. Using the typical values shown in Table 2.2, we can write the following relation:

$$\frac{1}{Fr^2} > \frac{1}{Re} > \frac{1}{Ro} \gg St. \tag{2.8}$$

Since $St = O(1)$, both the acceleration and inertia terms have small 'contributions' in comparison to the remaining terms in Eqs. 2.7. Moreover, the Coriolis force is at least nine orders of magnitude smaller than the gravitational force. Neglecting these terms yields:

$$\operatorname{div}\boldsymbol{\sigma} + \rho\mathbf{g} = \mathbf{0}. \tag{2.9}$$

Eqs. 2.9 represent a quasi-static flow, known as Stokes or creeping flow, where the only driving force is the gravitational force.

2.5 Constitutive law

The stress tensor $\boldsymbol{\sigma}$ (Cauchy) can be expressed as:

$$\boldsymbol{\sigma} = -p\mathbf{I} + \boldsymbol{\tau}, \tag{2.10}$$

where p is the mechanical pressure, $\mathbf{I}$ is the identity matrix and $\boldsymbol{\tau}$ is the deviatoric stress tensor. Using Eq. 2.10, Eqs. 2.9 are rewritten as:

$$\operatorname{div}\boldsymbol{\tau} - \nabla p + \rho\mathbf{g} = \mathbf{0} \tag{2.11}$$

Since the glacial ice is considered isotropic and incompressible, the resulting constitutive

equations are:

$$\boldsymbol{\tau} = 2\mu\dot{\boldsymbol{\varepsilon}}, \tag{2.12}$$

where $\mu = \mu(T,\ p, \dot{\boldsymbol{\varepsilon}})$ is the dynamic (shear) viscosity of the ice, which depends on the temperature T, pressure p, and strain rate tensor $\dot{\boldsymbol{\varepsilon}}$. The strain rate tensor $\dot{\boldsymbol{\varepsilon}}$ is defined as:

$$\dot{\boldsymbol{\varepsilon}} = \frac{1}{2}\left(\nabla\mathbf{u} + \nabla\mathbf{u}^{\intercal}\right). \tag{2.13}$$

Then, using Eqs. 2.12 and 2.13, the resulting linear momentum equations are:

$$\operatorname{div}\left[\mu\left(\nabla\mathbf{u} + \nabla\mathbf{u}^{\intercal}\right)\right] - \nabla p + \rho\mathbf{g} = \mathbf{0}. \tag{2.14}$$

A constitutive law widely used is the Glen's law, based on the experiments of J. W. Glen in 1955 [56]. Using uniaxial compressive experiments under several values of compressive stress and temperature, Glen obtained the following relation:

$$\dot{\varepsilon}_c = A\sigma_c^n, \tag{2.15}$$

where the subscript c indicates the uniaxial compressive strain rate and stress, A is a parameter that depends on the temperature and n is a constant, known as the flow law exponent, or the Glen's exponent. Glen found $n \approx 3$ [56], and although it is a topic of discussion, several studies have found similar value. Thus, $n = 3$ is the value most frequently used in the literature [73, p.15], [28, p.55].

Relation 2.15 obtained by Glen was generalized by J. F. Nye in 1957 for multiaxial stress states [110]. Assuming the glacial ice as a continuous isotropic medium, Nye postulated the following relation:

$$\dot{\varepsilon}_e = f(\tau_e), \tag{2.16}$$

where $\dot{\varepsilon}_e$ and τ_e was named by Nye as 'effective strain rate' and 'effective shear stress', respectively. Nye defined both of them in terms of the second invariant of the respective tensors:

$$\dot{\varepsilon}_e = \sqrt{II_{\dot{\boldsymbol{\varepsilon}}}} = \sqrt{\frac{1}{2}\operatorname{tr}\left(\dot{\boldsymbol{\varepsilon}}\dot{\boldsymbol{\varepsilon}}^{\intercal}\right)} = \sqrt{\frac{1}{2}\sum_i\sum_j \dot{\varepsilon}_{ij}^2} = \frac{1}{\sqrt{2}} \parallel \dot{\boldsymbol{\varepsilon}} \parallel_F, \tag{2.17}$$

$$\tau_e = \sqrt{II_{\boldsymbol{\tau}}} = \sqrt{\frac{1}{2}\operatorname{tr}\left(\boldsymbol{\tau}\boldsymbol{\tau}^{\intercal}\right)} = \sqrt{\frac{1}{2}\sum_i\sum_j \tau_{ij}^2} = \frac{1}{\sqrt{2}} \parallel \boldsymbol{\tau} \parallel_F, \tag{2.18}$$

where $\parallel \cdot \parallel_F$ is the Frobenius norm [59, p.55]. It is important to note that using the second invariant of the tensors returns $\tau_e = |\tau_{xz}|$ and $\dot{\varepsilon}_e = |\dot{\varepsilon}_{xz}|$ for the simple shear condition (which is consistent with the ice viscosity expression as we show below).

Using a general form for relation 2.12, i.e.:

$$\dot{\boldsymbol{\varepsilon}} = \lambda\boldsymbol{\tau}, \tag{2.19}$$

Nye obtained the same relation for the effective strain rate and effective shear stress (in fact this

is easily verifiable since $\mathrm{tr}\,(\dot{\boldsymbol{\varepsilon}}\dot{\boldsymbol{\varepsilon}}^{\intercal}) = \lambda^2 \mathrm{tr}\,(\boldsymbol{\tau}\boldsymbol{\tau}^{\intercal})$):

$$\dot{\varepsilon}_e = \lambda \tau_e. \tag{2.20}$$

Then, Nye extended the Glen's relation 2.15 as:

$$f(\tau_e) = \left(\frac{\tau_e}{B}\right)^n, \tag{2.21}$$

which from Eq. 2.16 yields:

$$\dot{\varepsilon}_e = \left(\frac{\tau_e}{B}\right)^n. \tag{2.22}$$

Using relation 2.20 and Nye's extension 2.22 yields:

$$\lambda = \frac{\tau_e^{n-1}}{B^n}, \tag{2.23}$$

which is the original relation written by Nye [110]. For numerical purposes, we define λ as a function of the effective strain rate. Then, from relation 2.22, we have:

$$\tau_e = B\dot{\varepsilon}_e^{1/n}, \tag{2.24}$$

which through relation 2.20 yields:

$$\lambda = \frac{\dot{\varepsilon}_e^{1-1/n}}{B}. \tag{2.25}$$

We can finally write an expression for the ice viscosity μ. Using the general form of the constitutive law, Eq. 2.20, relation 2.25 for λ, and constitutive law 2.12, we have:

$$\mu = \frac{1}{2\lambda}, \tag{2.26}$$

which yields:

$$\mu = \frac{B^n}{2\tau_e^{n-1}} = \frac{B}{2\dot{\varepsilon}_e^{1-1/n}} = \frac{1}{2A^{1/n}\dot{\varepsilon}_e^{1-1/n}}, \tag{2.27}$$

with $B = A^{-1/n}$ (or $A = B^{-n}$). The flow parameter A (the same from the original Glen's relation 2.15) is known as the 'rate factor', and B as the 'associated rate factor'. Glen used an Arrhenius law-type to express A as:

$$A = A_0 \exp\left(-\frac{Q}{RT'}\right), \tag{2.28}$$

where A_0 is a pre-exponential constant, Q is the activation energy, R is the universal gas constant, and T' is the temperature relative to the pressure melting point. Glen used T' as the absolute temperature in his original paper [56]; here, we consider a linear temperature-pressure dependency as shown in [61, p.54]:

$$T' = T + \beta\, p, \tag{2.29}$$

where T is the absolute temperature, p is the mechanical pressure, and β is the Clausius-

Clapeyron constant. Some recommended values for the Arrhenius law (Eq. 2.28) are listed in Table 2.3.

Recommended values for the flow parameter (A) as a function of the temperature (Cuffey and Paterson, 2010 [28]) are listed in Table 2.4. Values obtained with Arrhenius law 2.28 and Table 2.3 are also listed in Table 2.4. Figure 2.2 shows the ice viscosity as a function of the effective stress (τ_e). The viscosity values are calculated using Eq. 2.27 with the effective strain rate ($\dot{\varepsilon}_e$) given by Eq. 2.22. The strain rate behavior for different values of the Glen's exponent is illustrated in Figure 2.3. The curves are obtained using $\dot{\varepsilon} = A\tau^n$. For the linear case ($n = 1$), we apply an ice viscosity $\sim 10^{14}\ Pa\ s$ [28, p.62].

Table 2.3: Typical parameter values for the Arrhenius law, Eq. 2.28 [61].

Parameter	Value	Obs.
R (universal gas constant)	$8.314\ Jmol^{-1}K^{-1}$	
β (Clausius-Clapeyron constant)	$7.42 \times 10^{-8}\ K\ Pa^{-1}$	pure ice
	$9.8 \times 10^{-8}\ K\ Pa^{-1}$	air-saturated ice
Q (activation energy)	$60\ kJmol^{-1}$	for $T' \leq 263.15K$
	$139\ kJmol^{-1}$	for $T' > 263.15K$
A_0 (pre-exponential constant)*	$3.985 \times 10^{-13}\ Pa^{-3}s^{-1}$	for $T' \leq 263.15K$
	$1.916 \times 10^{3}\ Pa^{-3}s^{-1}$	for $T' > 263.15K$

*These values hold for $n = 3$ [61, p.54].

Table 2.4: Recommended values for the flow parameter A from Cuffey and Paterson (2010) [28, p.75], and values calculated using Arrhenius law 2.28 with values of Table 2.3.

Temperature* [$^\circ C$]	A** [$Pa^{-3}s^{-1}$]	
	Cuffey & Paterson [28, p.75]	Arrhenius law 2.28
0	2.4×10^{-24}	5.0×10^{-24}
-2	1.7×10^{-24}	3.2×10^{-24}
-5	9.3×10^{-25}	1.6×10^{-24}
-10	3.5×10^{-25}	4.9×10^{-25}
-15	2.1×10^{-25}	2.9×10^{-25}
-20	1.2×10^{-25}	1.7×10^{-25}
-25	6.8×10^{-26}	9.3×10^{-26}
-30	3.7×10^{-26}	5.1×10^{-26}
-30	2.0×10^{-26}	2.7×10^{-26}
-40	1.0×10^{-26}	1.4×10^{-26}
-45	5.2×10^{-27}	7.3×10^{-27}
-50	2.6×10^{-27}	3.6×10^{-27}

*Relative to the pressure melting point.

**These values hold for $n = 3$.

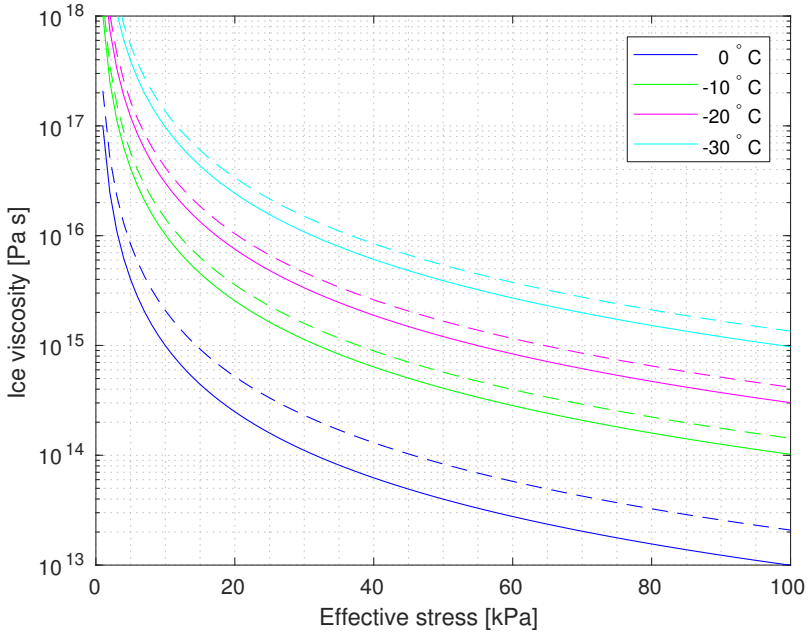

Figure 2.2: Ice viscosity as a function of the effective stress (τ_e) and temperature. The values correspond to Arrhenius law 2.28 (solid lines) and values from Cuffey and Paterson (2010) (dashed lines). See Table 2.4.

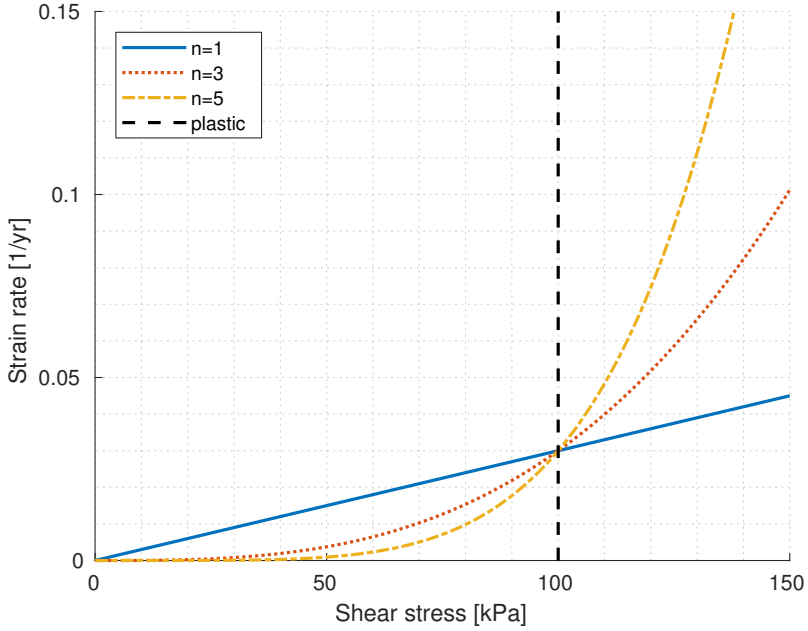

Figure 2.3: Strain rate as a function of the shear stress ($\dot{\varepsilon} = A\tau^n$) for different values of exponent n. For the linear case, the ice viscosity used is $\sim 10^{14}\, Pa\, s$ [28, p.62]. The plastic curve refers to the case when $n \to \infty$; in this case, the plastic yield stress used is $100\, kPa$.

2.6 Shelf-Stream Approximation

The aspect ratio of marine ice sheets allows some simplifications in the Stokes equations (Eqs. 2.9). In fact, the behavior of any fluid on the Earth's surface is to spread under the gravitational force, increasing its surface area and reducing, consequently, its thickness, in a diffusion-type movement. This is the basic behavior of glaciers and ice sheets (see Section 2.2 and Eq. 2.1). In marine ice sheets, both grounded and floating part are under the same driving force, the gravitational force, but under different equilibrium forces. While the grounded part slips on the bedrock, which imposes a basal force contrary to the ice flow, the attached ice shelf is under a negligible base-sea friction, but in a membrane-type stress balance.

In this section we derive the 'Shelf-Stream' or 'Shallow-Shelf' Approximation (SSA) to describe the marine ice sheet stress balance. L. W. Morland, in 1987 [100], derived the SSA equations for unconfined ice shelves. D. R. MacAyeal, in 1989 [94], derived the same formulation for both ice stream, the grounded part with basal friction, and ice shelf. There are different approaches to derive these equations in the literature (e.g., [105, 135, 61, 101]). Here, we follow [61, p.117] and [101, p.47].

The following assumptions are employed in the SSA formulation:

$$\begin{aligned} \frac{\partial \sigma_{xz}}{\partial x} &\ll \frac{\partial \sigma_{zz}}{\partial z}, \\ \frac{\partial \sigma_{yz}}{\partial y} &\ll \frac{\partial \sigma_{zz}}{\partial z}, \end{aligned} \tag{2.30}$$

$$\begin{aligned} \frac{\partial u_x}{\partial z} &\approx 0, \\ \frac{\partial u_y}{\partial z} &\approx 0, \end{aligned} \tag{2.31}$$

$$\begin{aligned} \dot{\varepsilon}_{xz} &\approx 0, \\ \dot{\varepsilon}_{yz} &\approx 0, \end{aligned} \tag{2.32}$$

$$\begin{aligned} \frac{\partial b}{\partial x} &\approx 0, \\ \frac{\partial b}{\partial y} &\approx 0. \end{aligned} \tag{2.33}$$

where b is the ice base (see Figure 2.1). To apply these assumptions, it is useful to rewrite the Stokes equations (Eqs. 2.9) for each Cartesian component. Considering the balance of angular

momentum, we have $\boldsymbol{\sigma} = \boldsymbol{\sigma}^{\intercal}$, and then:

$$\begin{aligned}
\frac{\partial \sigma_{xx}}{\partial x} + \frac{\partial \sigma_{xy}}{\partial y} + \frac{\partial \sigma_{xz}}{\partial z} &= 0, \\
\frac{\partial \sigma_{xy}}{\partial x} + \frac{\partial \sigma_{yy}}{\partial y} + \frac{\partial \sigma_{yz}}{\partial z} &= 0, \\
\frac{\partial \sigma_{xz}}{\partial x} + \frac{\partial \sigma_{yz}}{\partial z} + \frac{\partial \sigma_{zz}}{\partial z} &= \rho g,
\end{aligned} \tag{2.34}$$

or, from Eqs. 2.14:

$$\begin{aligned}
&\frac{\partial}{\partial x}\left(2\mu\frac{\partial u_x}{\partial x}\right) + \frac{\partial}{\partial y}\left(\mu\frac{\partial u_x}{\partial y} + \mu\frac{\partial u_y}{\partial x}\right) + \frac{\partial}{\partial z}\left(\mu\frac{\partial u_x}{\partial z} + \mu\frac{\partial u_z}{\partial x}\right) - \frac{\partial p}{\partial x} = 0, \\
&\frac{\partial}{\partial x}\left(\mu\frac{\partial u_x}{\partial y} + \mu\frac{\partial u_y}{\partial x}\right) + \frac{\partial}{\partial y}\left(2\mu\frac{\partial u_y}{\partial y}\right) + \frac{\partial}{\partial z}\left(\mu\frac{\partial u_y}{\partial z} + \mu\frac{\partial u_z}{\partial y}\right) - \frac{\partial p}{\partial y} = 0, \\
&\frac{\partial}{\partial x}\left(\mu\frac{\partial u_x}{\partial z} + \mu\frac{\partial u_z}{\partial x}\right) + \frac{\partial}{\partial y}\left(\mu\frac{\partial u_y}{\partial z} + \mu\frac{\partial u_z}{\partial y}\right) + \frac{\partial}{\partial z}\left(2\mu\frac{\partial u_z}{\partial z}\right) - \frac{\partial p}{\partial z} = \rho g,
\end{aligned} \tag{2.35}$$

with the incompressibility equation (Eq. 2.3):

$$\frac{\partial u_x}{\partial x} + \frac{\partial u_y}{\partial y} + \frac{\partial u_z}{\partial z} = 0. \tag{2.36}$$

The first assumption (2.30) leads to a hydrostatic approximation of the vertical normal stress, σ_{zz}. In fact, the shear stresses σ_{xz} and σ_{yz} are, in general, $\leq 100\, kPa$ for the entire ice sheet [61, p.73], which are small in comparison to the pressure p magnitude ($P_0 \approx 10\, Mpa$, see Table 2.1). Therefore, assuming $\sigma_{zz} \mid_H \approx \rho g H$ is a reasonable approximation. Then, neglecting the shear stresses in Eq. 2.34(c) yields:

$$\frac{\partial \sigma_{zz}}{\partial z} = \frac{\partial}{\partial z}\left(2\mu\frac{\partial u_z}{\partial z} - p\right) = \rho g. \tag{2.37}$$

Integrating Eq. 2.37 for $z \in [z,\, s]$, we have:

$$\sigma_{zz} \mid_s - \sigma_{zz} \mid_z = \left(2\mu\frac{\partial u_z}{\partial z} - p\right)_s - \left(2\mu\frac{\partial u_z}{\partial z} - p\right)_z = \rho g\,(s - z)\,. \tag{2.38}$$

At the ice surface, the normal stress is assumed to be neglected, i.e., $\sigma_{zz} \mid_s = 0$. Then, we can write an expression for pressure p at any z:

$$p = 2\mu\frac{\partial u_z}{\partial z} + \rho g\,(s - z)\,. \tag{2.39}$$

Now, we can use the continuity equation (Eq. 2.36) to rewrite the pressure equation 2.39 as:

$$p = -2\mu\left(\frac{\partial u_x}{\partial x} + \frac{\partial u_y}{\partial y}\right) + \rho g\,(s - z), \tag{2.40}$$

which can be inserted in Eqs. 2.35(a, b):

$$\begin{aligned}
&\frac{\partial}{\partial x}\left(4\mu\frac{\partial u_x}{\partial x} + 2\mu\frac{\partial u_y}{\partial y}\right) + \frac{\partial}{\partial y}\left(\mu\frac{\partial u_x}{\partial y} + \mu\frac{\partial u_y}{\partial x}\right) + \frac{\partial}{\partial z}\left(\mu\frac{\partial u_x}{\partial z} + \mu\frac{\partial u_z}{\partial x}\right) = \rho g\frac{\partial s}{\partial x},\\
&\frac{\partial}{\partial x}\left(\mu\frac{\partial u_x}{\partial y} + \mu\frac{\partial u_y}{\partial x}\right) + \frac{\partial}{\partial y}\left(4\mu\frac{\partial u_y}{\partial y} + 2\mu\frac{\partial u_x}{\partial x}\right) + \frac{\partial}{\partial z}\left(\mu\frac{\partial u_y}{\partial z} + \mu\frac{\partial u_z}{\partial y}\right) = \rho g\frac{\partial s}{\partial y}.
\end{aligned} \tag{2.41}$$

Equations 2.41 are known as the 'hydrostatic approximation' [61, p.72]. Assumption 2.30 decouples the pressure from the velocity field equations (Stokes equations), which makes the numerical solution simpler. From Table 2.1 and Eq. 2.1, we can write:

$$\frac{\partial u_z}{\partial x}\Big/\frac{\partial u_x}{\partial z},\ \frac{\partial u_z}{\partial y}\Big/\frac{\partial u_y}{\partial z} \sim \frac{[W_0]}{[L_0]}\Big/\frac{[U_0]}{[H_0]} = \frac{[W_0]\,[H_0]}{[U_0]\,[L_0]} = \epsilon^2 \sim 10^{-6}. \tag{2.42}$$

Then, neglecting $\partial u_z/\partial x$ and $\partial u_z/\partial y$ in Eqs. 2.41, we have:

$$\begin{aligned}
&\frac{\partial}{\partial x}\left(4\mu\frac{\partial u_x}{\partial x} + 2\mu\frac{\partial u_y}{\partial y}\right) + \frac{\partial}{\partial y}\left(\mu\frac{\partial u_x}{\partial y} + \mu\frac{\partial u_y}{\partial x}\right) + \frac{\partial}{\partial z}\left(\mu\frac{\partial u_x}{\partial z}\right) = \rho g\frac{\partial s}{\partial x},\\
&\frac{\partial}{\partial x}\left(\mu\frac{\partial u_x}{\partial y} + \mu\frac{\partial u_y}{\partial x}\right) + \frac{\partial}{\partial y}\left(4\mu\frac{\partial u_y}{\partial y} + 2\mu\frac{\partial u_x}{\partial x}\right) + \frac{\partial}{\partial z}\left(\mu\frac{\partial u_y}{\partial z}\right) = \rho g\frac{\partial s}{\partial y}.
\end{aligned} \tag{2.43}$$

In the literature, Eqs. 2.43 are called as the Blatter & Pattyn (BP) or Higher-Order (HO) Approximation (or yet First-Order, FO, Approximation [61, p.75]). H. Blatter developed this formulation in 1995 [18] based on a bidimensional version of H. C. Muller (1991). In a different approach, F. Pattyn, in 2003, developed the same formulation, but solving them in terms of the velocity field gradient [115], unlike Blatter that solved the equations in terms of the stress field.

Assumptions 2.31 and 2.32 indicate that the vertical changes of the horizontal velocities are negligible, i.e., the ice motion is mainly dictated by basal sliding, being insignificant the shear deformation in the ice body. Then, under assumptions 2.31 and 2.32, Eqs. 2.43 are written as:

$$\begin{aligned}
&\frac{\partial}{\partial x}\left(4\mu\frac{\partial u_x}{\partial x} + 2\mu\frac{\partial u_y}{\partial y}\right) + \frac{\partial}{\partial y}\left(\mu\frac{\partial u_x}{\partial y} + \mu\frac{\partial u_y}{\partial x}\right) = \rho g\frac{\partial s}{\partial x},\\
&\frac{\partial}{\partial x}\left(\mu\frac{\partial u_x}{\partial y} + \mu\frac{\partial u_y}{\partial x}\right) + \frac{\partial}{\partial y}\left(4\mu\frac{\partial u_y}{\partial y} + 2\mu\frac{\partial u_x}{\partial x}\right) = \rho g\frac{\partial s}{\partial y}.
\end{aligned} \tag{2.44}$$

Since it is assumed that u_x and u_y are z-independent, we can integrate Eqs. 2.44 in the

vertical coordinate $z \in [b,\ s]$:

$$\begin{aligned}
&\frac{\partial}{\partial x}\int_b^s \left(4\mu\frac{\partial u_x}{\partial x} + 2\mu\frac{\partial u_y}{\partial y}\right) dz + \frac{\partial}{\partial y}\int_b^s \left(\mu\frac{\partial u_x}{\partial y} + \mu\frac{\partial u_y}{\partial x}\right) dz \\
&+ \left(4\mu\frac{\partial u_x}{\partial x} + 2\mu\frac{\partial u_y}{\partial y}\right)_b \frac{\partial b}{\partial x} - \left(4\mu\frac{\partial u_x}{\partial x} + 2\mu\frac{\partial u_y}{\partial y}\right)_s \frac{\partial s}{\partial x} \\
&+ \left(\mu\frac{\partial u_x}{\partial y} + \mu\frac{\partial u_y}{\partial x}\right)_b \frac{\partial b}{\partial y} - \left(\mu\frac{\partial u_x}{\partial y} + \mu\frac{\partial u_y}{\partial x}\right)_s \frac{\partial s}{\partial y} = \rho g H \frac{\partial s}{\partial x}, \\
&\frac{\partial}{\partial x}\int_b^s \left(\mu\frac{\partial u_x}{\partial y} + \mu\frac{\partial u_y}{\partial x}\right) dz + \frac{\partial}{\partial y}\int_b^s \left(4\mu\frac{\partial u_y}{\partial y} + 2\mu\frac{\partial v_x}{\partial x}\right) dz \\
&+ \left(\mu\frac{\partial u_x}{\partial y} + \mu\frac{\partial u_y}{\partial x}\right)_b \frac{\partial b}{\partial x} - \left(\mu\frac{\partial u_x}{\partial y} + \mu\frac{\partial u_y}{\partial x}\right)_s \frac{\partial s}{\partial x} \\
&+ \left(4\mu\frac{\partial u_y}{\partial y} + 2\mu\frac{\partial u_x}{\partial x}\right)_b \frac{\partial b}{\partial y} - \left(4\mu\frac{\partial u_y}{\partial y} + 2\mu\frac{\partial u_x}{\partial x}\right)_s \frac{\partial s}{\partial y} = \rho g H \frac{\partial s}{\partial y}.
\end{aligned} \tag{2.45}$$

Note that $H = \int_b^s dz$. The Leibniz's rule is used in the integration since $s = s(x, y)$ and $b = b(x, y)$. Using the horizontal components of the stress field, Eqs. 2.45 are written as:

$$\begin{aligned}
&\frac{\partial}{\partial x}\int_b^s \left(4\mu\frac{\partial u_x}{\partial x} + 2\mu\frac{\partial u_y}{\partial y}\right) dz + \frac{\partial}{\partial y}\int_b^s \left(\mu\frac{\partial u_x}{\partial y} + \mu\frac{\partial u_y}{\partial x}\right) dz \\
&+ \left(2\tau_{xx} + \tau_{yy}\right)_b \frac{\partial b}{\partial x} - \left(2\tau_{xx} + \tau_{yy}\right)_s \frac{\partial s}{\partial x} \\
&+ \tau_{xy}\,|_b \frac{\partial b}{\partial y} - \tau_{xy}\,|_s \frac{\partial s}{\partial y} = \rho g H \frac{\partial s}{\partial x}, \\
&\frac{\partial}{\partial x}\int_b^s \left(\mu\frac{\partial u_x}{\partial y} + \mu\frac{\partial u_y}{\partial x}\right) dz + \frac{\partial}{\partial y}\int_b^s \left(4\mu\frac{\partial u_y}{\partial y} + 2\mu\frac{\partial u_x}{\partial x}\right) dz \\
&+ \tau_{xy}\,|_b \frac{\partial b}{\partial x} - \tau_{xy}\,|_s \frac{\partial s}{\partial x} \\
&+ \left(\tau_{xx} + 2\tau_{yy}\right)_b \frac{\partial b}{\partial y} - \left(\tau_{xx} + 2\tau_{yy}\right)_s \frac{\partial s}{\partial y} = \rho g H \frac{\partial s}{\partial y}.
\end{aligned} \tag{2.46}$$

It is assumed that the stress at the ice surface is negligible, i.e., $\boldsymbol{\sigma} \mid_s \mathbf{n}_s \approx \mathbf{0}$. Then, with:

$$\mathbf{n}_s = \frac{1}{N_s}\begin{bmatrix} -\dfrac{\partial s}{\partial x} \\ -\dfrac{\partial s}{\partial y} \\ 1 \end{bmatrix},\ N_s = \left[1 + \left(\frac{\partial s}{\partial x}\right)^2 + \left(\frac{\partial s}{\partial y}\right)^2\right]^{1/2}, \tag{2.47}$$

we have:

$$\boldsymbol{\sigma} \mid_s \mathbf{n}_s = \frac{1}{N_s}\begin{bmatrix} -\tau_{xx}\dfrac{\partial s}{\partial x} - \tau_{xy}\dfrac{\partial s}{\partial y} + \tau_{xz} + p\dfrac{\partial s}{\partial x} \\ -\tau_{xy}\dfrac{\partial s}{\partial x} - \tau_{yy}\dfrac{\partial s}{\partial y} + \tau_{yz} + p\dfrac{\partial s}{\partial y} \\ -\tau_{xz}\dfrac{\partial s}{\partial x} - \tau_{yz}\dfrac{\partial s}{\partial y} + \tau_{zz} - p \end{bmatrix}_s \approx \begin{bmatrix} 0 \\ 0 \\ 0 \end{bmatrix}. \tag{2.48}$$

The pressure equation (Eq. 2.40) in terms of the normal deviatoric stresses is written as:

$$p = -\tau_{xx} - \tau_{yy} + \rho g\,(s - z), \tag{2.49}$$

then, from Eq. 2.48, assuming τ_{xz} and τ_{yz} as negligible (assumption 2.32) and considering the incompressibility condition ($\tau_{xx} + \tau_{yy} + \tau_{zz} = 0$), we have:

$$\begin{aligned} -\left(2\tau_{xx} + \tau_{yy}\right)_s \frac{\partial s}{\partial x} - \tau_{xy} \mid_s \frac{\partial s}{\partial y} &\approx 0, \\ -\tau_{xy} \mid_s \frac{\partial s}{\partial x} - \left(\tau_{xx} + 2\tau_{yy}\right)_s \frac{\partial s}{\partial y} &\approx 0. \end{aligned} \tag{2.50}$$

Then, neglecting the terms of Eq. 2.50 in Eqs. 2.46, we have:

$$\begin{aligned} &\frac{\partial}{\partial x}\int_b^s \left(4\mu\frac{\partial u_x}{\partial x} + 2\mu\frac{\partial u_y}{\partial y}\right) dz + \frac{\partial}{\partial y}\int_b^s \left(\mu\frac{\partial u_x}{\partial y} + \mu\frac{\partial u_y}{\partial x}\right) dz \\ &\qquad + \left(2\tau_{xx} + \tau_{yy}\right)_b \frac{\partial b}{\partial x} + \tau_{xy} \mid_b \frac{\partial b}{\partial y} = \rho g H \frac{\partial s}{\partial x}, \\ &\frac{\partial}{\partial x}\int_b^s \left(\mu\frac{\partial u_x}{\partial y} + \mu\frac{\partial u_y}{\partial x}\right) dz + \frac{\partial}{\partial y}\int_b^s \left(4\mu\frac{\partial u_y}{\partial y} + 2\mu\frac{\partial u_x}{\partial x}\right) dz \\ &\qquad + \tau_{xy} \mid_b \frac{\partial b}{\partial x} + \left(\tau_{xx} + 2\tau_{yy}\right)_b \frac{\partial b}{\partial y} = \rho g H \frac{\partial s}{\partial y}. \end{aligned} \tag{2.51}$$

Now, we come back to the boundary condition at the ice base. We consider a general basal friction $\boldsymbol{\tau}_b$ (defined as a vector pointed in the opposite direction to the ice flow) such that:

$$\boldsymbol{\tau}_b = \boldsymbol{\sigma} \mid_b \mathbf{n}_b - \left[(\boldsymbol{\sigma} \mid_b \mathbf{n}_b) \cdot \mathbf{n}_b\right] \mathbf{n}_b, \tag{2.52}$$

where:

$$\mathbf{n}_b = \frac{1}{N_b}\begin{bmatrix}\dfrac{\partial b}{\partial x}\\ \dfrac{\partial b}{\partial y}\\ -1\end{bmatrix},\ N_b = \left[1 + \left(\frac{\partial b}{\partial x}\right)^2 + \left(\frac{\partial b}{\partial y}\right)^2\right]^{1/2}, \tag{2.53}$$

$$\boldsymbol{\sigma}\ |_b\ \mathbf{n}_b = \frac{1}{N_b}\begin{bmatrix}\tau_{xx}\dfrac{\partial b}{\partial x} + \tau_{xy}\dfrac{\partial b}{\partial y} - \tau_{xz} - p\dfrac{\partial b}{\partial x}\\ \tau_{xy}\dfrac{\partial b}{\partial x} + \tau_{yy}\dfrac{\partial b}{\partial y} - \tau_{yz} - p\dfrac{\partial b}{\partial y}\\ \tau_{xz}\dfrac{\partial b}{\partial x} + \tau_{yz}\dfrac{\partial b}{\partial y} - \tau_{zz} + p\end{bmatrix}_b, \tag{2.54}$$

$$\begin{aligned}(\boldsymbol{\sigma}\ |_b\ \mathbf{n}_b)\cdot\mathbf{n}_b = \frac{1}{N_b^2}\left(\tau_{xx}\frac{\partial b}{\partial x} + \tau_{xy}\frac{\partial b}{\partial y} - \tau_{xz} - p\frac{\partial b}{\partial x}\right)_b\frac{\partial b}{\partial x}\\ +\frac{1}{N_b^2}\left(\tau_{xy}\frac{\partial b}{\partial x} + \tau_{yy}\frac{\partial b}{\partial y} - \tau_{yz} - p\frac{\partial b}{\partial y}\right)_b\frac{\partial b}{\partial y} - \frac{1}{N_b^2}\left(\tau_{xz}\frac{\partial b}{\partial x} + \tau_{yz}\frac{\partial b}{\partial y} - \tau_{zz} + p\right)_b.\end{aligned} \tag{2.55}$$

Then, neglecting the quadratic terms in $\partial b/\partial x$ and $\partial b/\partial y$ (assumption 2.33, note that $N_b \approx 1$), and using the pressure expression 2.49, we have:

$$\boldsymbol{\sigma}\ |_b\ \mathbf{n}_b = \begin{bmatrix}\tau_{xx}\ |_b\ \dfrac{\partial b}{\partial x} + \tau_{xy}\ |_b\ \dfrac{\partial b}{\partial y} - \left(-\tau_{xx}\ |_b - \tau_{yy}\ |_b + \rho g H\right)\dfrac{\partial b}{\partial x}\\ \tau_{xy}\ |_b\ \dfrac{\partial b}{\partial x} + \tau_{yy}\ |_b\ \dfrac{\partial b}{\partial y} - \left(-\tau_{xx}\ |_b - \tau_{yy}\ |_b + \rho g H\right)\dfrac{\partial b}{\partial y}\\ -\tau_{zz}\ |_b + \left(-\tau_{xx}\ |_b - \tau_{yy}\ |_b + \rho g H\right)\end{bmatrix}, \tag{2.56}$$

$$(\boldsymbol{\sigma}\ |_b\ \mathbf{n}_b)\cdot\mathbf{n}_b \approx \tau_{zz}\ |_b - p\ |_b = -\rho g H. \tag{2.57}$$

Note that the terms τ_{xz} and τ_{yz} are neglected (assumption 2.32). Then, from Eqs. 2.56 and 2.57, we can define the basal friction (Eq. 2.52) as:

$$\boldsymbol{\tau}_b = \begin{bmatrix}\left(2\tau_{xx}\ |_b + \tau_{yy}\ |_b\right)\dfrac{\partial b}{\partial x} + \tau_{xy}\ |_b\ \dfrac{\partial b}{\partial y} - \rho g H\dfrac{\partial b}{\partial x}\\ \tau_{xy}\ |_b\ \dfrac{\partial b}{\partial x} + \left(\tau_{xx}\ |_b + 2\tau_{yy}\ |_b\right)\dfrac{\partial b}{\partial y} - \rho g H\dfrac{\partial b}{\partial y}\\ \rho g H\end{bmatrix} + \rho g H\begin{bmatrix}\dfrac{\partial b}{\partial x}\\ \dfrac{\partial b}{\partial y}\\ -1\end{bmatrix}, \tag{2.58}$$

or

$$\boldsymbol{\tau}_b = \begin{bmatrix}\tau_{bx}\\ \tau_{by}\\ \tau_{bz}\end{bmatrix} = \begin{bmatrix}\left(2\tau_{xx}\ |_b + \tau_{yy}\ |_b\right)\dfrac{\partial b}{\partial x} + \tau_{xy}\ |_b\ \dfrac{\partial b}{\partial y}\\ \tau_{xy}\ |_b\ \dfrac{\partial b}{\partial x} + \left(\tau_{xx}\ |_b + 2\tau_{yy}\ |_b\right)\dfrac{\partial b}{\partial y}\\ 0\end{bmatrix}. \tag{2.59}$$

Therefore, in the SSA formulation, the basal friction has only horizontal components. Then,

Eqs. 2.51 are written as:

$$\begin{aligned}
&\frac{\partial}{\partial x}\int_b^s \left(4\mu\frac{\partial u_x}{\partial x} + 2\mu\frac{\partial u_y}{\partial y}\right) dz + \frac{\partial}{\partial y}\int_b^s \left(\mu\frac{\partial u_x}{\partial y} + \mu\frac{\partial u_y}{\partial x}\right) dz - \tau_{bx} = \rho g H\frac{\partial s}{\partial x},\\
&\frac{\partial}{\partial x}\int_b^s \left(\mu\frac{\partial u_x}{\partial y} + \mu\frac{\partial u_y}{\partial x}\right) dz + \frac{\partial}{\partial y}\int_b^s \left(4\mu\frac{\partial u_y}{\partial y} + 2\mu\frac{\partial u_x}{\partial x}\right) dz - \tau_{by} = \rho g H\frac{\partial s}{\partial y}.
\end{aligned} \tag{2.60}$$

The 'minus' signs (-) in τ_{bx} and τ_{by} mean the action is opposite to the ice flow (as considered in Eq. 2.52). The basal friction $\boldsymbol{\tau}_b$ is neglected in floating parts of the marine ice sheets. Although a shear stress exists due to the sea water circulation below the ice shelf, it is small in comparison to the shear stress present on the grounded part [61, 117]. Different formulations try to model the 'real' condition in the ice-bedrock interface. Some models are presented in Section 2.9. Here, we keep the generic notation (τ_{bx} and τ_{by}).

Since u_x and u_y are z-independent, Eqs. 2.60 is integrated in z, which finally yields:

$$\begin{aligned}
&\frac{\partial}{\partial x}\left(4H\bar{\mu}\frac{\partial u_x}{\partial x} + 2H\bar{\mu}\frac{\partial u_y}{\partial y}\right) + \frac{\partial}{\partial y}\left(H\bar{\mu}\frac{\partial u_x}{\partial y} + H\bar{\mu}\frac{\partial u_y}{\partial x}\right) - \tau_{bx} = \rho g H\frac{\partial s}{\partial x},\\
&\frac{\partial}{\partial x}\left(H\bar{\mu}\frac{\partial u_x}{\partial y} + H\bar{\mu}\frac{\partial u_y}{\partial x}\right) + \frac{\partial}{\partial y}\left(4H\bar{\mu}\frac{\partial u_y}{\partial y} + 2H\bar{\mu}\frac{\partial u_x}{\partial x}\right) - \tau_{by} = \rho g H\frac{\partial s}{\partial y},
\end{aligned} \tag{2.61}$$

where $\bar{\mu} = (1/H)\int_b^s \mu dz$ is the vertically integrated ice viscosity. Eqs. 2.61 are the desired SSA equations. Using a compact notation, we have:

$$\begin{aligned}
\mathrm{div}_{xy}\left(2H\bar{\mu}\dot{\boldsymbol{\varepsilon}}_x\right) - \tau_{bx} &= f_x,\\
\mathrm{div}_{xy}\left(2H\bar{\mu}\dot{\boldsymbol{\varepsilon}}_y\right) - \tau_{by} &= f_y,
\end{aligned} \tag{2.62}$$

with

$$\begin{aligned}
\dot{\boldsymbol{\varepsilon}}_x &= \begin{bmatrix} 2\dfrac{\partial u_x}{\partial x} + \dfrac{\partial u_y}{\partial y} \\ \dfrac{1}{2}\left(\dfrac{\partial u_x}{\partial y} + \dfrac{\partial u_y}{\partial x}\right) \end{bmatrix} = \begin{bmatrix} 2\dot{\varepsilon}_{xx} + \dot{\varepsilon}_{yy} \\ \dot{\varepsilon}_{xy} \end{bmatrix},\\
\dot{\boldsymbol{\varepsilon}}_y &= \begin{bmatrix} \dfrac{1}{2}\left(\dfrac{\partial u_x}{\partial y} + \dfrac{\partial u_y}{\partial x}\right) \\ \dfrac{\partial u_x}{\partial x} + 2\dfrac{\partial u_y}{\partial y} \end{bmatrix} = \begin{bmatrix} \dot{\varepsilon}_{yx} \\ \dot{\varepsilon}_{xx} + 2\dot{\varepsilon}_{yy} \end{bmatrix},
\end{aligned} \tag{2.63}$$

and

$$\begin{aligned}
f_x &= \rho g H\frac{\partial s}{\partial x},\\
f_y &= \rho g H\frac{\partial s}{\partial y}.
\end{aligned} \tag{2.64}$$

Note that $\mathrm{div}_{xy}(\cdot)$ indicates that the divergence operator is carried out only on the 2D xy-plane. The SSA formulation is a set of non-linear elliptic-type equations where a membrane-type stress balance (vertically integrated horizontal deviatoric stress) is solved.

Dirichlet-type boundary conditions (the velocity field is prescribed) complete the SSA equations. Neumann-type condition (water-ocean pressure) is applied at the ice-ocean contact in the calving front, as follows:

$$\begin{aligned} 2H\bar{\mu}\dot{\boldsymbol{\varepsilon}}_x \cdot \mathbf{n}_{if} &= \left(\frac{1}{2}\rho g H^2 - \frac{1}{2}\rho_w g b^2\right) n_{ifx}, \\ 2H\bar{\mu}\dot{\boldsymbol{\varepsilon}}_y \cdot \mathbf{n}_{if} &= \left(\frac{1}{2}\rho g H^2 - \frac{1}{2}\rho_w g b^2\right) n_{ify}, \end{aligned} \tag{2.65}$$

where $\mathbf{n}_{if}$ is the horizontal normal unit vector (see definition in Section 2.13).

The last variable to be prescribed is the effective strain rate, $\dot{\varepsilon}_e$. Then, for SSA formulation, Eq. 2.17 is simplified to:

$$\dot{\varepsilon}_e = \left[\left(\frac{\partial u_x}{\partial x}\right)^2 + \left(\frac{\partial u_y}{\partial y}\right)^2 + \frac{\partial u_x}{\partial x}\frac{\partial u_y}{\partial y} + \frac{1}{4}\left(\frac{\partial u_x}{\partial y} + \frac{\partial u_y}{\partial x}\right)^2\right]^{1/2}. \tag{2.66}$$

2.7 Shallow Ice Approximation

The Shallow Ice Approximation (SIA) is widely used in Glaciology, mainly due to its fast velocity field computation. However, its assumptions are stronger than any other Stokes' approximations, which may limit its applicability[2]. The SIA formulation is assigned to K. Hutter [74] and L. Morland [99]. Although we do not apply it in this work, its presentation is a didactic way to show the essential behavior of a glacier motion. The assumptions are based on the aspect ratio ϵ (Eq. 2.1), and the deduction is found in [61, 101]. The SIA assumptions are:

$$\tau_{xx} = \tau_{yy} = \tau_{zz} = \tau_{xy} = 0, \tag{2.67}$$

$$\begin{aligned} \frac{\partial u_z}{\partial x} &\ll \frac{\partial u_x}{\partial z}, \\ \frac{\partial u_z}{\partial y} &\ll \frac{\partial u_y}{\partial z}. \end{aligned} \tag{2.68}$$

In SIA, only horizontal shear stresses are considered, τ_{xz}, τ_{yz}, and the normal stresses are equal to the pressure, i.e., $\sigma_{xx} = \sigma_{yy} = \sigma_{zz} = -p$. These assumptions lead to a hydrostatic pressure:

$$\frac{\partial p}{\partial z} = -\rho g. \tag{2.69}$$

[2]In fact, the SIA formulation is only applied to grounded ice. The accuracy of SIA depends on the aspect ratio ϵ of the glacier/ice sheet. See discussion in [61, p.151].

and, from Eqs. 2.34(a,b), yields:

$$\begin{aligned} \frac{\partial \tau_{xz}}{\partial z} &= \rho g \frac{\partial s}{\partial x}, \\ \frac{\partial \tau_{yz}}{\partial z} &= \rho g \frac{\partial s}{\partial y}. \end{aligned} \tag{2.70}$$

Integrating Eqs. 2.70, we express the shear stresses along the vertical coordinate[3]:

$$\begin{aligned} \tau_{xz}(z) &= -\rho g (s - z) \frac{\partial s}{\partial x}, \\ \tau_{yz}(z) &= -\rho g (s - z) \frac{\partial s}{\partial y}. \end{aligned} \tag{2.71}$$

The horizontal components of the velocity field in SIA are[4]:

$$\begin{aligned} u_x(z) &= u_{bx} - 2(\rho g)^n \parallel \nabla s \parallel^{n-1} \frac{\partial s}{\partial x} \int_b^z A(T')(s - \zeta)^n \, d\zeta, \\ u_y(z) &= u_{by} - 2(\rho g)^n \parallel \nabla s \parallel^{n-1} \frac{\partial s}{\partial y} \int_b^z A(T')(s - \zeta)^n \, d\zeta, \end{aligned} \tag{2.72}$$

where the basal velocities u_{bx} and u_{by} can be written as[5]:

$$\begin{aligned} u_{bx} &= -C(\rho g H)^{(1-q)/m} \parallel \nabla s \parallel^{1/m-1} \frac{\partial s}{\partial x}, \\ u_{by} &= -C(\rho g H)^{(1-q)/m} \parallel \nabla s \parallel^{1/m-1} \frac{\partial s}{\partial y}, \end{aligned} \tag{2.73}$$

where n is the Glen's exponent (see Section 2.5), C is a positive coefficient (variable in space), m and q are positive constants. Therefore, in SIA, the horizontal velocities are only functions of the local variables, and follow the (opposite) surface gradient. Also, note that the balance of the driving and resistive forces is local (see Section 2.8).

2.8 Driving stress

The force vector in the SSA formulation (Eqs. 2.64) is called as the 'driving stress':

$$\begin{aligned} \tau_{dx} &= -\rho g H \frac{\partial s}{\partial x}, \\ \tau_{dy} &= -\rho g H \frac{\partial s}{\partial y}, \end{aligned} \tag{2.74}$$

The driving stress represents the force that drives the ice sheet/glacier movement, and is

[3]Note that a free condition at the ice surface (i.e., $\tau_{xz} \mid_s = \tau_{yz} \mid_s = 0$) is applied in Eqs. 2.71.

[4]The complete deduction can be found in [61, p.77].

[5]Considering a generalized Weertman-type (or Budd-type) model for the basal stress. See Section 2.9.

proportional to the ice surface gradient. In SIA, Eqs. 2.74 are the shear stresses at the ice base (see Eqs. 2.71). This reinforces the statement written in Section 2.7: the driving stress is balanced locally by the basal drag[6].

2.9 Basal friction

The choice of basal friction law in ice sheet models impacts not only the grounding line dynamics, but also future sea level projections [20, 55, 80, 97, 146]. The relation between the basal drag (τ_b) and basal velocities (u_b) is a theme of constant discussion [146]: in-situ observations are rare [61, p.157] and there are many processes interacting at the ice/bed interface [25]. A first model is assigned to J. Weertman, who demonstrated the following relation for ice sliding on a rigid bedrock [155]:

$$\tau_b = C u_b^m, \tag{2.75}$$

where C is a friction coefficient and m is a parameter (positive). An extension of Eq. 2.75 was carried by Budd and colleagues [21]:

$$\tau_b = C u_b^m N^q, \tag{2.76}$$

where N is the effective pressure at the ice/bed interface and q is another positive parameter. Relation 2.76, also called as generalized Weertman's model, is the most common friction law employed in ice sheet models [146].

The presence of water-filled cavities at the ice/bed interface bounds the maximum value of the basal drag [77]. The general form, called here as Schoof's model, is [134, 50, 90]:

$$\tau_b = \frac{C u_b^m N^q}{\left(1 + u_b \left(C/C_{max} N\right)^{1/m}\right)^m}, \tag{2.77}$$

where C_{max} corresponds to the upper bounded value of the relation τ_b/N. When $N \to \infty$, Eq. 2.77 yields $\tau_b \sim C u_b^m$, a Weertman-type law. When $N \to 0$, Eq. 2.77 results in $\tau_b \sim C_{max} N$, a Coulomb-type friction. The interpretation of this latter behavior is: at small N, water-filled cavities open, which decreases the roughness of the rigid bedrock.

Considering two types of friction regime at the base, Weertman and Coulomb, Tsai and colleagues proposed the following relation [150]:

$$\tau_b = min\left(C u_b^m, fN\right), \tag{2.78}$$

where f is a friction coefficient. Both Tsai and Schoof laws produce similar asymptotic behaviors. Figure 2.4 shows basal drag values as a function of sliding velocity and effective pressure for the friction laws exposed above.

[6]The basal drag for SIA is equal to the negative of the basal stress, i.e. $= \left[-\tau_{xz}(b),\ -\tau_{yz}(b)\right]^\intercal$. See Eqs. 2.71.

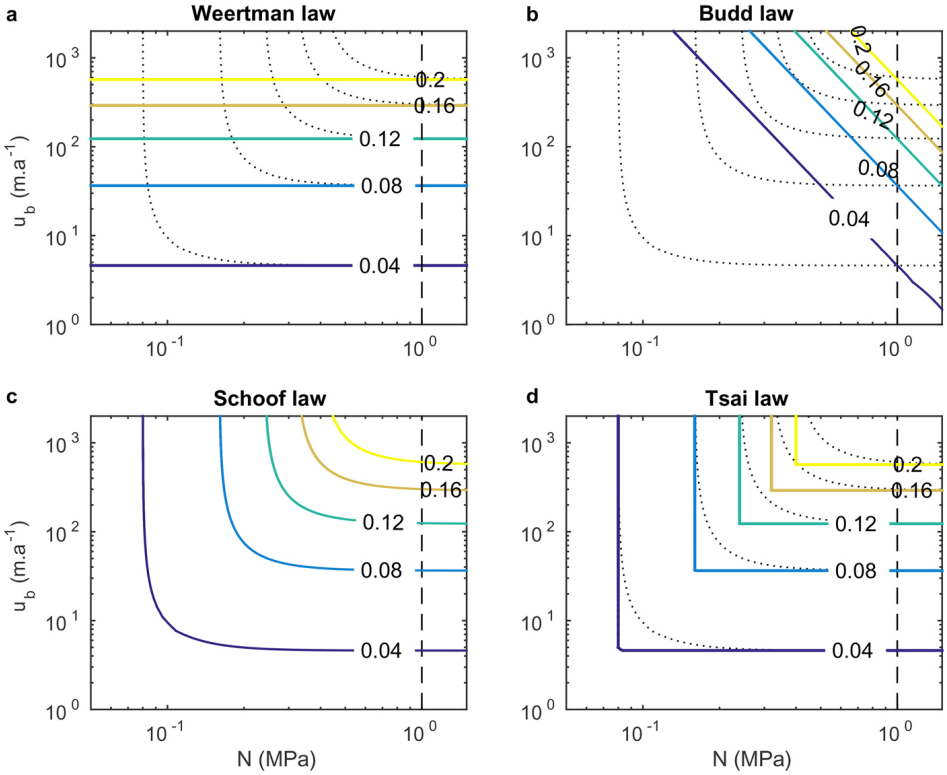

Figure 2.4: Values of the basal drag τ_b $(0.04-0.2\,MPa)$ as a function of the effective pressure N and sliding velocity u_b for the following friction laws: (a) Weertman, Eq. 2.75, (b) Budd, Eq. 2.76, (c) Schoof, Eq. 2.77 and (d) Tsai, Eq. 2.78. Parameter values used: $C = 7.624\times10^6$ (SI), $C_{max} = f = 0.5$, $m = 1/3$. Thin dotted lines are the basal drag values for the Schoof's law. Vertical thick black lines represent $N = 1\,MPa$. Figure from [20]. ©The Authors, 2017, distributed under a Creative Commons Attribution license (http://creativecommons.org/licenses/by/4.0/).

2.10 Scaling arguments of the ice flow

Since inertial forces are negligible in ice sheets and glaciers (see Section 2.4), the balance of forces acting on these ice masses should result in zero. In other words, ice sheets and glaciers are in a static equilibrium [28, p.295]. A first approximation is assuming that the driving stress is balanced by the basal stress. This balance is responsible for shaping glaciers and ice sheets. We demonstrate this using scaled variables. The driving stress (Eqs. 2.74) can be written as:

$$\tau_d \sim \rho g H_0 \frac{H_0}{L_0}, \tag{2.79}$$

where we approximate the surface gradient by the aspect ratio, i.e., $\nabla s \sim H_0/L_0$. Then, assuming the basal stress τ_b as the resistive force, we have:

$$\tau_b \sim \tau_d. \tag{2.80}$$

In fact, Eq. 2.80 is a first estimate of the basal stress. Experimental results show that the

ice deformation rates increase substantially when the effective stress exceeds $100\,kPa$ ($1\,bar$)[7]. This is mainly dictated by the non-linear Glen's law. Also, driving stresses obtained by actual geometries rarely exceed $100\,kPa$: more than 3/4 of the glacial areas[8] are under driving stresses below $1\,bar$ [97]. This threshold allows us to assume the basal stress at a constant value τ_0, like a 'perfectly plastic' behavior[9]. Then, from Eqs. 2.79 and 2.80, we can write:

$$\frac{H_0^2}{L_0} \sim const, \tag{2.81}$$

or

$$L_0 \sim H_0^2, \tag{2.82}$$

An immediate consequence of Eq. 2.82 is the aspect ratio of ice sheets and glaciers: the larger they are, the shallower they become. In fact, Eq. 2.82 can be written as:

$$\epsilon \sim \frac{1}{H_0}. \tag{2.83}$$

Another interesting consequence of assuming perfect plasticity is the relation between thickness and surface gradient. If $\tau_0 = 100\,kPa$, we have $\tau_0/\rho g \approx 11\,m$. Thus:

$$\nabla s H_0 \sim 11\,m, \tag{2.84}$$

what means that the ice thickness can be estimated by measurements of the surface slope. Relation 2.84 tell us the glacier is thin in the regions with high gradients, and vice versa.

Scaling arguments also allow us to compare driving stress with (ice) deformation stress. Then, the shear deformation and ice viscosity are written as (see Section 2.5):

$$\begin{aligned} \tau_s &\sim \mu_0 \frac{U_0}{H_0}, \\ \mu_0 &\sim \frac{1}{2A_0\tau_s^{n-1}}. \end{aligned} \tag{2.85}$$

Relation 2.85 estimates the stress τ_s needed to deform an ice body such that the observed surface velocities U_0 are matched. These simple calculations show that there is a scatter relation between τ_s and τ_d: about 50% of both Greenland and Antarctica areas present $\tau_s > \tau_d$ [97]. This means that the observed velocities are not explained only by internal shear deformation and, therefore, a basal sliding component may be present in such area. Sliding also occurs beneath glaciers and ice caps [97, and references therein]. The fundamental implication of this simple analysis is that basal sliding is a dominant process in glacial contributions to sea level rise, and subglacial processes involved in the ice-bed interface should be the major concern in ice sheet modeling.

[7] See Figure 2.3 and [28, p.61].

[8] Including Greenland, Antarctica and Alpine glaciers [97].

[9] Assuming ice as a perfectly plastic material, τ_0 means the yield stress. See Figure 2.3.

2.11 Transport equation

As we see in Section 2.4, the dynamics of a glacier/ice sheet is a quasi-static movement. It means that the glacier/ice sheet geometry defines the stress field, and consequently, the velocity field at any point in the ice body. The velocity field induces a new geometry since both ice surface and ice base are free boundaries. Additionally, a glacier/ice sheet gains and loses ice mass through the accumulation and ablation zones, respectively. These called external forces also induce a change in the ice geometry. Rarely a glacier/ice sheet is in a steady state condition: external forces follow climate fluctuations and a glacier/ice sheet has its own characteristic response time[10]. Therefore, if one wants to understand the evolution of a glacier/ice sheet, it is necessary to analyze the kinematics of the ice surface and ice base. As we see in Section 2.11.3, for the SSA formulation, the kinematics of both surface and base are combined to generate a transport equation of the ice thickness.

2.11.1 Ice surface

The ice surface $s\,(x,\ y,\ t)$ is expressed as an implicit function:

$$f_s\,(x,\ y,\ z,\ t) = z - s\,(x,\ y,\ t) = 0. \tag{2.86}$$

At a scenario with no accumulation neither ablation, the material derivative of f_s is:

$$\frac{df_s}{dt} = \frac{\partial f_s}{\partial t} + (\nabla f_s) \cdot \mathbf{u}_s = 0, \tag{2.87}$$

where $\mathbf{u}_s$ is the surface velocity. From Eq. 2.86, we have:

$$\frac{\partial s}{\partial t} = -\frac{\partial s}{\partial x} u_x \mid_s - \frac{\partial s}{\partial y} u_y \mid_s + u_z \mid_s . \tag{2.88}$$

Both accumulation and ablation change the rate of s in relation to time t. Then, inserting a surface mass balance (=accumulation-ablation) in Eq. 2.88 yields:

$$\frac{\partial s}{\partial t} = -\frac{\partial s}{\partial x} u_x \mid_s - \frac{\partial s}{\partial y} u_y \mid_s + u_z \mid_s + \dot{m}_s\,, \tag{2.89}$$

where $\dot{m}_s$ is the surface mass balance (SMB, positive for accumulation).

2.11.2 Ice base

Similar to Section 2.11.1, we define an implicit function to the ice base:

$$f_b\,(x,\ y,\ ,z,\ t) = z - b\,(x,\ y,\ t) = 0. \tag{2.90}$$

[10]The characteristic response time is the time for which a glacier takes to adjust its own geometry to a change in the external forcings (mass balance and/or climate conditions)[124].

Applying the material derivative in f_b and using Eq. 2.90, we have:

$$\frac{\partial b}{\partial t} = -\frac{\partial b}{\partial x} u_x \mid_b - \frac{\partial b}{\partial y} u_y \mid_b + u_z \mid_b . \tag{2.91}$$

Now, we insert a base mass balance in Eq. 2.91 to account refreezing and basal melting:

$$\frac{\partial b}{\partial t} = -\frac{\partial b}{\partial x} u_x \mid_b - \frac{\partial b}{\partial y} u_y \mid_b + u_z \mid_b + \dot{m}_b , \tag{2.92}$$

where $\dot{m}_b$ is the base mass balance (positive for melting).

2.11.3 Ice thickness

Equations 2.89 and 2.92 are combined to obtain a transport equation of the ice thickness, $H = s - b$. Thus, by subtracting Eq. 2.92 from Eq. 2.89, we have:

$$\frac{\partial s}{\partial t} - \frac{\partial b}{\partial t} = \frac{\partial H}{\partial t} = -\frac{\partial s}{\partial x} u_x \mid_s + \frac{\partial b}{\partial x} u_x \mid_b - \frac{\partial s}{\partial y} u_y \mid_s + \frac{\partial b}{\partial y} u_y \mid_b + u_z \mid_s - u_z \mid_b + \dot{m}_s - \dot{m}_b. \tag{2.93}$$

According to the Leibniz's rule, we have:

$$\frac{\partial}{\partial x} \int_b^s u_x dz = \int_b^s \frac{\partial u_x}{\partial x} dz + \frac{\partial s}{\partial x} u_x \mid_s - \frac{\partial b}{\partial x} u_x \mid_b . \tag{2.94}$$

Thus, by applying the same for u_y, and being $\int_b^s (\partial u_z / \partial z)\, dz = u_z \mid_s - u_z \mid_b$, Eq. 2.93 is rewritten as:

$$\frac{\partial H}{\partial t} = -\frac{\partial}{\partial x} \int_b^s u_x dz + \int_b^s \frac{\partial u_x}{\partial x} dz - \frac{\partial}{\partial y} \int_b^s u_y dz + \int_b^s \frac{\partial u_y}{\partial y} dz + \int_b^s \frac{\partial u_z}{\partial z} dz + \dot{m}_s - \dot{m}_b, \tag{2.95}$$

which can be simplified through the continuity equation. Then, we have:

$$\frac{\partial H}{\partial t} = -\frac{\partial}{\partial x} \int_b^s u_x dz - \frac{\partial}{\partial y} \int_b^s u_y dz + \dot{m}_s - \dot{m}_b. \tag{2.96}$$

Since it is assumed that both u_x and u_y are z-independent for the SSA formulation, we can integrate the horizontal velocities in z. Then, we finally have the ice thickness evolution equation:

$$\frac{\partial H}{\partial t} = -\mathrm{div}_{xy} \mathbf{Q} + \dot{m}_s - \dot{m}_b , \tag{2.97}$$

where $\mathbf{Q} = H\mathbf{u}_{xy}$ is the horizontal flux, being $\mathbf{u}_{xy} = \begin{bmatrix} u_x & u_y \end{bmatrix}^\intercal$ the horizontal velocities, which are functions of x, y and t. Eq. 2.97 is the fundamental evolution equation applied in glacier/ice sheet modeling.

2.11.4 Diffusion equation

An important consequence of the SIA formulation is a non-linear diffusion equation that arises from the ice thickness evolution equation. As we see, in SIA, horizontal velocities are functions

of the surface gradient, and they can be inserted in the ice thickness equation (Eq. 2.97). The horizontal flux from SIA velocities can be written as:

$$\begin{aligned} Q_x &= \int_b^s u_x dz = -D\frac{\partial s}{\partial x}, \\ Q_y &= \int_b^s u_y dz = -D\frac{\partial s}{\partial y}, \end{aligned} \tag{2.98}$$

where:

$$D = \int_b^s \left[C\left(\rho g H\right)^{p-q} \parallel \nabla s \parallel^{p-1} + 2\left(\rho g\right)^n \parallel \nabla s \parallel^{n-1} \int_b^z A\left(T'\right)\left(s-\zeta\right)^n d\zeta \right] dz. \tag{2.99}$$

Then, inserting Eq. 2.98 in the ice thickness equation (Eq. 2.97), and writing the ice surface as $s = H - b$, we have:

$$\frac{\partial H}{\partial t} = \mathrm{div}_{xy}\left[D\nabla\left(H-b\right)\right] + \dot{m}_s - \dot{m}_b. \tag{2.100}$$

Equation 2.100 is a non-linear diffusion equation of the ice thickness [76]. It means that the more a glacier's length increases (which makes SIA assumptions valid), the more its motion is diffusive[11].

2.12 Grounding line

Grounding line dynamics is the central motivation of this thesis, in the sense of applying adaptive mesh refinement. As we show in Section 1.2, the grounding line migration associated with the Marine Ice Sheet Instability hypothesis may potentially contribute to sea level rise, mainly due to the (potential) West Antarctic Ice Sheet collapse. Here, we attempt to show the theory of grounding line dynamics based on the main works of the literature.

As we see in Section 2.6, the ice flow in ice shelves is dictated by a membrane-like stress, which means that only horizontal stretching is accounted (SSA). On the other hand, as we see in Section 2.7, the ice flow in the grounded part of ice sheets occurs mainly due to the shear stress, with or without a basal slip component (SIA). Then, a so called 'transition zone' in ice flow exists around the grounding line. In a Stokes-like model, all these flow patterns are modeled, with the grounding line being a singular point in the basal boundary condition [98, 109]. Then, a contact-type problem arises in the Stokes equations in solving the grounding line migration, e.g., [109, 37]. Besides that, a fine mesh resolution is required to account accurately the ice flow in the transition zone and the grounding line migration, which is computationally prohibitive in large scale simulations [37, 39, 49]. Alternatively, the Shallow Ice and Shallow Shelf (Shelf-Stream) Approximations overcome the high computational cost of the Stokes equations with an acceptable accuracy[12], but the transition zone must be correctly treated when both SIA and SSA

[11] See also an interesting discussion in [44, p.624].

[12] It is important to note that both SIA and SSA have limitations, and for some glaciers the flow pattern is really 3D, which requires a High-Order model or even the Stokes equations.

equations are combined around the grounding line.

One of the first numerical studies on transition zone is from K. Herterich, in 1987 [67]. Herterich used simplified equations derived from the Stokes model to obtain a two-dimensional ice flow in the transition zone under different boundary conditions. He found the width of the transition zone is within the order of the ice thickness and the horizontal velocity present large gradients around the grounding line. R. Lestringant, in 1994 [92], carried out a similar study, but using the two-dimensional Stokes equations. His results shown clearly two flow patterns: the shallow ice (on the ice sheet) and the shallow shelf (on the ice shelf) regimes. Lestringant noted a very narrow transition zone between these two regimes (within the order of the ice thickness) where a strong horizontal gradient in the shear stress was present.

Pattyn and colleagues, in 2006 [117], studied the role of the transition zone in the dynamics of marine ice sheets. They used a two-dimensional High-Order model[13] and the ice thickness evolution equation[14] coupled to a grounding line migration model with subgrid accuracy. They changed the width of the transition zone by prescribing a spatial variation of the basal friction. Their results shown that the amplitude of the grounding line advance/retreat is a function of the transition zone length and that a neutral equilibrium[15] for the grounding line positions was observed for small transition zones. Unfortunately, their results may have been affected by a low grid resolution used in the numerical discretization, which may not have solved accurately small transition zones[16].

Nowicki and Wingham, in 2008 [109], analyzed steady state conditions for grounding line positions by solving the transition zone with the Stokes equations (considering linear viscosity) under two different basal boundary conditions: with and without slip. They noted a very thin 'transition zone' (2-3 $\times$ the ice thickness upstream to the grounding line), in which they applied a fine mesh resolution. Although they found a singular solution for the pressure at the base near the grounding line[17], they argued that the stress solution in that region was not affected by this singularity. Also, they noted high deviatoric stresses values around the grounding line. For the case with basal slip, they found a unique velocity solution for the given grounding line position. However, for the no-slip condition at the base, a range of ice flows for the same grounding line position were found.

Durand and colleagues, in 2009 [37], performed a similar study to Nowicki and Wingham. They solved the full Stokes with non-linear viscosity for an entire ice sheet coupled to the transport equations of the ice surface and ice base[18]. A contact problem was also applied to solve the grounding line migration. They analyzed the stability of a marine ice sheet under two different bedrock geometries. They found the ice sheet is unstable on bedrock with inland-deepening slopes. On a prograde bedrock slope, they noted that the 'neutral equilibrium' disappeared when high mesh resolution was applied in the grounding line vicinity (element size $< 100\,m$ in a domain of $1,800\,km$). Their results were in agreement with the semianalytical results from [136].

[13] The xz-version of Eqs. 2.43.

[14] See Section 2.11.3.

[15] Neutral equilibrium means that the grounding line presents infinite equilibrium positions. This hypothesis was proposed by R. Hindmarsh, in 1993 [68]. Nowadays, this hypothesis has been discarded [137, 136].

[16] See the discussion in [136, line 105].

[17] In fact, it is expected a singular solution of the type $p(x)\,|_b \sim O\left(x^{-1/2}\right)$.

[18] See Sections 2.11.1 and 2.11.2.

C. Schoof, in 2007 [137, 136], studied the role of the transition zone in controlling the marine ice sheet stability. He used an asymptotic analysis in the case of fast sliding ice sheets (with negligible internal shear stress) in opposition to a previous work of Chugunov and Wilchinsky [23, 157, 158], who studied the case of no basal sliding. The transition zone was treated as a boundary layer structure, and with matched asymptotic expansions he found an increasing function between the bedrock elevation and ice flux, both at the grounding line. He also found that there is no 'neutral equilibrium' in marine ice sheets, and there is no stable grounding line position on retrograde bedrock slope. Comparing his asymptotic result with a numerical model, Schoof pointed out that high mesh resolution, mainly in solving the transition zone, it is an important issue to achieve reliable numerical results.

Here, to illustrate, we are considering a marine ice sheet flowing by fast basal sliding, then shear stresses acting within the ice body are negligible (see assumptions in Section 2.6). Consequently, a diffusive-type equation arises in the grounded ice sheet. This can be shown considering a Weertman-type law for the basal friction (see Section 2.9):

$$\begin{aligned} \tau_{bx} &= -C u_b^{m-1} u_x, \\ \tau_{by} &= -C u_b^{m-1} u_y, \end{aligned} \tag{2.101}$$

where $u_b = \sqrt{u_x^2 + u_y^2}$ is the basal velocity magnitude; then, neglecting the longitudinal stress terms in the SSA equations (Eqs. 2.61), we have:

$$\begin{aligned} u_x &= -\frac{1}{C u_b^{m-1}} \rho g H \frac{\partial (H - b)}{\partial x}, \\ u_y &= -\frac{1}{C u_b^{m-1}} \rho g H \frac{\partial (H - b)}{\partial y}. \end{aligned} \tag{2.102}$$

Therefore, for the fast sliding case (for which we ignore the horizontal stress terms), the horizontal velocities, u_x and u_y, are functions of the ice surface gradient. From Eq. 2.97, it is possible to obtain a non-linear diffusion equation describing the ice thickness evolution. Note that the structure of this diffusion equation is the same of the diffusion equation (Eq. 2.100) obtained with SIA equations with no shear deformation. In general, the basal sliding tends to reduce the internal deformation, controlling the ice motion [97].

Both numerical and boundary layer studies described above produce similar results: the transition zone is very small compared to the ice sheet domain. Following [137, 136], this allows to solve only the grounded part of the ice sheet by the ice thickness diffusion equation (e.g., Eq. 2.100), provided that an additional boundary condition is employed to account the role of the transition zone. From the boundary layer results [137, 136], this boundary condition is the ice flux at the grounding line. This approach is used in some continental scale simulations (e.g. [123, 31, 116]), although the accuracy of this scheme is questionable [120].

The SSA formulation solves both grounded and floating parts, including the transition zone (where basal and longitudinal stresses have the same magnitude). However, as we see above, high resolution is required to solve accurately the transition zone. The grounding line position in the SSA formulation can be defined by an implicit level set function ϕ_{gl} based on the floatation

criteria, as follows:

$$\phi_{gl} = \rho H + \rho_w r, \tag{2.103}$$

where r is the bedrock elevation (negative if below sea level). Then, the position of the grounding line is defined as:

$$\begin{cases} \phi_{gl} > 0: & \text{ice is grounded} \\ \phi_{gl} < 0: & \text{ice is floating} \\ \phi_{gl} = 0: & \text{grounding line position} \end{cases}. \tag{2.104}$$

The level set function ϕ_{gl} defines the changes in the basal boundary condition, i.e., the basal friction. For $\phi_{gl} < 0$, $\tau_{bx} = \tau_{by} = 0$. The basal friction for $\phi_{gl} = 0$ is a numerical matter, and depends on the discretization type of the domain. In Section 3.5 there are some details about how ISSM deals with this issue.

A free floating ice shelf does not impact the attached upstream grounded ice [136]. As free we mean that the ice shelf is not confined in a bay neither fixed on pinning points[19]. On the other hand, a confined ice shelf leads to an important interaction with the ice sheet/glacier through the 'backstress': the stress resulting from the lateral (basal) friction exerted by the boundaries of a bay (pinning points) [42]. The backstress 'buttresses' the ice sheet, stabilizing the grounded ice and decreasing the ice flow speed [36]. Therefore, the effect of the buttressing is in extending inland the transition zone and stabilizing the grounding line on retrograde bed slopes [136, 62]. In fact, an increasing in the ice velocities and mass losses were observed in the tributary glaciers of the Larsen B Ice Shelf, Antarctic Peninsula, after its collapse in 2002 [127, 16, 85].

2.13 Ice front

The ice front (or calving front) is another place where the adaptive mesh refinement can be applied. As suggested by [61, p.116] and implemented by [19], the position of the ice front can be determined by a level set function ϕ_{if}, in a similar approach used for the grounding line position:

$$\begin{cases} \phi_{if} > 0: & \text{no ice} \\ \phi_{if} < 0: & \text{presence of ice} \\ \phi_{if} = 0: & \text{ice front position} \end{cases}. \tag{2.105}$$

The evolution of the ice front can be determined through a 'kinematic condition' [61, p.116], which is given by the material derivative of level set ϕ_{if}:

$$\frac{d\phi_{if}}{dt} = \frac{\partial \phi_{if}}{\partial t} + \mathbf{u}_{if} \cdot \nabla \phi_{if} = 0, \tag{2.106}$$

where $\mathbf{u}_{if} = \left[u_{ifx}\, u_{ify}\right]^{\intercal}$ is the ice front (calving front) velocity, which can be related to the ice velocity at the ice front, $\mathbf{u}\,|_{if}$, as:

$$c = \left(\mathbf{u}\,|_{if} - \mathbf{u}_{if}\right) \cdot \mathbf{n}_{if}, \tag{2.107}$$

where c is the 'calving rate', i.e., the rate by which ice is lost by 'physical release' at the ice

[19] Pinning points are isolated bedrock elevations that touch the floating ice.

front, and $\mathbf{n}_{if}$ is the horizontal normal unit vector, defined as:

$$\mathbf{n}_{if} = \frac{\nabla \phi_{if}}{\| \nabla \phi_{if} \|} = \frac{\nabla \phi_{if}}{N_{if}}. \tag{2.108}$$

Through the calving rate expression (Eq. 2.107) and Eq. 2.108, Eq. 2.106 is rewritten as:

$$\frac{\partial \phi_{if}}{\partial t} + \mathbf{u} \cdot \nabla \phi_{if} = c N_{if}, \tag{2.109}$$

The solution of Eq. 2.109 gives the evolution of level set ϕ_{if}, considering that both ice velocity and calving rate are calculated in advance. More details about the level set method can be found in [113, 141].

Chapter 3

Implementation of adaptive mesh refinement in the Ice Sheet System Model

3.1 Introduction

We describe in this chapter a brief introduction to finite element method, which is used to solve the SSA formulation, the main features of the Ice Sheet System Model (ISSM) architecture, an overview of the adaptive mesh refinement (AMR) technique, and the implementation of this technique and refinement criteria in ISSM.

3.2 Finite element spaces on triangles

The meshes used in this work are based on a Delaunay-like triangulation. Then, the finite element spaces should be constructed on triangular elements. The finite element space used here is based on polynomials $\mathscr{P}$ of degrees p defined as:

$$\mathscr{P}_p = \text{span}\left\{x^m y^n,\ 0 \leq m,\ n,\ m+n \leq p\right\}. \tag{3.1}$$

Specifically, we work with $p = 1$ and, therefore, the $\mathscr{P}_1$ polynomials build the finite element space in ISSM[1]. There are some important assumptions on the meshes before building the finite element space. We are following [2, p.9]. Let Ω be a polygonal domain with boundary Γ. A finite element partition $\mathcal{P}$ of Ω is a set of elements $\{K\}$ such that:

(1) Each element is a triangle contained in Ω;

(2) The elements form a partition of the domain: $\bar{\Omega} = \cup_{K\in\mathcal{P}}\bar{K}$;

(3) The nonempty intersection of the closure of each distinct pair of elements is either a single common vertex or a single common edge of both elements.

The regularity κ_K of a triangle K is defined as:

$$\kappa_K = \frac{h_K}{\varrho_K}, \tag{3.2}$$

[1]There are $p = 2$ polynomials in ISSM, but these are not considered in this thesis.

where h_K is the diameter of the triangle (= $\sup_{x,\, y \in K} \parallel x - y \parallel$) and ϱ_K is the diameter of the largest circle that my be inscribed in K. A partition $\mathcal{P}$ is said to be 'regular' if there is a constant κ such that:

$$\kappa_K \leq \kappa, \ \forall K \in \Omega. \tag{3.3}$$

More generally, regular families of partitions consist of partitions composed by elements for which the regularity κ_K is uniformly bounded over the whole family [2, p.9]. In the literature, this property is referred as the 'shape regularity' of the elements. The regularity assumption allows partitions of the domain Ω into meshes that may be very highly locally refined containing elements of quite different sizes. The assumption of regularity indeed includes meshes generated by an adaptive refinement procedure: elements where the solution is nonsmooth may be refined at every step of the procedure, while other elements may not be refined [2, p.9].

The finite element space associated with the partition $\mathcal{P}$ is defined by continuous piecewise polynomials:

$$\mathcal{V} = \left\{ v \in C\left(\bar{\Omega}\right) : \forall K \in \mathcal{P}, \ v \mid_K \in \mathscr{P}_1 \right\}. \tag{3.4}$$

We define a basis for the space $\mathcal{V}$ composed by functions $\{\Phi_i : i \in N\}$ that satisfies the following conditions:

(1) $\Phi_i \in \mathcal{V}$ for all $i \in N$;

(2) $\Phi_i(\mathbf{x}_j) = \delta_{ij}$ for all $i, \ j \in N$, where δ_{ij} is the Kronecker symbol;

where $\left\{\mathbf{x}_j\right\}$ is the set of vertices existing in the given partition, Here, N is a natural number accounting for the existing number of vertices in the partition. This basis is referred as the '$\mathscr{P}_1$ Lagrange basis'. Therefore, in $\mathscr{P}_1$ Lagrange basis, the degrees of freedom of the space $\mathcal{V}$ is identified by function evaluations at the vertices of the elements presents in the partition.

The numerical implementation of the space $\mathcal{V}$ using $\mathscr{P}_1$ Lagrange basis is carried out through a 'reference element'[2]. For triangular elements, the reference element is defined as:

$$\hat{K} = \{(\hat{x}, \ \hat{y}) : 0 \leq \hat{x} \leq x, \ 0 \leq \hat{y} \leq 1 - \hat{x}\}. \tag{3.5}$$

Each triangular element K is related to the reference element $\hat{K}$ under a continuous, affine, invertible transformation $\mathcal{F}_K$ written as:

$$\mathcal{F}_K(\hat{\mathbf{x}}) = \mathbf{A}_K \hat{\mathbf{x}} + \mathbf{b}_k, \tag{3.6}$$

where $\hat{\mathbf{x}} = [\hat{x} \ \hat{y}]^\intercal$, $\mathbf{A}_K$ is a matrix and $\mathbf{b}_K$ is a vector. The regularity of the element K implies that $\mathbf{A}_K$ is nonsingular, and there is a constant C that depends only on the regularity parameter κ_K such that [2, p.9]:

$$\begin{cases} \parallel \mathbf{A}_K \parallel \leq C h_k \\ \parallel \mathbf{A}_K^{-1} \parallel \leq C \varrho_k^{-1} \\ C\varrho_k^2 \leq |\det(\mathbf{A}_K)| \leq C h_k^2 \end{cases}, \tag{3.7}$$

[2] Also named as 'master element'.

where $\|\cdot\|$ is a matrix norm.

The $\mathscr{P}_1$ Lagrange basis functions[3] $\left\{\hat{\Phi}_i(\hat{\mathbf{x}}),\ i = 1,\ 2,\ 3\right\}$ of the space $\mathcal{V}$ defined in the reference element $\hat{K}$ (Eq. 3.5) are:

$$\begin{cases} \hat{\Phi}_1(\hat{x},\ \hat{y}) = 1 - \hat{x} - \hat{y} \\ \hat{\Phi}_2(\hat{x},\ \hat{y}) = \hat{x} \\ \hat{\Phi}_3(\hat{x},\ \hat{y}) = \hat{y} \end{cases}. \tag{3.8}$$

Considering the edges of an element K remain straight, a possible transformation $\mathcal{F}_K$ is written as[4]:

$$\mathcal{F}_K(\hat{\mathbf{x}}) = \begin{bmatrix} x \\ y \end{bmatrix} = \begin{bmatrix} x_2 - x_1 & x_3 - x_1 \\ y_2 - y_1 & y_3 - y_1 \end{bmatrix} \begin{bmatrix} \hat{x} \\ \hat{y} \end{bmatrix} + \begin{bmatrix} x_1 \\ y_1 \end{bmatrix}, \tag{3.9}$$

where $\{x_i,\ y_i,\ i = 1,\ 2,\ 3\}$ are the vertices' coordinates of element K. Transformation 3.9 can be written as:

$$\mathcal{F}_K(\hat{\mathbf{x}}) = \begin{cases} x = (x_2 - x_1)\hat{x} + (x_3 - x_1)\hat{y} + x_1 \\ y = (y_2 - y_1)\hat{x} + (y_3 - y_1)\hat{y} + y_1 \end{cases}, \tag{3.10}$$

or, after some rearrangement, as:

$$\mathcal{F}_K(\hat{\mathbf{x}}) = \begin{cases} x = (1 - \hat{x} - \hat{y})x_1 + \hat{x}x_2 + \hat{y}x_3 = \displaystyle\sum_{i=1}^{3} x_i\hat{\Phi}_i \\ \\ y = (1 - \hat{x} - \hat{y})y_1 + \hat{x}y_2 + \hat{y}y_3 = \displaystyle\sum_{i=1}^{3} y_i\hat{\Phi}_i \end{cases}. \tag{3.11}$$

The application of the $\mathscr{P}_1$ basis functions to the geometric transformation $\mathcal{F}_K$ (Eq.3.11) illustrates the attractive features of implementations based on reference elements: the basis functions of the reference elements are used to construct both the finite element space and the geometry of the elements[5].

It is important to note that the space $\mathcal{V}$ defined by 3.4 composed by functions $\{\Phi_i : i \in N\}$ is in fact a subspace of the class of functions H^1 (see Appendix A). Note that we don't fix the values of the basis functions at the boundary of the domain as carried out in Appendix A (definition of H_0^1); then we exclude the subscript 0 in the space H^1 notation.

The matrix $\mathbf{A}_K$ is also known in the literature as the Jacobian matrix[6], $\mathbf{J}$, which contains all the first-order partial derivatives of the linear transformation $\mathcal{F}_K(\hat{\mathbf{x}})$, i.e., $J_{ij} = \partial\mathcal{F}_{K,\,j}/\partial x_i$[7]. The determinant of $\mathbf{J}$ represents the ratio between the areas of the 'distorted' and reference elements.

---

[3] Also named in the literature as shape functions.

[4] This is verified by setting: $\mathcal{F}_K(0,\ 0) = (x_1,\ y_1)$, $\mathcal{F}_K(1,\ 0) = (x_2,\ y_2)$, $\mathcal{F}_K(0,\ 1) = (x_3,\ y_3)$.

[5] Here, we are working with the concept of 'isoparametric' elements, in the sense that the same basis functions are used to represent both approximation space and geometric description of the elements.

[6] Or as the transpose of the Jacobian matrix.

[7] In fact, the most common definition of the Jacobian matrix is $J_{ij} = \partial\mathcal{F}_{K,\,i}/\partial x_j$.

3.3 Finite element formulation

In this section we describe the finite element formulations for the SSA stress balance equations and ice thickness evolution equation.

The SSA stress balance problem is summarized as: find $\mathbf{u}(\mathbf{x}) = \left[u_x(x,\, y)\, u_y(x,\, y)\right]^\intercal$ such that:

$$
\begin{cases}
\operatorname{div}\left(2H\bar{\mu}\dot{\boldsymbol{\varepsilon}}_x\right) - \tau_{bx} = f_x \\
\operatorname{div}\left(2H\bar{\mu}\dot{\boldsymbol{\varepsilon}}_y\right) - \tau_{by} = f_y \\
\mathbf{u} = \mathbf{u}_0 \text{ on } \Gamma_D \\
2H\bar{\mu}\dot{\boldsymbol{\varepsilon}}_x \cdot \mathbf{n}_{\Gamma_N} = \left(\dfrac{1}{2}\rho g H^2 - \dfrac{1}{2}\rho_w g b^2\right) n_{\Gamma_{Nx}} \text{ on } \Gamma_N \\
2H\bar{\mu}\dot{\boldsymbol{\varepsilon}}_y \cdot \mathbf{n}_{\Gamma_N} = \left(\dfrac{1}{2}\rho g H^3 - \dfrac{1}{2}\rho_w g b^2\right) n_{\Gamma_{Ny}} \text{ on } \Gamma_N \\
\dot{\boldsymbol{\varepsilon}}_x = \begin{bmatrix} 2\dfrac{\partial u_x}{\partial x} + \dfrac{\partial u_y}{\partial y} \\ \dfrac{1}{2}\left(\dfrac{\partial u_x}{\partial y} + \dfrac{\partial u_y}{\partial x}\right) \end{bmatrix},\ \dot{\boldsymbol{\varepsilon}}_y = \begin{bmatrix} \dfrac{1}{2}\left(\dfrac{\partial u_x}{\partial y} + \dfrac{\partial u_y}{\partial x}\right) \\ \dfrac{\partial u_x}{\partial x} + 2\dfrac{\partial u_y}{\partial y} \end{bmatrix} \\
f_x = \rho g H \dfrac{\partial s}{\partial x},\ f_y = \rho g H \dfrac{\partial s}{\partial y} \\
\bar{\mu} = (1/H)\displaystyle\int_b^s \mu\, dz,\ \ \mu = \dfrac{B}{2\dot{\varepsilon}_e^{1-1/n}} \\
\dot{\varepsilon}_e = \left[\left(\dfrac{\partial u_x}{\partial x}\right)^2 + \left(\dfrac{\partial u_y}{\partial y}\right)^2 + \dfrac{\partial u_x}{\partial x}\dfrac{\partial u_y}{\partial y} + \dfrac{1}{4}\left(\dfrac{\partial u_x}{\partial y} + \dfrac{\partial u_y}{\partial x}\right)^2\right]^{1/2}
\end{cases}
, \tag{3.12}
$$

where Γ_D and Γ_N represent the parts of the boundary Γ of domain Ω in which Dirichlet and Neumann boundary conditions are applied, respectively. Note that we exclude the xy-plane notation in the divergence operator (see Eq. 2.62).

The finite element space for the velocity field $\mathbf{u}$ is defined as:

$$
\mathcal{V}_\mathbf{u} = \left\{\boldsymbol{\upsilon} \in (\mathcal{V})^2,\, \boldsymbol{\upsilon} = \mathbf{u}_0 \text{ on } \Gamma_D\right\}, \tag{3.13}
$$

where $\mathcal{V}$ is defined by Eq. 3.4. The test functions $\boldsymbol{\upsilon} = \left[\upsilon_x\, \upsilon_y\right]^\intercal$ are vectors where each component is a function that belongs to space $\mathcal{V}$. Although the SSA problem has two components of stress balance, the finite element formulation of Eq. 3.12 is carried out using the same procedure shown in Appendix A. Then, applying a dot product between the two SSA stress equations and a test function $\boldsymbol{\upsilon} \in \mathcal{V}_\mathbf{u}$, and integrating over the domain Ω, the resulting variational formulation is:

$$
\begin{aligned}
\int_\Omega \left[\operatorname{div}\left(2H\bar{\mu}\dot{\boldsymbol{\varepsilon}}_x\right)\upsilon_x + \operatorname{div}\left(2H\bar{\mu}\dot{\boldsymbol{\varepsilon}}_y\right)\upsilon_y - \tau_{bx}\upsilon_x - \tau_{by}\upsilon_y\right] d\Omega \\
= \int_\Omega \left(f_x\upsilon_x + f_y\upsilon_y\right) d\Omega.
\end{aligned} \tag{3.14}
$$

Integrating Eq. 3.14 by parts and applying a tensor property, we have:

$$\int_{\Omega} \left[\operatorname{div}\left(2H\bar{\mu}\dot{\boldsymbol{\varepsilon}}_x \upsilon_x\right) - 2H\bar{\mu}\dot{\boldsymbol{\varepsilon}}_x \cdot \nabla\upsilon_x + \operatorname{div}\left(2H\bar{\mu}\dot{\boldsymbol{\varepsilon}}_y \upsilon_y\right) - 2H\bar{\mu}\dot{\boldsymbol{\varepsilon}}_y \cdot \nabla\upsilon_y - \tau_{bx}\upsilon_x - \tau_{by}\upsilon_y \right] d\Omega = \int_{\Omega} \left(f_x\upsilon_x + f_y\upsilon_y\right) d\Omega. \tag{3.15}$$

Applying the Gauss' theorem in the divergence operator in Eq. 3.15 and rearranging the terms, the variational formulation of the SSA equations is:

$$\begin{aligned} \int_{\Omega} \left(2H\bar{\mu}\dot{\boldsymbol{\varepsilon}}_x \cdot \nabla\upsilon_x + 2H\bar{\mu}\dot{\boldsymbol{\varepsilon}}_y \cdot \nabla\upsilon_y + \tau_{bx}\upsilon_x + \tau_{by}\upsilon_y\right) d\Omega \\ = \int_{\Gamma_N} \left(2H\bar{\mu}\dot{\boldsymbol{\varepsilon}}_x \upsilon_x + 2H\bar{\mu}\dot{\boldsymbol{\varepsilon}}_y \upsilon_y\right) d\Gamma \\ - \int_{\Omega} \left(f_x\upsilon_x + f_y\upsilon_y\right) d\Omega. \end{aligned} \tag{3.16}$$

The Galerkin's approximation is reached by searching the solution of Eq. 3.16 in a finite subspace $\mathcal{V}_{\mathbf{u}}^N$ of $\mathcal{V}_{\mathbf{u}}$. Then, Eq. 3.16 is written as:

$$\begin{aligned} \int_{\Omega} \left(2H\bar{\mu}\dot{\boldsymbol{\varepsilon}}_{Nx} \cdot \nabla\upsilon_{Nx} + 2H\bar{\mu}\dot{\boldsymbol{\varepsilon}}_{Ny} \cdot \nabla\upsilon_{Ny} + \tau_{bx}\upsilon_{Nx} + \tau_{by}\upsilon_{Ny}\right) d\Omega \\ = \int_{\Gamma_N} \left(2H\bar{\mu}\dot{\boldsymbol{\varepsilon}}_{Nx} \upsilon_{Nx} + 2H\bar{\mu}\dot{\boldsymbol{\varepsilon}}_{Ny} \upsilon_{Ny}\right) d\Gamma \\ - \int_{\Omega} \left(f_x\upsilon_{Nx} + f_y\upsilon_{Ny}\right) d\Omega, \end{aligned} \tag{3.17}$$

where:

$$\dot{\boldsymbol{\varepsilon}}_{Nx} = \begin{bmatrix} 2\dfrac{\partial u_{Nx}}{\partial x} + \dfrac{\partial u_{Ny}}{\partial y} \\ \dfrac{1}{2}\left(\dfrac{\partial u_{Nx}}{\partial y} + \dfrac{\partial u_{Ny}}{\partial x}\right) \end{bmatrix},$$

$$\dot{\boldsymbol{\varepsilon}}_{Ny} = \begin{bmatrix} \dfrac{1}{2}\left(\dfrac{\partial u_{Nx}}{\partial y} + \dfrac{\partial u_{Ny}}{\partial x}\right) \\ \dfrac{\partial u_{Nx}}{\partial x} + 2\dfrac{\partial u_{Ny}}{\partial y} \end{bmatrix}. \tag{3.18}$$

Inserting Eqs. 3.18 in Eq. 3.17, we have:

$$\begin{aligned}\int_\Omega 2H\bar{\mu}\left(2\frac{\partial u_{Nx}}{\partial x}+\frac{\partial u_{Ny}}{\partial y}\right)\frac{\partial v_{Nx}}{\partial x}+H\bar{\mu}\left(\frac{\partial u_{Nx}}{\partial y}+\frac{\partial u_{Ny}}{\partial x}\right)\frac{\partial v_{Nx}}{\partial y}\\ +H\bar{\mu}\left(\frac{\partial u_{Nx}}{\partial y}+\frac{\partial u_{Ny}}{\partial x}\right)\frac{\partial v_{Ny}}{\partial x}+2H\bar{\mu}\left(\frac{\partial u_{Nx}}{\partial x}+2\frac{\partial u_{Ny}}{\partial y}\right)\frac{\partial v_{Ny}}{\partial y}\\ +\tau_{bx}v_{Nx}+\tau_{by}v_{Ny}\,d\Omega\\ =\int_{\Gamma_N}\left(2H\bar{\mu}\dot{\boldsymbol{\varepsilon}}_{Nx}\,v_{Nx}+2H\bar{\mu}\dot{\boldsymbol{\varepsilon}}_{Ny}\,v_{Ny}\right)d\Gamma\\ -\int_\Omega\left(f_x v_{Nx}+f_y v_{Ny}\right)d\Omega.\end{aligned} \tag{3.19}$$

Since both approximate solution $\left[u_{Nx}\,u_{Ny}\right]^\intercal$ and test function $\left[v_{Nx}\,v_{Ny}\right]^\intercal$ are written as a linear combination of basis functions of subspace $\mathcal{V}_{\mathbf{u}}^N$, i.e.:

$$\begin{aligned}v_{Nx}(x,y)=\sum_{i=1}^{N}\beta_{xi}\Phi_i(x,y),\quad v_{Ny}(x,y)=\sum_{i=1}^{N}\beta_{yi}\Phi_i(x,y),\\ u_{Nx}(x,y)=\sum_{j=1}^{N}\alpha_{xj}\Phi_j(x,y),\quad u_{Ny}(x,y)=\sum_{j=1}^{N}\alpha_{yj}\Phi_j(x,y),\end{aligned} \tag{3.20}$$

we rewrite Eq. 3.19 as:

$$\begin{aligned}\int_\Omega 4H\bar{\mu}\frac{\partial}{\partial x}\left(\sum_{j=1}^{N}\alpha_{xj}\Phi_j\right)\frac{\partial}{\partial x}\left(\sum_{i=1}^{N}\beta_{xi}\Phi_i\right)+2H\bar{\mu}\frac{\partial}{\partial y}\left(\sum_{j=1}^{N}\alpha_{yj}\Phi_j\right)\frac{\partial}{\partial x}\left(\sum_{i=1}^{N}\beta_{xi}\Phi_i\right)\\ +H\bar{\mu}\frac{\partial}{\partial y}\left(\sum_{j=1}^{N}\alpha_{xj}\Phi_j\right)\frac{\partial}{\partial y}\left(\sum_{i=1}^{N}\beta_{xi}\Phi_i\right)+H\bar{\mu}\frac{\partial}{\partial x}\left(\sum_{j=1}^{N}\alpha_{yj}\Phi_j\right)\frac{\partial}{\partial y}\left(\sum_{i=1}^{N}\beta_{xi}\Phi_i\right)\\ +H\bar{\mu}\frac{\partial}{\partial y}\left(\sum_{j=1}^{N}\alpha_{xj}\Phi_j\right)\frac{\partial}{\partial x}\left(\sum_{i=1}^{N}\beta_{yi}\Phi_i\right)+H\bar{\mu}\frac{\partial}{\partial x}\left(\sum_{j=1}^{N}\alpha_{yj}\Phi_j\right)\frac{\partial}{\partial x}\left(\sum_{i=1}^{N}\beta_{yi}\Phi_i\right)\\ +2H\bar{\mu}\frac{\partial}{\partial x}\left(\sum_{j=1}^{N}\alpha_{xj}\Phi_j\right)\frac{\partial}{\partial y}\left(\sum_{i=1}^{N}\beta_{yi}\Phi_i\right)+4H\bar{\mu}\frac{\partial}{\partial y}\left(\sum_{j=1}^{N}\alpha_{yj}\Phi_j\right)\frac{\partial}{\partial y}\left(\sum_{i=1}^{N}\beta_{yi}\Phi_i\right)\\ +\tau_{bx}\sum_{i=1}^{N}\beta_{xi}\Phi_i+\tau_{by}\sum_{i=1}^{N}\beta_{yi}\Phi_i\,d\Omega\\ =\int_{\Gamma_N}\left(2H\bar{\mu}\dot{\boldsymbol{\varepsilon}}_{Nx}\,v_{Nx}+2H\bar{\mu}\dot{\boldsymbol{\varepsilon}}_{Ny}\,v_{Ny}\right)d\Gamma\\ -\int_\Omega\left(f_x\sum_{i=1}^{N}\beta_{xi}\Phi_i+f_y\sum_{i=1}^{N}\beta_{yi}\Phi_i\right)d\Omega.\end{aligned} \tag{3.21}$$

The resulting system of (non-linear) equations of Eq. 3.21 is:

$$\mathbf{K}\boldsymbol{\alpha}=\mathbf{F}, \tag{3.22}$$

where $\mathbf{K}$ and $\mathbf{F}$ are the stiffness matrix and load vector, respectively, defined as:

$$\begin{aligned}
K_{ij} = \int_\Omega & 4H\bar{\mu}\frac{\partial}{\partial x}\left(\sum_{i=1}^{N}\Phi_i\right)\frac{\partial}{\partial x}\left(\sum_{j=1}^{N}\Phi_j\right) + 2H\bar{\mu}\frac{\partial}{\partial y}\left(\sum_{i=1}^{N}\Phi_i\right)\frac{\partial}{\partial x}\left(\sum_{j=1}^{N}\Phi_j\right) \\
& + H\bar{\mu}\frac{\partial}{\partial y}\left(\sum_{i=1}^{N}\Phi_i\right)\frac{\partial}{\partial y}\left(\sum_{j=1}^{N}\Phi_j\right) + H\bar{\mu}\frac{\partial}{\partial x}\left(\sum_{i=1}^{N}\Phi_i\right)\frac{\partial}{\partial y}\left(\sum_{j=1}^{N}\Phi_j\right) \\
& + H\bar{\mu}\frac{\partial}{\partial y}\left(\sum_{i=1}^{N}\Phi_i\right)\frac{\partial}{\partial x}\left(\sum_{j=1}^{N}\Phi_j\right) + H\bar{\mu}\frac{\partial}{\partial x}\left(\sum_{i=1}^{N}\Phi_i\right)\frac{\partial}{\partial x}\left(\sum_{j=1}^{N}\Phi_j\right) \\
& + 2H\bar{\mu}\frac{\partial}{\partial x}\left(\sum_{i=1}^{N}\Phi_i\right)\frac{\partial}{\partial y}\left(\sum_{j=1}^{N}\Phi_j\right) + 4H\bar{\mu}\frac{\partial}{\partial y}\left(\sum_{i=1}^{N}\Phi_i\right)\frac{\partial}{\partial y}\left(\sum_{j=1}^{N}\Phi_j\right) \\
& + \tau_{bx}\sum_{i=1}^{N}\Phi_i + \tau_{by}\sum_{i=1}^{N}\Phi_i \, d\Omega, \\
F_i = \int_{\Gamma_N} & \left(2H\bar{\mu}\dot{\boldsymbol{\varepsilon}}_{Nx}\,\upsilon_{Nx} + 2H\bar{\mu}\dot{\boldsymbol{\varepsilon}}_{Ny}\,\upsilon_{Ny}\right) d\Gamma \\
& - \int_\Omega \left(f_x\sum_{i=1}^{N}\Phi_i + f_y\sum_{i=1}^{N}\Phi_i\right) d\Omega.
\end{aligned} \tag{3.23}$$

It is important to note that Eq. 3.22 is a non-linear system of equations, since both ice viscosity $\bar{\mu}$ and basal stress $\boldsymbol{\tau}_b$ are functions of the velocity field, i.e., $\mathbf{K} = \mathbf{K}(\boldsymbol{\alpha})$.

Analogously, the finite element space for the ice thickness H evolution is:

$$\mathcal{V}_H = \{\upsilon \in \mathcal{V},\ \upsilon = H_0 \text{ on } \Gamma_D\}\,. \tag{3.24}$$

The ice thickness evolution problem is summarized as: find $H = H(x,\ y,\ t)$ such that:

$$\begin{cases} \dfrac{\partial H}{\partial t} = -\mathrm{div}\mathbf{Q} + \dot{m}_s - \dot{m}_b \\ \mathbf{Q} = H\mathbf{u} \\ H = H_i \text{ at } t = 0 \end{cases}. \tag{3.25}$$

For numerical stabilization purposes, the advection-type ice thickness equation is modified by adding an artificial diffusion term. Then, the modified ice thickness evolution problem is: find H such that:

$$\begin{cases} \dfrac{\partial H}{\partial t} = -\mathrm{div}\mathbf{Q} + \mathrm{div}\left(\mathcal{D}\nabla H\right) + \dot{m}_s - \dot{m}_b \\ \mathbf{Q} = H\mathbf{u} \\ \mathcal{D} = \dfrac{h}{2}\begin{bmatrix} |u_x| & 0 \\ 0 & |u_y| \end{bmatrix} \\ H = H_i \text{ at } t = 0 \end{cases}, \tag{3.26}$$

where $\mathcal{D}$ is the artificial diffusion coefficient and h is the characteristic size of the elements[8]. Multiplying Eq.3.26 by a test function $\upsilon \in \mathcal{V}_H$, integrating over domain Ω and applying the integrating-by-parts in the artificial diffusion term, we have:

$$\int_\Omega \frac{\partial H}{\partial t}\upsilon \, d\Omega = -\int_\Omega \operatorname{div}(H\mathbf{u})\,\upsilon + \nabla\upsilon \cdot (\mathcal{D}\nabla H)\, d\Omega + \int_\Omega (\dot{m}_s - \dot{m}_b)\,\upsilon \, d\Omega. \tag{3.27}$$

In a similar way, the Galerkin's approximation of Eq. 3.27 is:

$$\int_\Omega \frac{\partial H_N}{\partial t}\upsilon_N \, d\Omega = -\int_\Omega \operatorname{div}(H_N\mathbf{u})\,\upsilon_N + \nabla\upsilon_N \cdot (\mathcal{D}\nabla H_N)\, d\Omega + \int_\Omega (\dot{m}_s - \dot{m}_b)\,\upsilon_N \, d\Omega. \tag{3.28}$$

Writing the approximate solution H_N and the test function as a linear combination of the basis of the subspace $\mathcal{V}_H^N$ of $\mathcal{V}_H$, i.e.:

$$\upsilon_N(x,y) = \sum_{i=1}^{N} \beta_i \Phi_i(x,y), \quad H_N(x,y) = \sum_{j=1}^{N} \alpha_j \Phi_j(x,y), \tag{3.29}$$

we have:

$$\begin{aligned}\int_\Omega \frac{\partial}{\partial t}\left(\sum_{j=1}^{N}\alpha_j\Phi_j\right)\left(\sum_{i=1}^{N}\beta_i\Phi_i\right) d\Omega = &-\int_\Omega \operatorname{div}\left[\mathbf{u}\left(\sum_{j=1}^{N}\alpha_j\Phi_j\right)\right]\left(\sum_{i=1}^{N}\beta_i\Phi_i\right)\\ &+\nabla\left(\sum_{i=1}^{N}\beta_i\Phi_i\right)\cdot\left[\mathcal{D}\nabla\left(\sum_{j=1}^{N}\alpha_j\Phi_j\right)\right] d\Omega\\ &+\int_\Omega (\dot{m}_s - \dot{m}_b)\left(\sum_{i=1}^{N}\beta_i\Phi_i\right) d\Omega.\end{aligned} \tag{3.30}$$

The resulting system of equations[9] is:

$$\mathbf{M}\frac{\partial \boldsymbol{\alpha}}{\partial t} + \mathbf{K}\boldsymbol{\alpha} = \mathbf{F}, \tag{3.31}$$

where $\mathbf{M}$ is known as 'mass matrix', and $\mathbf{K}$ and $\mathbf{F}$ are the stiffness matrix and load vector, respectively. Each one of these entities is written as:

$$\begin{aligned} M_{ij} &= \int_\Omega \left(\sum_{i=1}^{N}\Phi_i\right)\left(\sum_{j=1}^{N}\Phi_j\right) d\Omega,\\ K_{ij} &= \int_\Omega \left(\sum_{i=1}^{N}\Phi_i\right)\operatorname{div}\left[\mathbf{u}\left(\sum_{j=1}^{N}\Phi_j\right)\right] + \nabla\left(\sum_{i=1}^{N}\Phi_i\right)\cdot\left[\mathcal{D}\nabla\left(\sum_{j=1}^{N}\Phi_j\right)\right] d\Omega,\\ F_i &= \int_\Omega (\dot{m}_s - \dot{m}_b)\left(\sum_{i=1}^{N}\Phi_i\right) d\Omega. \end{aligned} \tag{3.32}$$

[8] In ISSM, the artificial diffusion coefficient is calculated in each element using its characteristic size.

[9] There are different methods to solve the time derivative of H. ISSM employs the 'implicit method'.

3.4 Numerical scheme

Here, we briefly describe the numerical schemes implemented in ISSM to solve the systems of equations (Eqs. 3.22 and 3.31). In order to illustrate the numerical resolution, we change the notation of the systems such that the following system:

$$\mathbf{K}^v(\boldsymbol{\alpha}^v, \boldsymbol{\alpha}^H)\,\boldsymbol{\alpha}^v = \mathbf{F}^v(\boldsymbol{\alpha}^H), \tag{3.33}$$

represents the SSA non-linear system of equations and:

$$\mathbf{M}^H \frac{\partial \boldsymbol{\alpha}^H}{\partial t} + \mathbf{K}^H(\boldsymbol{\alpha}^v)\,\boldsymbol{\alpha}^H = \mathbf{F}^H, \tag{3.34}$$

represents the ice thickness system of equations[10].

The solution of Eq.3.33 for $\boldsymbol{\alpha}^v$ is carried out by the Picard's iterative scheme (also known as fixed-point iteration). The process is: given a geometry at time t and an initial guess for the velocity field, i.e., $\boldsymbol{\alpha}_t^H$ and $\boldsymbol{\alpha}_0^v$, respectively, solve the following sequence of linear systems:

$$\mathbf{K}^v(\boldsymbol{\alpha}_i^v, \boldsymbol{\alpha}_t^H)\,\boldsymbol{\alpha}_{i+1}^v = \mathbf{F}^v(\boldsymbol{\alpha}_t^H),\ i = 0,\ 1,\ 2,\ \ldots, \tag{3.35}$$

until a convergence criterion is reached (e.g., $\| \boldsymbol{\alpha}_{i+1}^v - \boldsymbol{\alpha}_i^v \| \leq \epsilon^v$, where ϵ^v is a given tolerance).

The temporal discretization of Eq. 3.34 is based on the implicit method:

$$\mathbf{M}^H \frac{\left(\boldsymbol{\alpha}_{t+1}^H - \boldsymbol{\alpha}_t^H\right)}{\Delta t} + \mathbf{K}^H\left(\boldsymbol{\alpha}_t^v\right)\boldsymbol{\alpha}_{t+1}^H = \mathbf{F}^H, \tag{3.36}$$

where the resulting linear system (for $\boldsymbol{\alpha}_{t+1}^H$) is:

$$\left[\mathbf{M}^H + \Delta t \mathbf{K}^H\left(\boldsymbol{\alpha}_t^v\right)\right]\boldsymbol{\alpha}_{t+1}^H = \Delta t \mathbf{F}^H + \mathbf{M}^H \boldsymbol{\alpha}_t^H. \tag{3.37}$$

Note that we keep, in Eq. 3.37, the previous velocity field, i.e., $\boldsymbol{\alpha}_t^v$. Considering the computation of both velocity field and ice thickness, the resulting coupled numerical scheme is 'semi-implicit' in time, as summarized by the following sequence:

$$\begin{cases} \text{Given } \boldsymbol{\alpha}_0^v \text{ and } \boldsymbol{\alpha}_1^H, \text{ find } \boldsymbol{\alpha}_t^v \text{ and } \boldsymbol{\alpha}_{t+1}^H: \\ \quad \mathbf{K}^v(\boldsymbol{\alpha}_i^v,\ \boldsymbol{\alpha}_t^H)\,\boldsymbol{\alpha}_{i+1}^v = \mathbf{F}^v(\boldsymbol{\alpha}_t^H) \\ \quad \text{for } i = 0,\ 1,\ 2,\ \ldots, \text{ until } \| \boldsymbol{\alpha}_{i+1}^v - \boldsymbol{\alpha}_i^v \| \leq \epsilon^v \\ \quad \boldsymbol{\alpha}_t^v = \boldsymbol{\alpha}_{i+1}^v \\ \quad \left[\mathbf{M}^H + \Delta t \mathbf{K}^H\left(\boldsymbol{\alpha}_t^v\right)\right]\boldsymbol{\alpha}_{t+1}^H = \Delta t \mathbf{F}^H + \mathbf{M}^H \boldsymbol{\alpha}_t^H \\ \text{for } t = 1,\ 2,\ 3,\ \ldots \end{cases} . \tag{3.38}$$

[10]Note that $\mathbf{K}^v$ depends on the velocity field and ice thickness (represented here as $\boldsymbol{\alpha}^v$ and $\boldsymbol{\alpha}^H$, respectively); $\mathbf{K}^H$ depends on the velocity field (see Eqs. 3.21 and 3.30).

3.5 Grounding line parameterization

The grounding line parameterization represents the numerical scheme of how the basal friction is applied on the elements present in the ice sheet/ice shelf transition. The implicit level set function ϕ_{gl} (Eq. 2.103) is used to define the grounding line position. In ISSM, there are four types of numerical discretization of basal friction within the elements: no sub-element parameterization (NSEP), sub-element parameterization 1 (SEP1), sub-element parameterization 2 (SEP2) and sub-element parameterization 3 (SEP3). Last one, SEP3, is actually not fully supported, then we focus on the first three. Figure 3.1 illustrates the grounding line position and sub-element parameterizations.

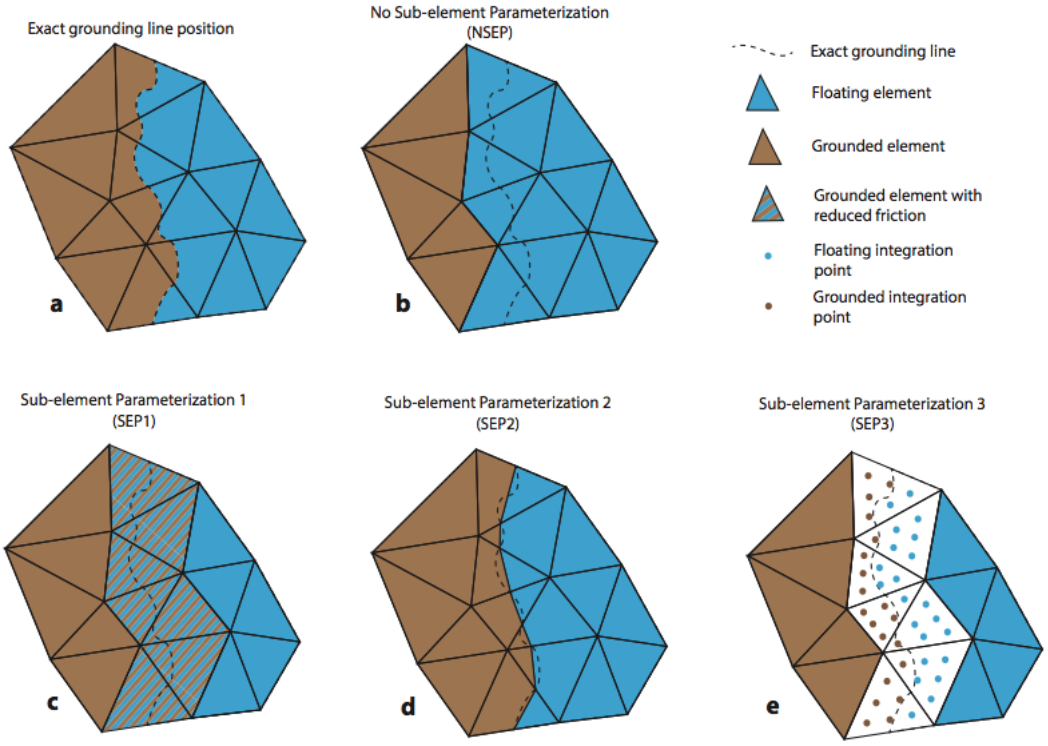

Figure 3.1: Different basal friction discretization within the elements. (**a**) is the exact grounding line position, (**b**) no sub-element parameterization, (**c**) sub-element parameterization 1, (**d**) sub-element parameterization 2, (**e**) sub-element parameterization 3. Figure from [138] ©The Authors, 2014, distributed under a Creative Commons Attribution license (http://creativecommons.org/licenses/by/3.0/)

In NSEP, no sub-element parameterization exists, in the sense that the grounding line is defined as the last grounded mesh vertex. Then, the basal friction is applied only on fully grounded elements. In SEP1, the basal friction coefficient C is reduced as $C_g = C\, A_g/A$, being C_g the new friction coefficient, A_g and A the grounded area and the total area of the element, respectively. In SEP2, the contribution of the basal friction is integrated[11] only on the grounded area of the element. More details of SEPs are found in [138].

[11] During the element stiffness matrix calculation.

3.6 ISSM architecture

The implementation of adaptive mesh refinement in ISSM is strongly based on its architecture. We describe here the main ISSM features necessary to understand the adaptive mesh strategy. We refer to Larour *et al*. [88] for a more detailed description of ISSM[12].

ISSM is an open source finite-element-based ice sheet simulator developed in collaboration between the Jet Propulsion Laboratory and University of California at Irvine. The main purpose of this collaboration is to tackle the challenge of modeling the evolution of Greenland and Antarctica ice sheets. ISSM is funded by NASA Cryosphere, IceBridge Research and MAP (Modeling Analysis and Prediction) programs, JPL R&TD (Research, Technology and Development), and National Science Foundation (NSF). The computational core of ISSM is written in C/C++, and its interface[13] is written in MATLAB.

Several stress balance approximations are implemented in ISSM, including higher-order models (e.g., Blatter & Pattyn [18, 115], Full Stokes). The current adaptive mesh capability is supported for the 2-D vertically integrated Shallow-Shelf or Shelfy-Stream Approximation, SSA [94, 100]. The SSA formulation is employed for both grounded and floating ice, then membrane stress terms [136] are included but all vertical shearing is neglected [139]. Here, the mesh used for the SSA formulation is unstructured and relies on a Delaunay triangulation. The initial mesh is generated by Bamg [66], but the mesh adaptation can be performed by Bamg or NeoPZ [34] (one or the other mesh generator is used according to the user's choice).

In ISSM, the solution of one partial differential equation (or a single time step in a time-dependent partial differential equation) is called 'analysis', e.g., stress balance analysis, mass transport analysis, damage evolution analysis, etc. One or several analyzes can be carried out in a given numerical simulation; then, the solution of one or several analyzes is called 'core', e.g., stress balance core, transient core, hydrology core, etc. The ISSM core used in this work is the transient core, which involves several analyzes (e.g., stress balance, mass transport, grounding line migration, ice front migration, etc). These analyzes are executed or not according to the user definition.

The ISSM data structure is organized through the 'FemModel' class, which represents the finite element model (FEM) of the physical problem. The class FemModel contains the following FEM data structures:

1. **Analysis_Type_List**: a list of analyzes to be carried out;
2. **Elements**: a list of the FEM elements (does not depend on the analysis type);
3. **Vertices**: a list of the geometric vertices (does not depend on the analysis type);
4. **Nodes**: a list of the degrees of freedom (depends on the analysis type);
5. **Constraints**: a list of the constraints (depends on the analysis type);
6. **Materials**: a list of materials, for each element (does not depend on the analysis type);
7. **Parameters**: a list of all model parameters (does not depend on the analysis type).

[12] Additional information is also found in the ISSM website: https://issm.jpl.nasa.gov/, last access: Feb 2 2019.
[13] Pre and post processes.

Analysis_Type_List is a vector filled up with the analyzes according to the core chosen to be carried out. Each analysis is responsible to compute the element stiffness matrix as well as the element vector load. General algorithms of solution sequences lead the computation and assembly of the stiffness matrix and load vector, as well as the numerical solution of the resulting (non)linear system.

The **Elements** vector represents both the geometric and computational elements. Here, computational means that the elements deal with the description of the fields in the corresponding approximation space; e.g., let's say that the ice thickness H is described by $\mathscr{P}_1$ Lagrange polynomials, then a given element computes the $\mathscr{P}_1$ basis functions and their spatial derivatives to generate $H(x,\ y)$ and $\nabla H(x,\ y)$, respectively, over the element domain. The **Vertices** vector keeps the spatial coordinates of the geometric vertices. **Nodes** is a matrix that keeps, for each analysis to be carried out, the corresponding degrees of freedom. The degrees of freedom that are constrained by Dirichlet boundary conditions are also kept in the **Nodes** structure. **Constraints** is also a matrix that keeps, for each analysis, the values of the boundary conditions, as well as the indexes of the corresponding nodes. The **Materials** vector has the same size of the **Elements** vector, and is responsible for computing material properties like ice viscosity, equivalent ice viscosity when the ice is damaged or enhanced, etc. **Parameters** is a vector structure that keeps all model setups, like domain dimension, physical constants, convergence criterion, etc.

In ISSM, all the information and data necessary to define a FEM model are called 'inputs'. Basically, there are five types of FEM model inputs:

1. Material type and state (ice or lithosphere, is damaged or not, etc);
2. Material parameters varying in space, which can be post-processed or not (ice viscosity, damage, Glen's flow law exponent, flow law parameter, etc);
3. Fields that vary in space (ice velocity, ice thickness, ice surface, bedrock elevation, basal friction coefficient, etc);
4. Physical constants, numerical parameters and model configuration that are constants (ice density, gravitational acceleration, convergence criterion, maximum number of iterations, domain dimension, grounding line migration type, etc).
5. Specified field values that represent the (Dirichlet) boundary conditions, which vary in space (specified ice velocity, specified ice thickness, etc).

These model inputs are kept in the following FemModel data structures:

1. Inputs (1) are kept in the **Materials** vector, i.e., FemModel->Materials;
2. Inputs (2) and (3) are kept within the FEM elements through the data structure called **Inputs**, i.e., FemModel->Elements[i]->Inputs[14];
3. Inputs (4) are kept in the **Parameters** vector, i.e., FemModel->Parameters;
4. Inputs (5) are kept in the **Constraints** matrix, i.e., FemModel->Constraints.

[14]Here, 'i' is an index in the vector FemModel->Elements.

ISSM is designed to run in parallel in a distributed memory scheme based on the 'Message Passing Interface', MPI. When a model is launched, the entire mesh[15] is spatially partitioned over processing units (CPUs), and the FEM model data structures are built in each partition. In this scheme, only one FemModel is built per each partition (CPU). Figure 3.2 shows an example of a mesh being partitioned in three partitions[16]. The mesh partitioner used in ISSM (METIS [82]) generates partitions with similar number of elements. This procedure reduces the imbalances during the solver phase (e.g., stiffness matrix assembly).

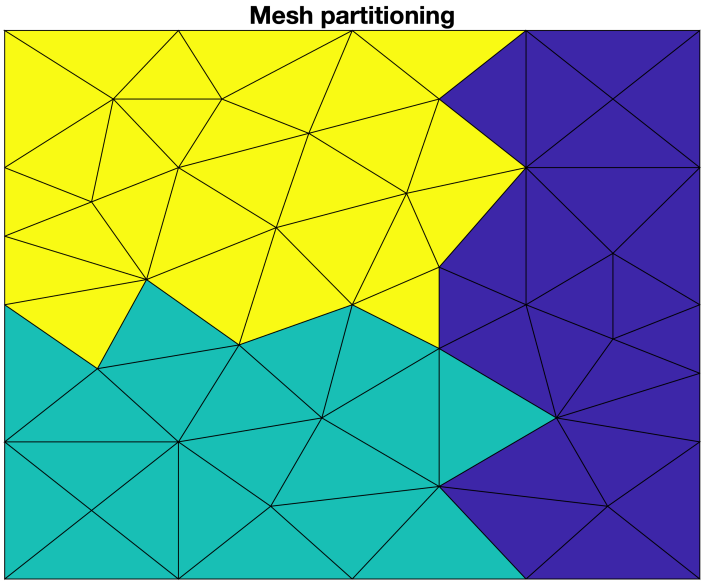

Figure 3.2: Example of a mesh partitioning: each color represents a partition (CPU). The mesh partitioner in ISSM keeps the number of elements similar between the partitions.

MPI communications between the partitions (CPUs) are performed to assemble the global stiffness matrix and load vector, as well as during the solution update in the elements once the system of equations is solved. The advantage of MPI is its ability to handle larger models (i.e., continental-scale simulations) in many cores and nodes on a cluster. Its disadvantage is the cost in the communications between the partitions.

The suite of solvers applied in ISSM is provided by the Portable, Extensive Toolkit for Scientific Computation package [11, 10, PETSc], which is also based on MPI. The non-linear SSA equations are solved using the Picard scheme and the Multifrontal Massively Parallel sparse direct Solver [4, 5, MUMPS].

[15] Which describes the whole physical domain.

[16] In this case, three CPUs are used; each CPU is responsible to build the FEM data corresponding to its own partition.

3.7 Adaptive mesh refinement

The quality of the finite element approximation of a boundary-value problem depends on the choice of the basis functions. In its turn, the construction of the set of the basis functions depends on the mesh describing the domain. One can often confronts with the situation of deciding on a mesh, analyzing the quality of the calculated solution, and perhaps iteratively adjusting and enriching the mesh. Since the solution and its derivatives may change considerably over the domain and/or over the time (in transient problems), enriching the mesh locally is a suitable way to guarantee numerical accuracy and computational efficiency. This technique is often called 'adaptive mesh refinement'.

The first works on adaptive refinement in finite element calculations were introduced by Babuška and Rheinboldt in the late 1970's [8, 9]. Their technique was based on a posteriori error estimators calculated on each finite element such that the adaptive meshing was design to minimize the error over the mesh. The search of effective adaptive methods took place during the early 1980's, when many of ad hoc errors estimators were developed. Most of these errors estimators were based on a priori estimation, which provided sufficient indicators for driving the adaptive procedures, but that sometimes failed when complex features of the solution appear (e.g., boundary layer, shock-boundary layer interactions) [1]. A simple but relatively effective a posteriori error estimator appeared with the work of Zienkiewicz and Zhu in 1987 [161]. The core of their estimator is the recovering process of the gradient of solutions such that recovered gradients are compared to the original FEM gradients to assess an estimation of the error. This technique is classified as a 'recovery based method', and the accuracy and robustness of the estimator depends on the specifics steps used to construct the recovered gradient [2, p. 66]. The extension of this technique was carried out by Zienkiewicz and Zhu in 1992 [162, 163] to the named 'superconvergent patch recovery' method, which main process is selecting mesh points that exhibits superconvergent recovery solutions. By superconvergent we mean that the solution converges faster in comparison to a priori estimation when the adaptive refinement is guided by this technique. In the following decades, many studies dedicated to the development of a posteriori error technique for both h and p version of the finite element method, and to the studies of robustness of such estimators in different applications [2, p. 4]. A complete review of the progress of adaptive mesh refinement and a posteriori error estimator is found in the book of Ainsworth and Oden [2] and in the references within it.

Basically, the adaptive mesh refinement technique can be performed with three different methods [112, 160, p. 402]: remeshing, r-adaptivity and h-adaptivity methods. The remeshing method represents a complete mesh regeneration where both refinement and coarsening elements are executed according to a posteriori analysis of the solution. The r-adaptivity method, also known as moving mesh method, moves progressively a fixed number of vertices in a given direction or region [6, p. 533]; in this method, the total number of vertices are kept constant. The h-adaptivity method splits edges and/or elements, inserting new vertices and elements into the mesh where high resolution is required (where high errors are observed), e.g., [15, 33]; the coarsening is also executed in the h-adaptivity method. The performance of each of these methods depends on the problem for which they are applied. Here, we are interested in the remeshing and h-adaptivity techniques.

There are a number of works analyzing the adaptive mesh refinement method applied to ice

sheet dynamics. Vieli and Payne, in 2005 [153] showed that models applying a moving mesh to track the grounding line movement perform better than fixed mesh models. Since the position of the grounding line is explicitly defined in moving meshes, Vieli and Payne noticed for this method a weak mesh resolution dependency in comparison to the fixed mesh method, for which the grounding line position falls between mesh vertices. Goldberg and colleagues, in 2009 [57], obtained accurate solutions with fewer computational effort solving the time-dependent shelfy-stream equations with the two of the mesh adaptation techniques mentioned above, moving mesh and *h*-adaptivity methods. Using a one-dimensional shelfy-stream model based on finite difference scheme, Gladstone and colleagues, in 2010 [54], demonstrated that adaptive mesh refinement and sub-element parameterization for grounding line position could produce robust predictions of grounding line migration. In a 1D marine ice sheet model intercomparison project (MISMIP), Pattyn and participants, in 2012 [119], found that moving mesh technique tends to be the most accurate and *h*-adaptivity method can further improve grounding line position accuracy compared to models based on a fixed mesh. In 2013, through a 3D marine ice sheet model intercomparison project (MISMIP3d), Pattyn and participants [118] confirmed the grounding line dynamics dependency on mesh resolutions. Cornford and co-authors, in 2013 [27], implemented a block-structured adaptive mesh refinement in the Berkeley Ice Sheet Initiative for Climate Extremes (BISICLES), a 2.5-D ice sheet model based on the finite volume method. They demonstrated that simulations with mesh adaptivity are computationally cheaper and more efficient, even as the grounding line moves over significant distances. Jouvet and Gräser, also in 2013 [81], combined the shallow ice approximation and the shallow-shelf approximation in a mesh adaptivity numerical scheme involving a truncated Newton multigrid and finite volume method. Through MISMIP3d experiments [118], they highlighted the relevance and efficiency of adaptive mesh refinement in terms of computational cost when high resolution ($\sim$100 m) is necessary to reproduce grounding line reversibility. Recently (2017), Gillet-Chaulet and colleagues [53] implemented an anisotropic mesh adaptation in the finite element ice flow model, Elmer/Ice [51]. Based on the MISMIP+ experiment [7], they showed that combining various variables (ice thickness, basal drag, velocity, etc.) in an estimator allowed to reduce the number of mesh vertices by more than 1 order of magnitude compared to uniformly refined meshes, for the same level of numerical accuracy.

3.7.1 NeoPZ

NeoPZ [34] is a finite element library dedicated to highly adaptive techniques [22]. The scheme used by NeoPZ is the *h*-adaptivity method. In NeoPZ's data structure, each element is refined into 4 topologically similar elements, whose resolutions are half of the refined element. Figure 3.3(a) presents a triangle (vertices 1-2-3) refined in four triangles (A, B, C, and D).

To avoid hanging vertices/nodes [22] (red vertices in Figure 3.3(a)), some elements are divided in specific ways such that any two elements in the mesh may have a vertex or an entire edge in common, or no vertices in common [147, p. 81]. The degrees of freedom associated with the hanging vertices should be handled to keep a continuous space of test functions. This can be done by constraining the (hanging) degrees of freedom on the neighbor nodes (red lines in Figure 3.3(a)), a procedure that changes the local stiffness matrix of the elements and, consequently, the global stiffness matrix. An alternative that does not change the (non)linear

system is the refinement of the neighbor elements in specific ways that the hanging nodes are naturally constrained. Figure 3.3(b) shows the refinement of the neighbor elements (gray elements are created) in specific ways such that the hanging nodes are naturally constrained. The approach shown in Figure 3.3(b) is adopted in this work. In this sense, all meshes refined by NeoPZ are nested, i.e., vertices and connectivities from the coarse mesh are kept fixed during all simulation time. Figure 3.4 presents an example of an adaptive mesh using NeoPZ. By generating nested meshes does not introduce any numerical error induced by the adaptive mesh refinement during the interpolation process (see Section 3.8).

The adaptive mesh refinement with NeoPZ is given by specifying the level of refinement, i.e., how often elements are refined. Therefore, the 'mesh transition zone', which links regions of different resolutions, is generated stepwise through resolutions dictated by levels of refinement.

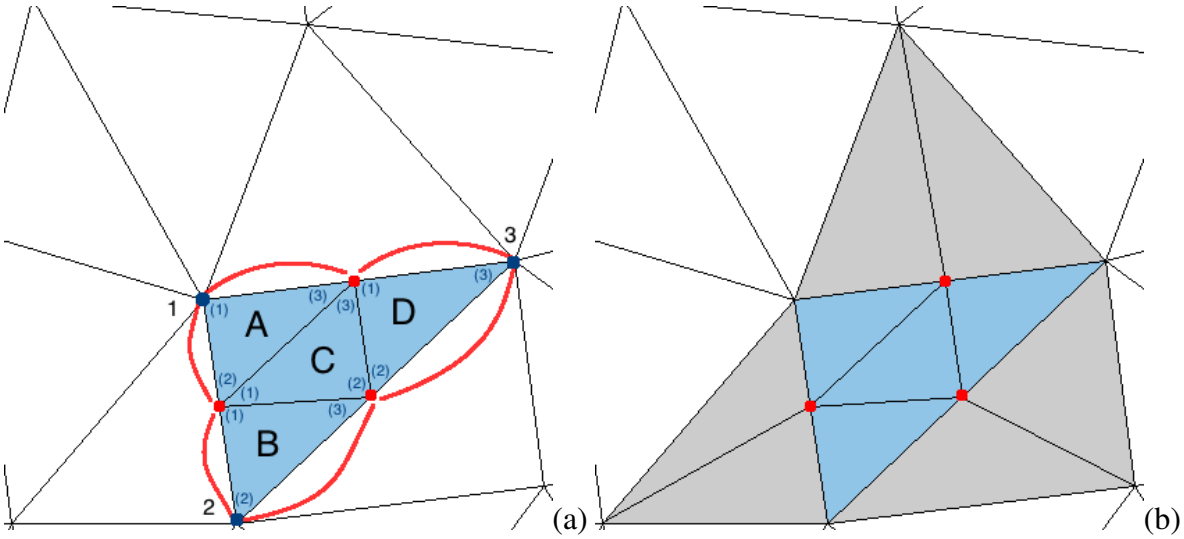

Figure 3.3: (a) Refinement of a triangular element (blue elements are created). Using uniform refinement pattern, hanging nodes are generated (red dots). These hanging nodes can be handled by constraining their degrees of freedom on their neighbor nodes (red lines). (b) Specific refinement can be used in the neighbor elements (gray elements are created) to constraint naturally the hanging nodes.

3.7.2 Bamg

Bamg [66] is a bidimensional mesh generator based on Delaunay-like method [65]. The scheme applied with Bamg is the remeshing method. This mesh generator is embedded in ISSM for static anisotropic mesh adaptation [102]. Here, we extend Bamg capabilities for dynamic adaptive mesh refinement. The refinement in Bamg is carried out by specifying the desired resolution on the vertices. To reach the desired resolution, Bamg's algorithm splits triangle edges and inserts new vertices in the mesh [66]. The algorithm keeps new vertices and connectivities unchanged as much as possible compared to the previous mesh [65]. This procedure reduces the numerical errors introduced by the AMR when the solutions are interpolated into the new mesh (see Section 3.8). Regions of different resolutions are linked by a mesh transition zone, where the element sizes are changed gradually. The spatial extent of this mesh transition zone is also specified by the user in the Bamg's algorithm. An example of adaptive mesh using Bamg is shown in Figure 3.5.

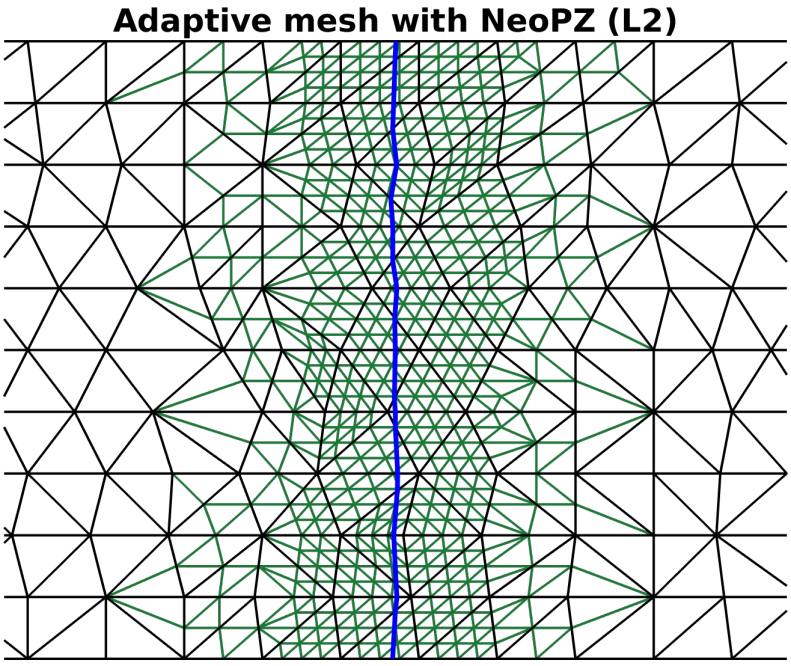

Figure 3.4: Example of adaptive mesh generated by NeoPZ. Blue line: grounding line position. Black lines: coarse mesh. Green lines: adaptive mesh with level of refinement equal to 2 (L2). NeoPZ generates nested meshes; vertices and connectivities of the coarse mesh are kept unchanged.

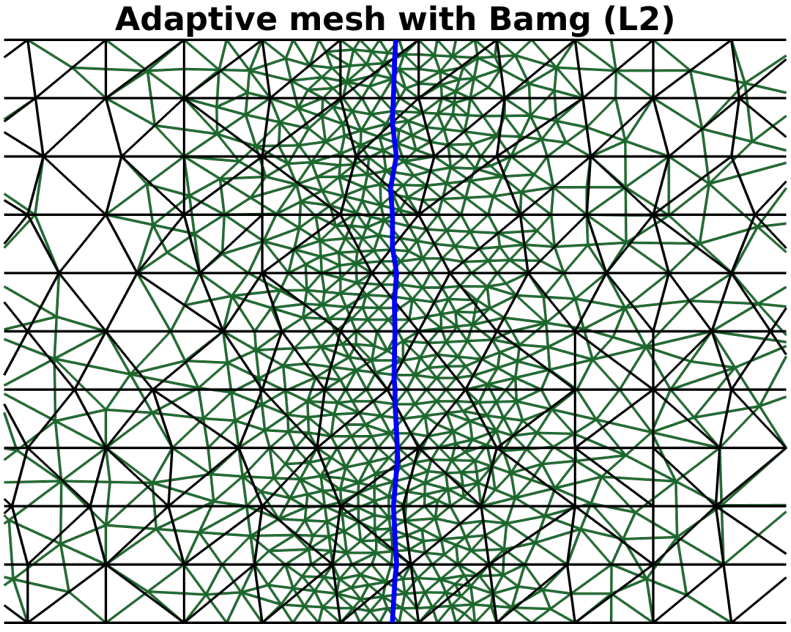

Figure 3.5: Example of adaptive mesh generated by Bamg. Blue line: grounding line position. Black lines: coarse mesh. Green lines: adaptive mesh with level of refinement equal to 2 (L2). Bamg keeps vertices and connectivities unchanged as possible compared to the coarse mesh.

3.8 Adaptive mesh refinement implementation in ISSM

Since the parallel scheme in ISSM is based on MPI and a given numerical simulation (transient core) is performed by several analyzes, we choose an implementation strategy with no impacts on the ISSM architecture and with minimized MPI communications to avoid overheads and latencies when big models are run.

We adopt an explicit approach in terms of mesh adaptivity in time-dependent simulations, where a new adapted mesh is built for a given solution, in a given time step. Although a predictor-corrector-like algorithm[17] for the mesh adaptation may be more consistent from a mathematical point of view, the explicit approach used here is suitable to the physical problems being investigated. Furthermore, our experience shows that the solutions don't change expressively between any two consecutive time steps, which makes unnecessary any loop iteration in the mesh adaptation, in each time step, to find the most suitable mesh. Thus, our scheme performs only one mesh adaptation in each time step. The solution sequence for transient simulations in ISSM with adaptive mesh refinement is summarized in Figure 3.6. Note that, in Figure 3.6, the adaptive mesh refinement is the last step to be executed for each time step.

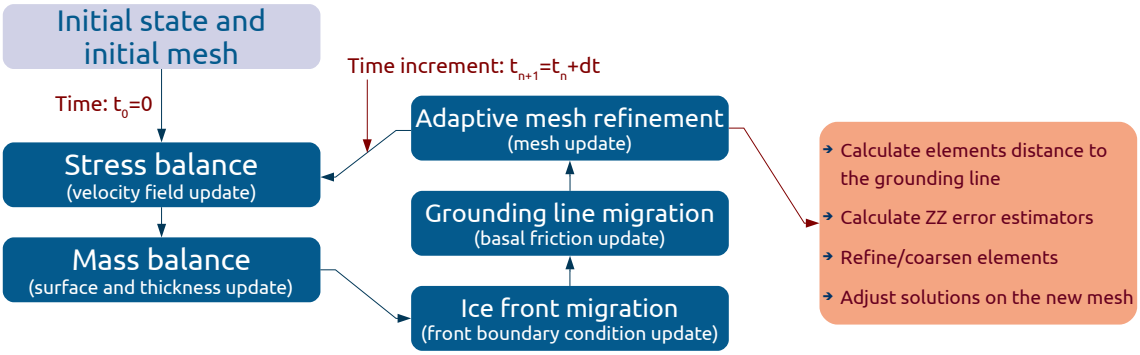

Figure 3.6: Solution sequence of marine ice sheet simulation with adaptive mesh refinement.

In terms of data structure, our strategy is to keep the entire mesh during all simulation time. We implement a new class in ISSM called 'AdaptiveMeshRefinement', which keeps Bamg or NeoPZ data structure of the entire mesh and performs the mesh adaptation. This data is kept within the FemModel class, i.e., 'FemModel->AdaptiveMeshRefinement'. This class also keeps the refinement criteria used in a given numerical simulation. Some works (e.g., [70]) adopt a different strategy in FEM codes based on MPI: each partition (CPU) executes the mesh adaption in its own mesh partition. In our implementation, only one partition (whose CPU rank is no. 0) keeps the Bamg or NeoPZ entire mesh and is responsible for executing the adaptive mesh refinement process. Details of the adaptive mesh refinement processes are itemized in Algorithm 1. In Algorithm 1, all processes involved in performing the mesh adaptation in ISSM are executed in step 'e', the remeshing core. Step 'e.1' executes the mesh adaptation (refinement or coarsening) and the other steps ('e.2' to 'e.5') prepare the adapted mesh, data structures and solutions for the next simulation time step. Both Bamg and NeoPZ perform the mesh adaptivity (step 'e.1', Algorithm 1) in serial, considering the entire mesh.

[17] See, for example, the scheme used in [33]; in each time step, there is a loop of mesh adaptation.

Algorithm 1 Transient simulation with adaptive mesh refinement

1. set initial solution state and initial mesh[18]
2. while $t_n \leq t_{max}$, do:
    a. call stress balance core (diagnostic)
    b. call thickness balance core (prognostic)
    c. call ice front migration core (level set adjustment)
    d. call grounding line migration core (hydrostatic adjustment)
    e. call remesh core (AMR)
        e.1. call AMR core (refine/coarsen mesh, Bamg or NeoPZ, serial in CPU #0)
        e.2. call mesh partitioning (over all CPUs, serial)
        e.3. build new data structures (all CPUs, parallel)
        e.4. interpolate solutions (all CPUs, parallel)
        e.5. call geometry adjustment core (all CPUs, parallel)
    f. time increment $t_{n+1} = t_n + dt$
3. post processing

Our implementation keeps the number of partitions constant during the entire simulation time. The number and distribution of elements into the partitions vary every time the adaptive mesh refinement is executed, since the mesh partitioning process (step 'e.2', Algorithm 1) generates partitions with a similar number of elements. This process reduces memory imbalance among the CPUs and overheads during the solver phase [88]. Figure 3.7 shows the evolution of the grounding line, and consequently the evolution of the mesh, for four consecutive time steps. We observe in Figure 3.7 how the distribution of the elements changes over the partitions every time the remesh core is called.

Each time remeshing core is performed, the solutions and all data fields that vary in space are interpolated from the old mesh onto the new mesh. This process is executed by reducing all fields in CPU no. 0, and then broadcasting them to the other CPUs as soon as the partitioning process and the building of new data structures are executed. The interpolation process is executed in parallel, where each CPU interpolates the solutions and fields just on its own mesh partition (step 'e.4', Algorithm 1). This all-to-one reduction and one-to-all broadcasting strategy is adopted because the distribution of elements over the partitions is not constant during the simulation time. Although this reduction/broadcasting process may be a bottleneck for large models, our strategy takes the advantage of using a pre-existent ISSM interpolation algorithm where all fields

[18]The setup of initial solutions into the initial mesh is important to reduce numerical artifacts during the first time steps. Therefore, the initial mesh should be defined using AMR with the same level of refinement chosen in Algorithm 1 (e.g., see [27, 89]).

are interpolated on given point using a vectorized operation, saving computational time during this step. Just to illustrate the size of MPI data transmissions, we show here a simple calculation. A mesh with 100,000 elements has about 50,000 vertices. Then, we have: 50,000 x 8 bytes = 0.4 Mb per interpolated field. This size is relatively small considering the transmission rate of current InfiniBand[19] (>10 Gb/s).

The construction of FEM model data structures and the adjustment of solutions (steps 'e.3' and 'e.5', respectively, Algorithm 1) are executed in parallel, i.e., each partition takes care of its own data structure. The computation of the refinement criteria (see Section 3.9) is also carried out in parallel.

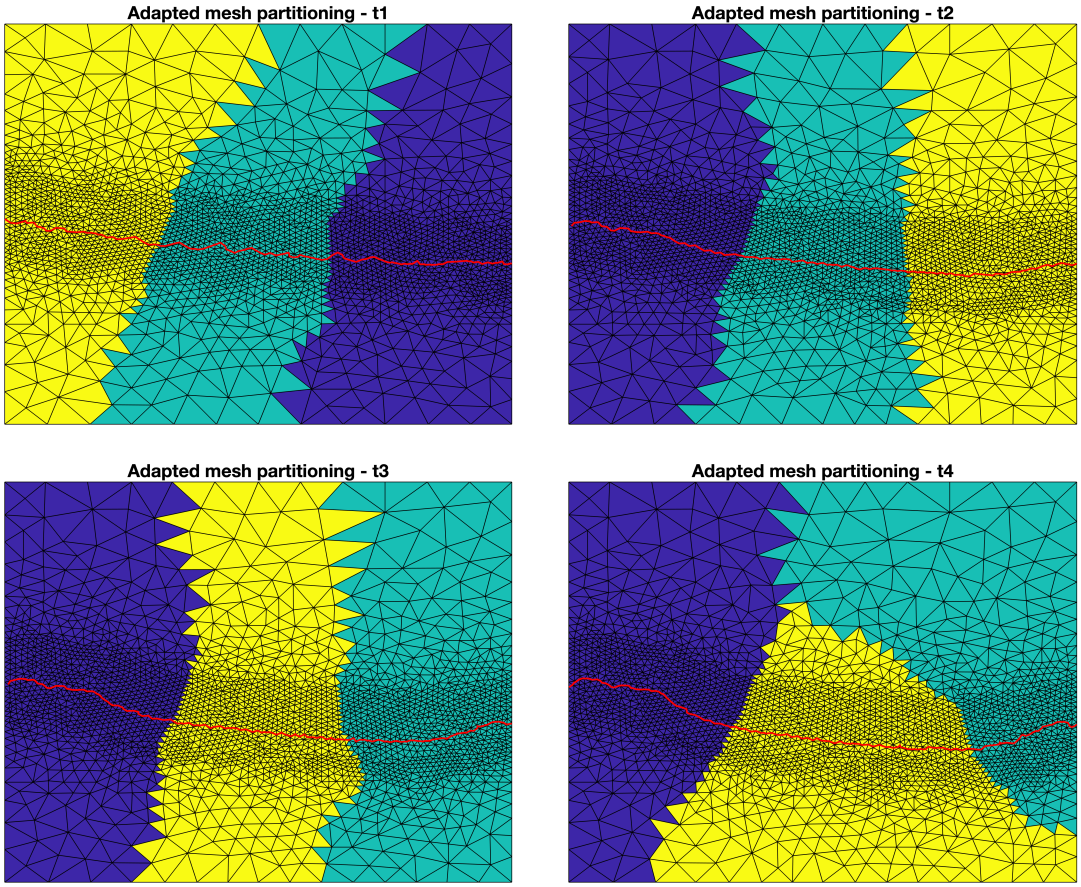

Figure 3.7: Example of a mesh partitioning during transient simulations (four consecutive time steps) with adaptive mesh refinement: each color represents a partition. Red line: grounding line position. Black line: adapted mesh.

All MPI communications in the remesh core (step 'e', Algorithm 1) are minimized to avoid overheads when large models are run. In order to minimize MPI calls, we perform a single communication of a large array that includes all data structures. In the interpolation process, for example, all solutions and fields are compacted by CPU no. 0 in a single vector structure in such a way that only one MPI broadcast is called. This approach is based on the fact that, in general, it is more efficient to perform few large MPI messages instead of carrying out many smaller ones [125, p.327].

[19]InfiniBand is a common networking device used for data transmission between several nodes in high-performance clusters.

3.9 Refinement criteria

The performance of any adaptive mesh approach depends on the refinement criterion [33]. We implement the three following criteria in ISSM:

(a) Element distance to the grounding line, R_{gl};

(b) Error estimator for deviatoric stress tensor, $\boldsymbol{\tau}$, and ice thickness, H;

(c) Different combinations of (a) and (b).

Criterion (a) is based on a heuristic approach commonly applied in the literature [57, 62, 27], where elements near the grounding line are refined until a desired resolution is reached. For example, Schoof 2007 [136] applied a high grid resolution at the transition zone, the region around the grounding line where mechanical sheet-shelf coupling must be accurately resolved (see Section 2.12). In fact, he observed discrepancies in the grounding line dynamics using an adapted high-resolution grid and an equally spaced coarse grid. In criterion (a), both the width around the grounding line in which the elements are refined and the desired resolution are parameters imposed by the user.

The second criterion, (b), automates the decision about the region or elements that should be refined based on their error estimates. We implement the a posteriori error estimator conceived by Zienkiewicz and Zhu in 1987 (ZZ, [161]). The ZZ error estimator was proposed for a linear elasticity problems, which involves elliptic equations. We implement the ZZ error estimator for the deviatoric stress tensor ($\boldsymbol{\tau}$) and we also extend the estimator for the ice thickness (H). Applying the ZZ error estimator to the deviatoric stress tensor is a natural extension, since the non-linear SSA equations are also elliptic. In fact, criterion (b) is based on the fact that high changes in the gradients in the velocity field (therefore, in the deviatoric stress tensor, $\boldsymbol{\tau}$) and ice thickness, H, are expected to be present near the grounding line, i.e., in the transition zone. Figure 3.8 shows an example of the velocity field (x-direction, steady state) around the grounding line for the MISMIP+ setup (see details in Section 4.3). The velocity field in Figure 3.8 was calculated using adaptive mesh refinement.

The ZZ error estimator calculated for the ice thickness highlights the regions of sharp bedrock gradient, and could be used to improve the resolution of the bedrock geometry. In fact, the bedrock defines the 'vertical geometry' of the mathematical problem, which impacts the solutions (velocity field and ice thickness). Therefore, the ZZ estimator for the ice thickness could be an indicator of areas where the bedrock geometry should be improved in terms of resolution, mainly in transient simulations where the grounded area changes with time. We suspect that the ZZ for the ice thickness could be also useful if applied together with the other one (ZZ for the deviatoric stress). The performance of this combination in real ice sheets and glaciers should be assessed in the future, since in real bedrock elevation there are complex features and noises.

Criterion (c) extends and merges the features of the other two previous refinement criteria. This criterion is based on the following: we know a priori that applying high resolution around the grounding line would reduce the error caused by the basal friction discretization within the elements (see Section 3.5 and [138]). On the other hand, applying only an error estimator does

not guarantee that the all elements around the grounding line are refined as properly desired[20]. We suspect there are at least three sources of numerical errors (which may be related to each other) in ice sheet simulations:

(1) Basal friction discretization within the elements around the grounding line;

(2) High gradient changes in the velocity field near the grounding line;

(3) Bedrock geometry description.

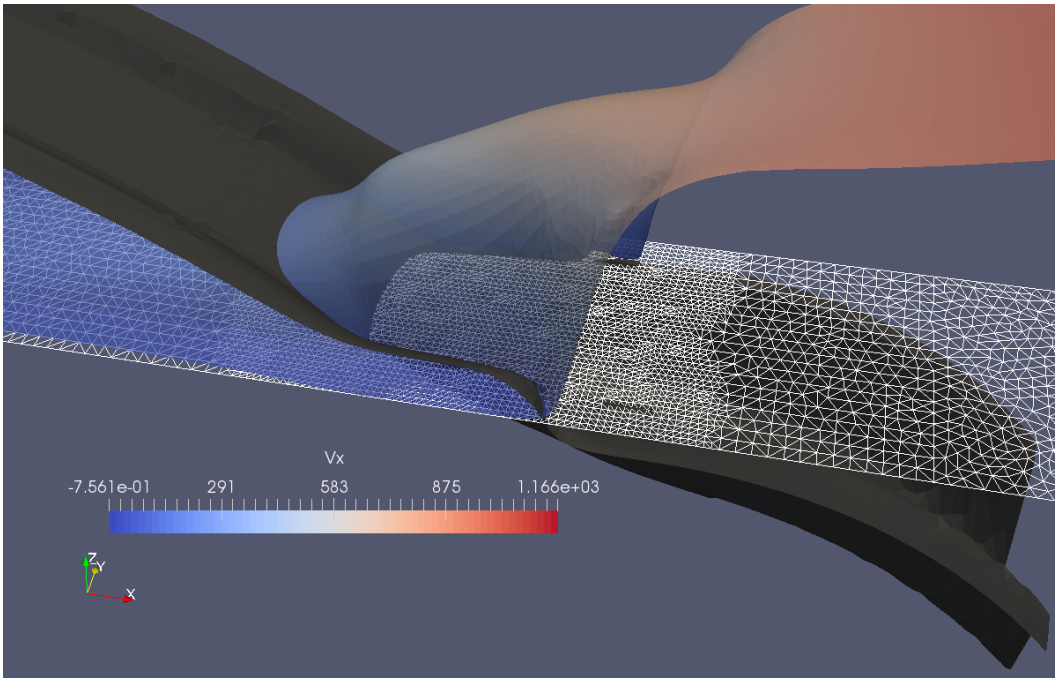

Figure 3.8: Example of the velocity field around the grounding line for the steady state solution of the MISMIP+ setup (see Section 4.3). The color bar represents the velocity field in the x-direction, and the brown surface represents the level set function ϕ_{gl} that determines the grounding line position (see Section 2.12).

Component (1) is a numerical model-dependent error. Using the sub-element parameterizations SEP1 and SEP2, the numerical convergence is higher than using NSEP (see [138]; also see our results in Section 4.2). Nevertheless, high resolution at the grounding line is yet necessary to reduce this error component. Then, criterion (a) should reduce this error. Component (2) is a physical problem-dependent error. We know that around the grounding line, in the transition zone, and in shear stream margins ([133, 64]), the deviatoric stress tensor dominates the stress balance (e.g., [136]). The width of these zones where the velocity field changes significantly (where the deviatoric stress tensor dominates) depends on the geometry of the physical problem, e.g., bedrock topography, ice thickness, ice sheet length, basal conditions, etc. Refining the elements in these zones would reduce the numerical error in the deviatoric stress tensor.

[20]In fact, we noted this for the MISMIP+ experiments. See Section 4.3.

Therefore, criterion (b) should reduce this component in an automated way. Component (3) is the error due to the discretization of the physical geometry. Currently, our adaptive mesh refinement doesn't increase the resolution of real bedrock topographies accordingly the mesh refinement process. This means that, for real ice sheets, the bed elevation remains the same as the coarse bed elevation (i.e., defined by the coarse mesh) during all simulation time. The only exception is for the MISMIP+ experiments: we hard coded the MISMIP+ bed elevation directly in ISSM such that the resolution of the bed is increased/decreased during the mesh refinement process. Keeping the bed resolution constant, and let's say, in a coarse representation, complex features and noises of the bed topography are smoothened, which tends to reduce the numerical error. But not necessarily this is always true, because fundamental geometric aspects could be 'hidden' in a coarse representation. As an example, let's take a given 2D problem in the unit circle for which we would like to solve numerically. The representation of the boundary (the circle) will be always finite and it will depend on the mesh resolution. Figure 3.9 shows a representation of our unit circle using different mesh resolutions. It is clear, through Figure 3.9, that the real boundary geometry is better approximated with the increase of mesh resolution. But if the circle description is kept in the coarser representation (the coarser mesh in Figure 3.9), even with mesh refinement, the boundary is not well approximated and this error component continues to pollute the solution. Figure 3.10 shows this case, where we apply a mesh refinement into the coarser unit circle geometry. Therefore, not necessarily applying criterion (a) or (b) (or combination of both) in an adaptive mesh scheme should improve the bedrock resolution as the setup of an initial uniformly refined mesh does (considering that the bedrock resolution is increased/decreased with the mesh resolution in this case). In fact, increasing/decreasing the bedrock geometry resolution during the mesh adaptation makes the problem different from a mathematical point of view. The impact of the bedrock description on real ice sheet numerical modeling is addressed in some works (e.g., [38, 106]). Although numerical models could be more sensitive to bed resolutions on coastal areas [38], small topographic features can cause significant differences in dynamic response in decadal-scale simulations [106]. We are not addressing this analysis in this work, Despite component (3), we suspect that criterion (c) should work properly to reduce the others components, (1) and (2).

We define the adaptive mesh refinement criterion used based on binary flags θ (= 0 or 1):

$$\begin{cases} \theta_{gl} = 1: & \text{use element distance to the GL} \\ \theta_{\tau} = 1: & \text{use ZZ error estimator for } \tau \\ \theta_{H} = 1: & \text{use ZZ error estimator for } H \end{cases} . \tag{3.39}$$

We propose Algorithm 2, inspired by [33], to execute the refinement and coarsening processes under different criteria (AMR core, step 'e.1' in Algorithm 1). The first 3 steps in Algorithm 2 compute the criterion according to the binary flags, θ, defined above. These steps are performed in parallel. Step '4' verifies, for each element in the mesh, if it should be refined: its distance to the grounding line and its ZZ error estimators are compared with prescribed limits (thresholds). The element is refined if at least one of the thresholds is exceeded, so long as its level of refinement is less than the maximum level chosen by the user. This logical operation is performed by the operator 'or' in the statement 'if' in step '4'. Once an element is refined, it is identified as a group. Step '5' verifies for each group if it should be coarsened. To be coarsened, a group

should meet all thresholds; the logical operator used in this case is 'and' (statement 'if' in step '5'). Algorithm 2 has two sets of thresholds (shown with max), for elements and for groups of elements. For the algorithm to work properly, these sets of thresholds should be defined such that (following [33]): $\chi_g^{max} < \chi_e^{max}$, where χ represents the threshold, g refers to group of elements, and e refers to elements.

The generic form of the ZZ [161] error estimator $\epsilon(e)$ for a given element e is:

$$\epsilon(e) = \left[\int_{\Omega_e} \left(\nabla u_N^* - \nabla u_N \right)^2 d\Omega_e \right]^{1/2}, \tag{3.40}$$

where Ω_e is the domain of the element e, ∇u_N is the gradient of the finite element solution u_N and ∇u_N^* is the smoothed recovery gradient, calculated on the element e as:

$$\nabla u_N^* = \sum_{i=1}^{s} \nabla u_{N,i}^* \Phi_i \,, \tag{3.41}$$

and

$$\nabla u_{N,i}^* = \frac{1}{W_i} \sum_{j=1}^{k} w_j \nabla u_{N,j} \,, \tag{3.42}$$

where Φ_i is the ith $\mathscr{P}_1$ Lagrange shape function on element e, s is the number of shape functions of the element e (for triangular elements, $s = 3$), j is the jth element connected to the vertex i, k is the number of elements connected to vertex i, w_j is the weight relative to the element j and W_i is the sum of all weights for the vertex i. Here, the weights w are defined as the geometric area of the triangular elements. Figure 3.11 presents the gradient (derivative) of the analytic solution of problem A.1 (see Appendix A), the gradient of the solution from the finite element method and the recovery gradient, based on expressions 3.41 and 3.42. The ZZ error estimator uses the recovery gradient as an estimate of the 'true' unknown gradient, and compares it with the gradient obtained from the finite element solution; the higher is the difference between the FEM gradient and the recovery gradient, the higher is the estimator. In fact, we can note through Figure 3.11 that the recovery gradient is a 'good' approximation of the analytic gradient solution, giving a reasonable estimation of the 'true' error. Although possessing several attractive features, there are some drawbacks in the ZZ error estimator. An interesting discussion is found in [2, p.82] and in [60].

The implementation of the ZZ error estimator for the deviatoric stress tensor ($\boldsymbol{\tau}$) is written in a vectorized form, i.e., for SSA we have $\nabla u \rightarrow \vec{\tau} = \left[\tau_{xx} \, \tau_{yy} \, \tau_{xy} \right]^{\intercal}$. For the ice thickness, we have $u = H$. In practice, our ZZ estimator for the deviatoric stress takes into account the gradient of the velocity field multiplied by the non-linear viscosity, which in its turn depends on the gradient of the velocity field (see Section 2.5).

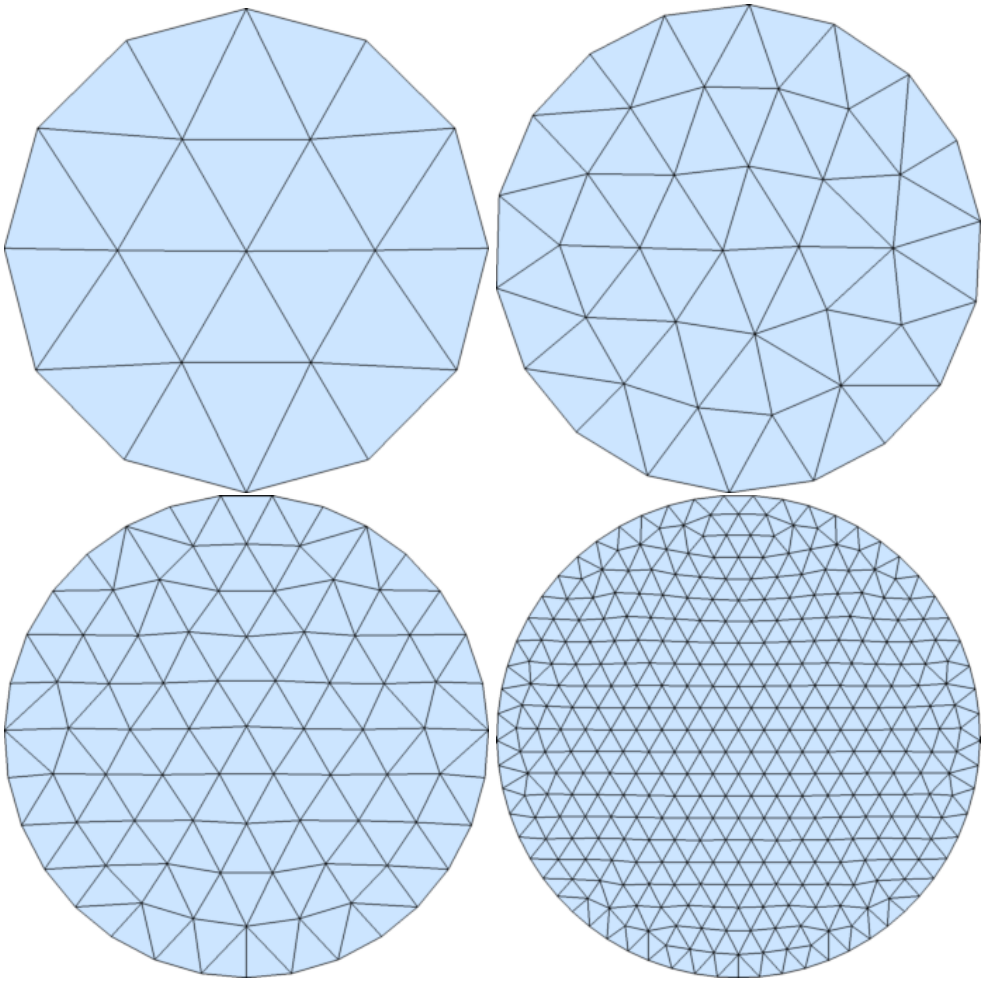

Figure 3.9: Geometric representation of the unit circle using different mesh resolutions.

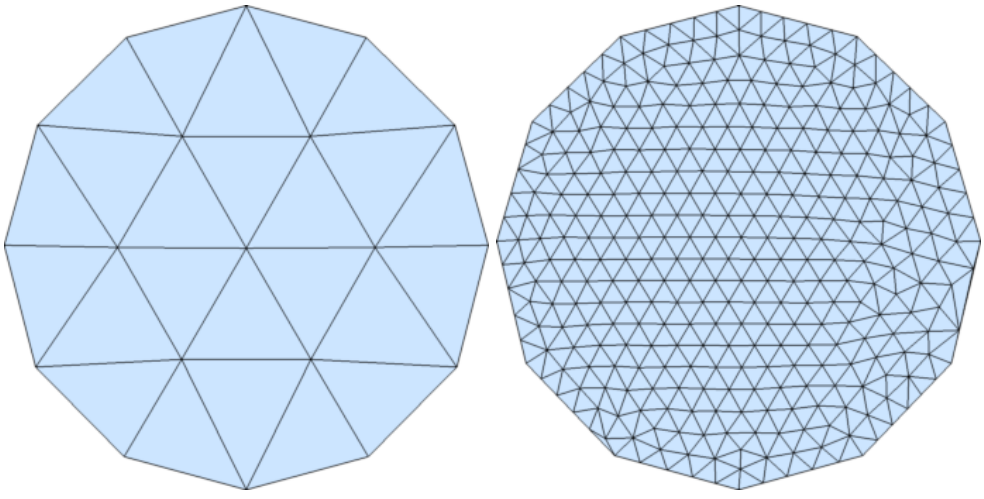

Figure 3.10: Example of mesh refinement using the coarse representation of the unit circle.

Algorithm 2 AMR core: refinement criteria calculation, refinement and coarsening processes. e = element. g = group of elements that are nested and derived from a refined element. $L(e)$ = level of refinement of the element e. L^{max} = maximum level of refinement. R^{max} = maximum threshold for element/group distance to the grounding line. ϵ^{max} = maximum threshold for element/group error estimator (thickness/deviatoric stress). θ = binary flags that define the criteria.

1. if $\theta_{gl} = 1$,
   then **compute** element and group distances to the grounding line, $R_{gl}(e)$ and $R_{gl}(g)$.
2. if $\theta_{\tau} = 1$,
   then **compute** element and group deviatoric stress error estimators, $\epsilon_{\tau}(e)$ and $\epsilon_{\tau}(g)$.
3. if $\theta_{H} = 1$,
   then **compute** element and group thickness error estimators, $\epsilon_{H}(e)$ and $\epsilon_{H}(g)$.
4. for each element e such that $L(e) < L^{max}$, do:
   if $\left[R_{gl}(e) < \theta_{gl} \cdot R^{max}_{gl,e}\right]$ or if $\left[\theta_{\tau} \cdot \epsilon_{\tau}(e) > \epsilon^{max}_{\tau,e}\right]$ or if $\left[\theta_{H} \cdot \epsilon_{H}(e) > \epsilon^{max}_{H,e}\right]$,
   then **refine** e.
5. for each group g, do:
   if $\left[R_{gl}(g) > \theta_{gl} \cdot R^{max}_{gl,g}\right]$ and if $\left[\theta_{\tau} \cdot \epsilon_{\tau}(g) < \epsilon^{max}_{\tau,g}\right]$ and if $\left[\theta_{H} \cdot \epsilon_{H}(g) < \epsilon^{max}_{H,g}\right]$,
   then **coarsen** g.

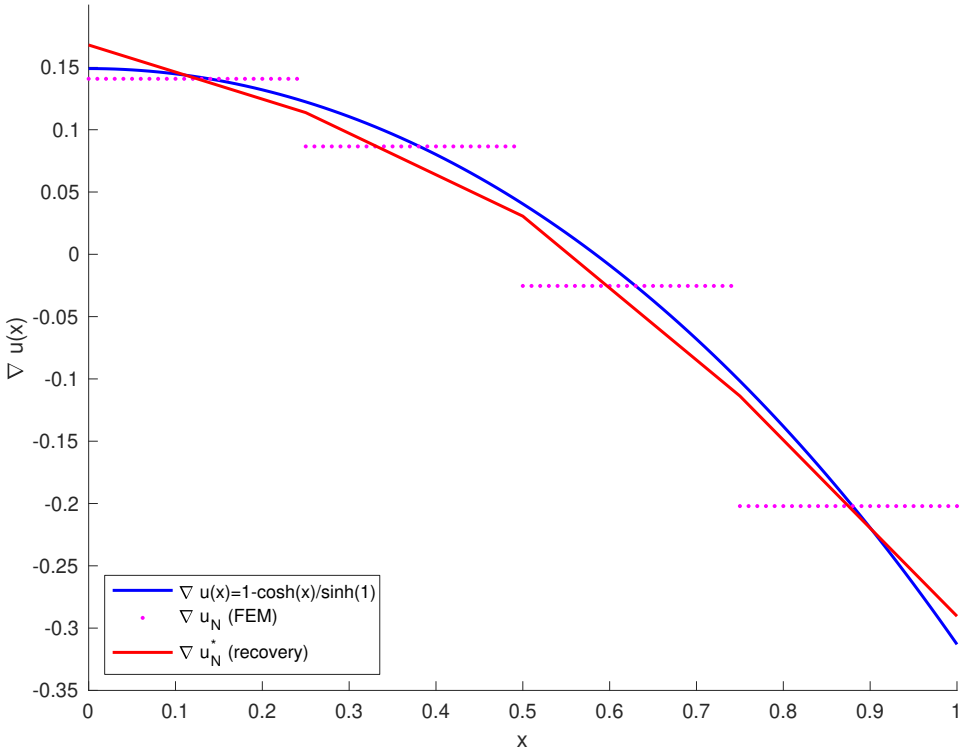

Figure 3.11: Comparison of gradients (exact gradient, FEM gradient, and recovery gradient) of the boundary-value problem A.1. The FEM gradient is given by the derivative of $u_N(x)$, Eq. A.34. Here, in this example, $\nabla \equiv d/dx$.

Chapter 4

Results

4.1 Introduction

We describe the numerical experiments used to assess the implementation of adaptive mesh refinement in ISSM. We compare the grounding line positions obtained with both uniform and adaptive meshes. The results from adaptive meshes should be as close as possible (within an acceptable tolerance) to those obtained from uniformly refined mesh, for the same level of refinement applied in both meshes. This comparison is an indicator of the adaptive mesh refinement performance. We run two different numerical experiments to assess our implementation. The first experiment is based on the Marine Ice Sheet Model Intercomparison Project 3D, MISMIP3d[1]. The second experiment is the MISMIP+, part of the Marine Ice Sheet-Ocean Model Intercomparison Project, MISOMIP[2].

4.2 MISMIP3d

The MISMIP3d experiment [118] is a similar initiative to the Marine Ice Sheet Model Intercomparison Project, MISMIP[3], a previous project with the purpose to evaluate numerical models along a flowline (xz-plane). MISMIP3d adds the y-axis to the physical domain, incorporating complexity in the ice flux through the buttressing effect during the perturbation phase of the experiment. The purpose of these experiments is to assess the reversibility of numerical models in terms of grounding line migration, as prescribed by the boundary layer theory [137, 136].

The bedrock elevation has a constant slope given by:

$$r(x, y) = -100 - x, \tag{4.1}$$

where r (m) is the bedrock elevation, being positive if above sea level, and x (km) is the horizontal coordinate. The domain (xy-plane) is rectangular ($800 \times 50\, km$) and the ice flux occurs in the

[1] http://homepages.ulb.ac.be/ fpattyn/mismip3d/

[2] http://www.climate-cryosphere.org/activities/targeted/misomip

[3] http://homepages.ulb.ac.be/ fpattyn/mismip/welcome.html

x-direction. The boundary conditions are defined as:

$$\begin{aligned} u_x &= 0 \text{ at } x = 0\,km; \\ u_y &= 0 \text{ at } y = 0\,km; \\ u_y &= 0 \text{ at } y = 50\,km; \\ 4\mu\frac{\partial u_x}{\partial x} &= \frac{\rho g H^2}{2\rho_w}(\rho_w - \rho) \text{ at } x = 800\,km. \end{aligned} \tag{4.2}$$

The default physical parameters are defined in Table 4.1. The friction model considered is the Weertman-type law, Eq. 2.75.

Table 4.1: Physical parameters used in MISMIP3d [118].

Parameter	Symbol [unit]	Value
ice density	$\rho\ [kg/m^3]$	900
water density	$\rho_w\ [kg/m^3]$	1000
gravitational acceleration	$g\ [m/s^2]$	9.8
Glen's law exponent	n	3
Glen's law coefficient	$A\ [Pa^{-3}s^{-1}]$	10^{-25}
bed friction exponent*	m	$1/3$
bed friction coefficient*	$C\ [Pa\,m^{-1/3}s^{1/3}]$	10^7
surface mass balance	$\dot{m}_s\ [m/yr]$	0.5
seconds per year	$[s/yr]$	$31,536,000$

*Considering a Weertman-type friction law (Eq. 2.75).

The numerical experiment consists of 3 phases: steady state (Stnd), basal sliding perturbation (P75S) and basal sliding restoring (P75R). The Stnd phase is initialized with a constant 10 m-thick ice shelf, and runs forward in time until a steady state is reached (which occurs after $\sim 30,000\,yr$). The P75S phase starts from the steady state geometry obtained in Stnd, and runs forward in time for 100 yr with a bed friction coefficient perturbation $C*$ defined as:

$$C^* = C\left\{1 - a\exp\left[-\frac{(x-x_b)^2}{2x_c^2} - \frac{(y-y_b)^2}{2y_c^2}\right]\right\}, \tag{4.3}$$

where $a = 0.75$, x_b is the grounding line position at $y = 0\,km$ obtained from Stnd, $y_b = 0\,km$, $x_c = 150\,km$ and $y_c = 10\,km$. The P75R phase starts at the end of P75S, and the bed friction coefficient is restored to the original value; then, the model runs forward in time until a steady state is reached (after $\sim 30,000\,yr$).

We investigate the effect of the refinement criteria based on the element distance to the grounding line, R_{gl}, as defined in Section 3.9. Three different distances are used for comparison: $R_{gl} = 5$, 10, and 15 km. The adaptive meshes generated by these criteria are labeled as AMR R5, AMR R10, and AMR R15, respectively. Table 4.2 summarizes the criteria used in MISMIP3d. The coarse resolution, common for all uniform and adaptive meshes, is equal to 5 km. We refine up to 3 levels of refinement, and the corresponding mesh resolutions are 2.5 km (1 level), 1.25 km

(2 levels), and 0.625 km (3 levels). Table 4.3 summarizes the correspondence between level of refinement and mesh resolution. We use both Bamg and NeoPZ to run the Stnd experiments. For the perturbation experiments, P75S and P75R, we use only Bamg.

Table 4.2: Refinement criteria used in MISMIP3d.

Label	Criterion
AMR R5	distance of 5 km to GL
AMR R10	distance of 10 km to GL
AMR R15	distance of 15 km to GL

GL=grounding line.

Table 4.3: Level of refinement and mesh resolution used in MISMIP3d.

Level	Label	Resolution
0 (CM)	L0	5 km
1	L1	2.5 km
2	L2	1.25 km
3	L3	625 m

CM=coarse mesh.

In addition, we investigate the sensitivity of adaptive mesh refinement to different grounding line parameterizations into the elements, as implemented in ISSM [138]. We test three different sub-element parameterizations (SEPs): NSEP, SEP1, and SEP2 (see Section 3.5). Figure 4.2 presents the grounding line positions at steady state condition (Stnd experiment) for different meshes and sub-element parameterizations as a function of number of elements. The refinement criterion used is the element distance to the grounding line, R_{gl} (see Section 3.9). Grounding line positions obtained with uniformly refined meshes are also shown in Figure 4.2. The grounding line positions and the ice volume above floatation (VAF[4]) as a function of mesh resolutions are present in Figure 4.1. For NSEP, the grounding line position varies between 200 km and 520 km for meshes L0 (coarse mesh) and L3, respectively. For these same meshes, the grounding line position varies between 620 km and 600 km for SEP1, and 550 km and 600 km for SEP2. The boundary layer theory [136] predicts a grounding line position at $\sim$ 606.8 km.

We note that grounding line positions obtained with NeoPZ are similar to the ones produced with uniformly refined mesh. This holds for all sub-element parameterizations and values of R_{gl}. Adaptive mesh refinement using Bamg is more sensitive to NSEP, for which grounding line positions depend on the R_{gl} chosen, especially for the lower refinement level (level equal to 1). Nevertheless, grounding line positions from adaptive meshes using Bamg are in agreement with uniformly refined meshes for SEP1 and SEP2. Table 4.4 summarizes the ratio between the number of elements for adaptive and uniformly refined meshes using NeoPZ and Bamg (in parentheses). Virtually, adaptive meshes using NeoPZ and Bamg have the same computational cost. For example, for the level of refinement equal to 3 (L3), the number of elements in adaptive meshes represents 4% (3%) to 7% (6%) of the number of elements present in uniformly refined meshes, depending on the R_{gl} value.

[4]The ice volume above floatation is the ice volume that contributes to sea level rise [17].

Table 4.4: Ratio between the number of elements in adaptive meshes and uniformly refined meshes using NeoPZ and Bamg. The ratio obtained with Bamg are in parentheses. Sub-element parameterization used: SEP1.

Level	R5	R10	R15
L1	0.27 (0.30)	0.28 (0.31)	0.29 (0.32)
L2	0.08 (0.08)	0.10 (0.10)	0.11 (0.11)
L3	0.04 (0.03)	0.05 (0.05)	0.07 (0.06)

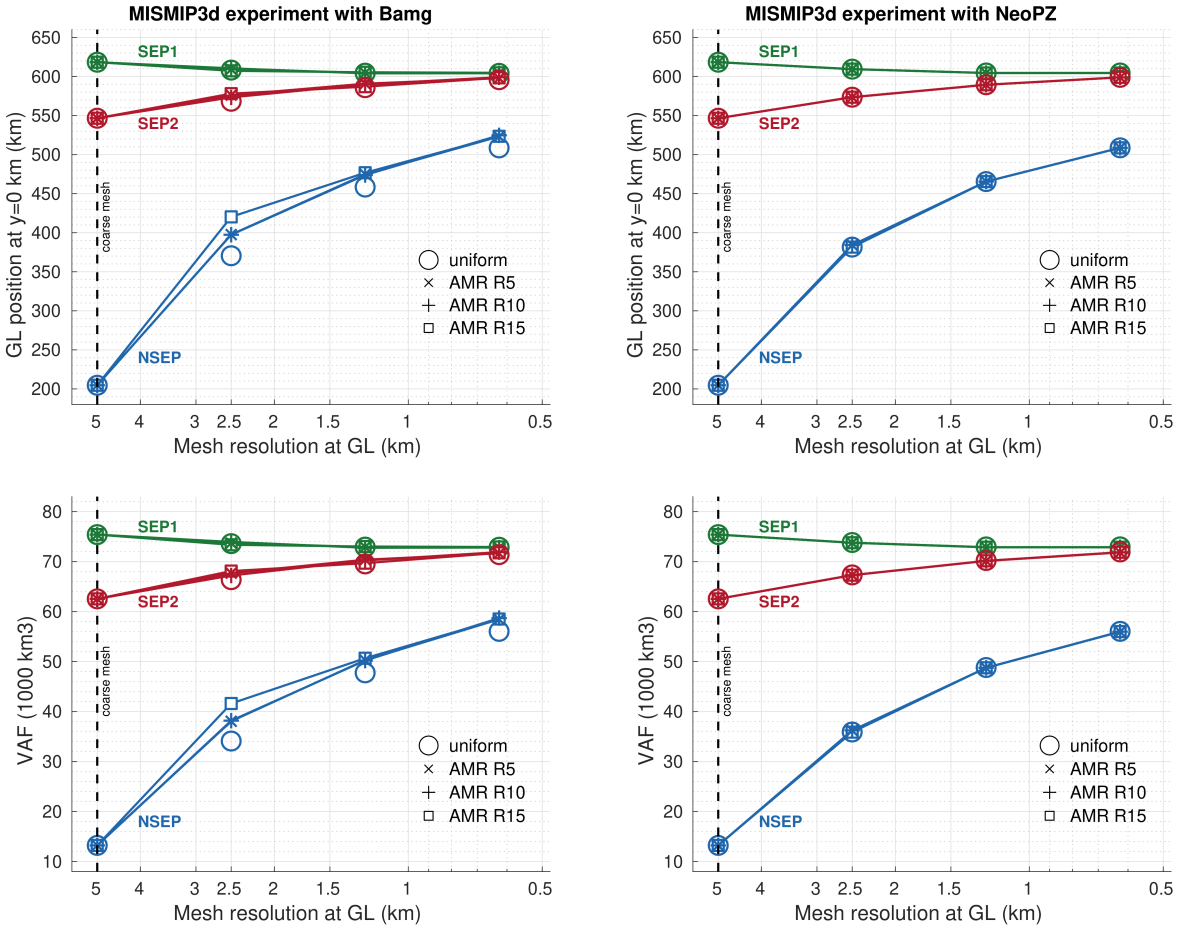

Figure 4.1: Grounding line (GL) position and volume above floatation (VAF) convergence in terms of mesh resolution, for three sub-element parameterizations: NSEP, SEP1, and SEP2. Both uniform and adaptive meshes are shown. The mesh resolutions refer to coarse and refined meshes (see Table 4.3).

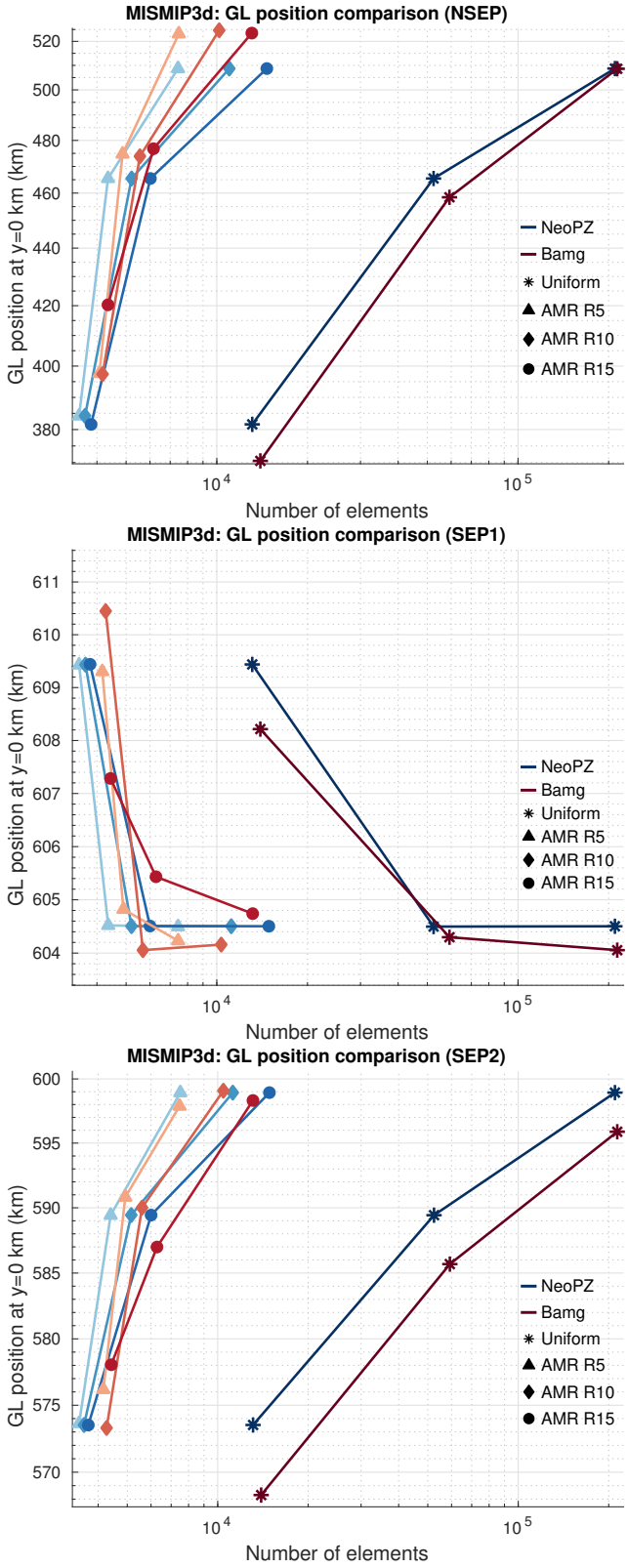

Figure 4.2: Grounding line (GL) position convergence in terms of number of elements, for three sub-element parameterizations: NSEP, SEP1, and SEP2. Both uniform and adaptive meshes are shown. Three levels of refinement are shown: L1, L2, and L3.

The grounding line positions at the end of the friction perturbation experiments (P75S and P75R) are present in Table 4.5. The grounding line positions at the end of the steady state phase (Stnd) is also shown. We use Bamg and SEP1 in the P75S and P75R phases. Based on the boundary layer theory [136], the grounding line positions at the end of Stnd and P75R experiments should be the same, since a unique solution is expected in a bedrock shape like MISMIP3d [136, 119, 118]. Therefore, we should expect a reversibility behavior in the grounding line movement. Through Table 4.5, we note the grounding line reversibility is virtually obtained for all refinement criteria used, for all levels of refinement. For AMR R5 meshes, there is a small difference between Stnd and P75R, even for the highest level of refinement. Figures 4.3 and 4.4 show the grounding positions at the end of Stnd, P75S and P75R. The adaptive meshes at the end of P75S are also shown, as well as the ice velocity.

We also perform the experiments using the ZZ error estimator calculated for the deviatoric stress tensor. Figures 4.5 show the grounding line positions at the end of Stnd, P75S and P75R, as well as the adapted mesh at the end of P75S. The thresholds for element/group used are, respectively, $\epsilon_{\tau,e}^{max} = 0.03\epsilon_{\tau}^{max}$ and $\epsilon_{\tau,g}^{max} = 0.001\epsilon_{\tau}^{max}$, where ϵ_{τ}^{max} is the maximum estimated error observed at the end of Stnd using the coarse mesh. We note that the reversibility in the grounding line movement is achieved, although a small difference is observed between Stnd and P75R. We suspect that this difference could be reduced by adjusting ('tightening') the error thresholds.

Table 4.5: Grounding line positions (km) at the end of the Stnd, P75S and P75R experiments using Bamg and SEP1. Positions at $y = 0\,km$ and at $y = 50\,km$

Level	Criteria	Stnd	P75S	P75R	Stnd	P75S	P75R
			$y = 0\,km$			$y = 50\,km$	
L1	AMR R5	609.3	619.6	609.1	609.4	603.4	609.0
L1	AMR R10	610.4	620.7	607.0	610.7	604.7	607.3
L1	AMR R15	607.3	617.8	607.3	607.2	601.1	607.2
L2	AMR R5	604.8	615.3	604.3	605.0	599.8	604.4
L2	AMR R10	604.1	614.2	603.8	603.9	597.8	603.8
L2	AMR R15	605.4	615.3	605.3	605.2	599.1	605.1
L3	AMR R5	604.2	614.5	603.9	604.2	598.1	603.8
L3	AMR R10	604.2	614.2	604.2	604.1	598.0	604.2
L3	AMR R15	604.7	614.7	604.7	604.8	598.5	604.8

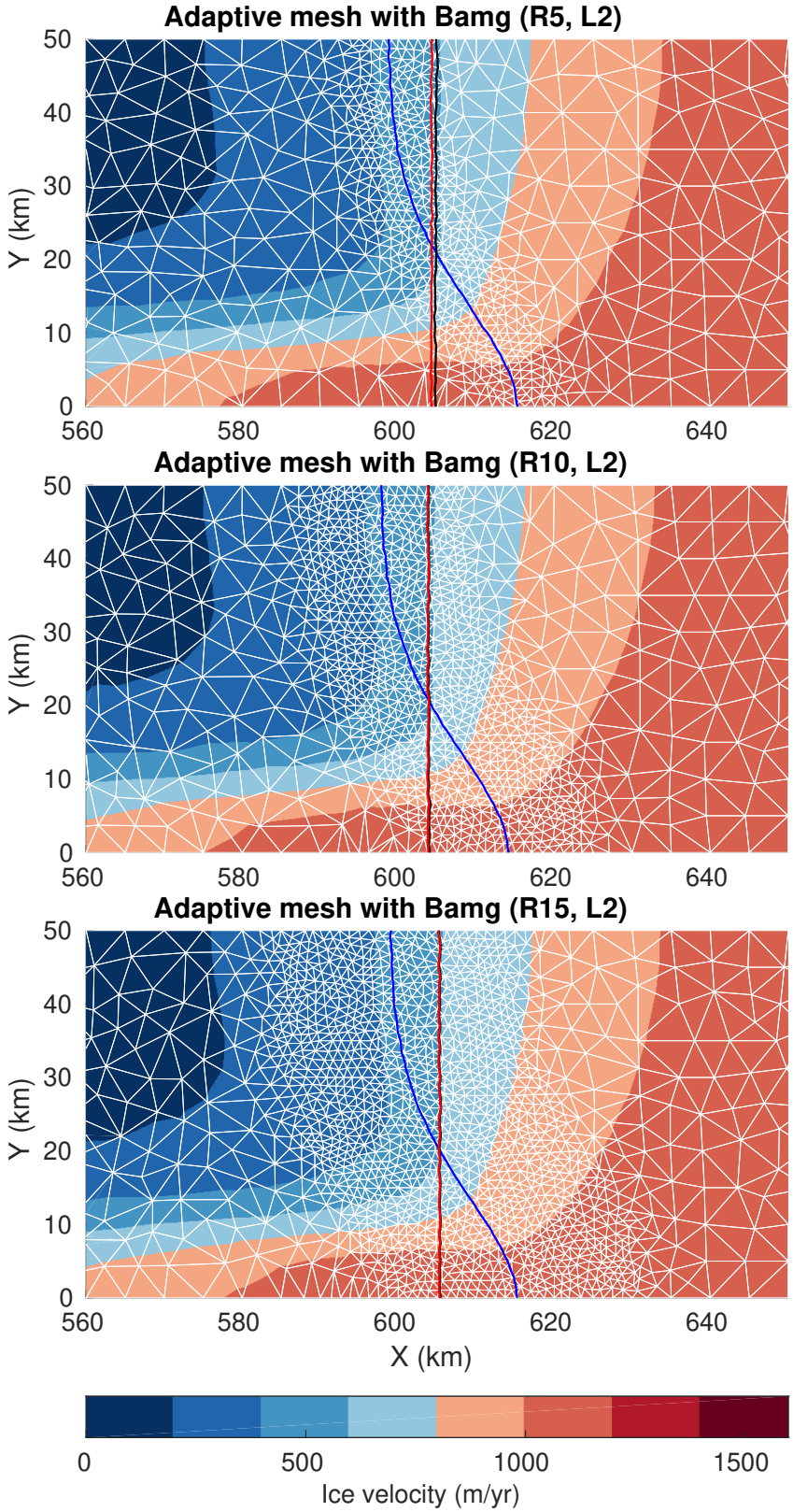

Figure 4.3: Adaptive meshes for the P75S experiment with level of refinement equal to 2 (L2) and different values of R_{gl}: R5, R10, and R15. Blue line: grounding line at the end of P75S. Red line: grounding line at the end of P75R. Black line: grounding line at the end of Stnd.

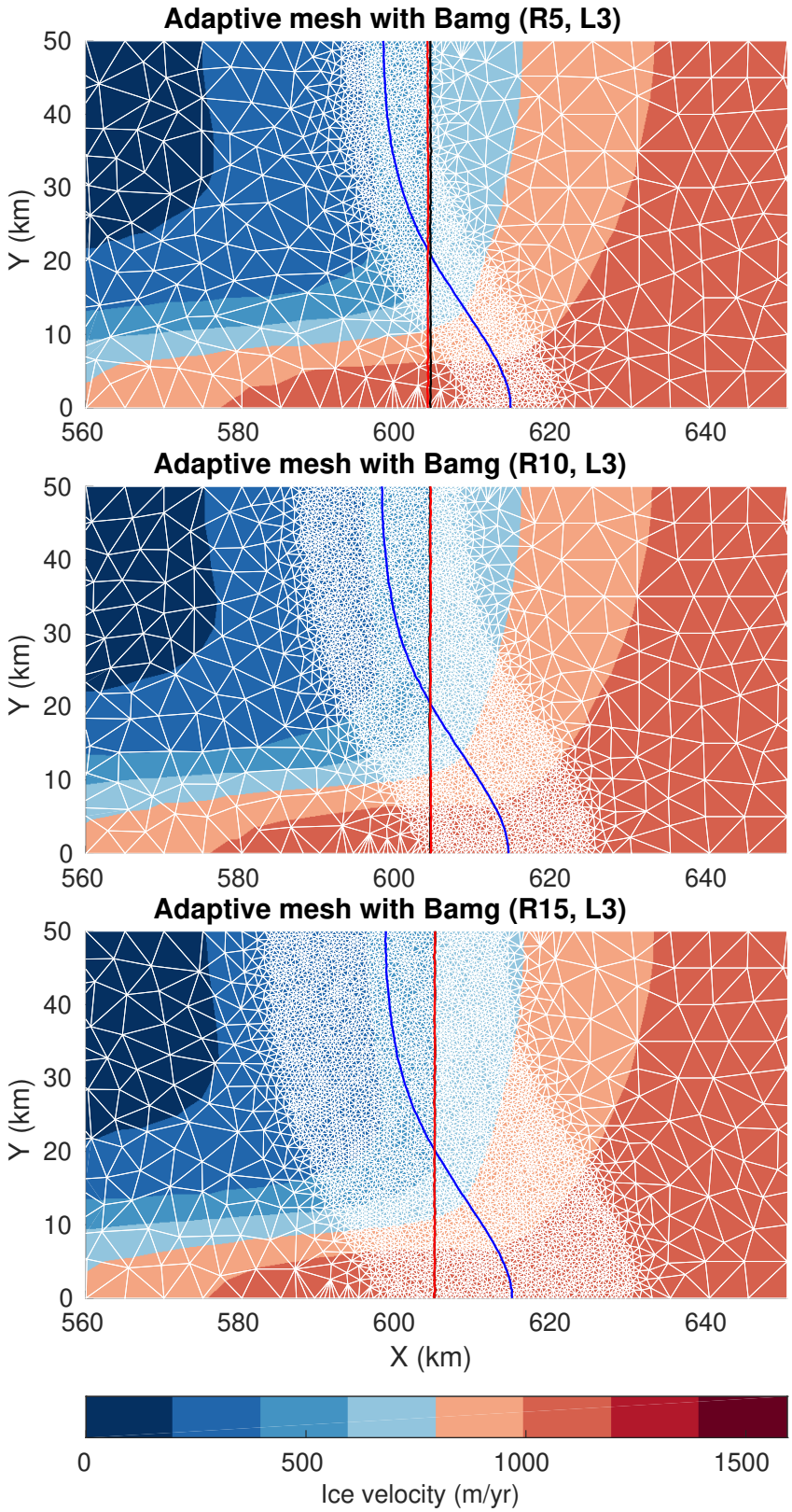

Figure 4.4: Adaptive meshes for the P75S experiment with level of refinement equal to 3 (L3) and different values of R_{gl}: R5, R10, and R15. Blue line: grounding line at the end of P75S. Red line: grounding line at the end of P75R. Black line: grounding line at the end of Stnd.

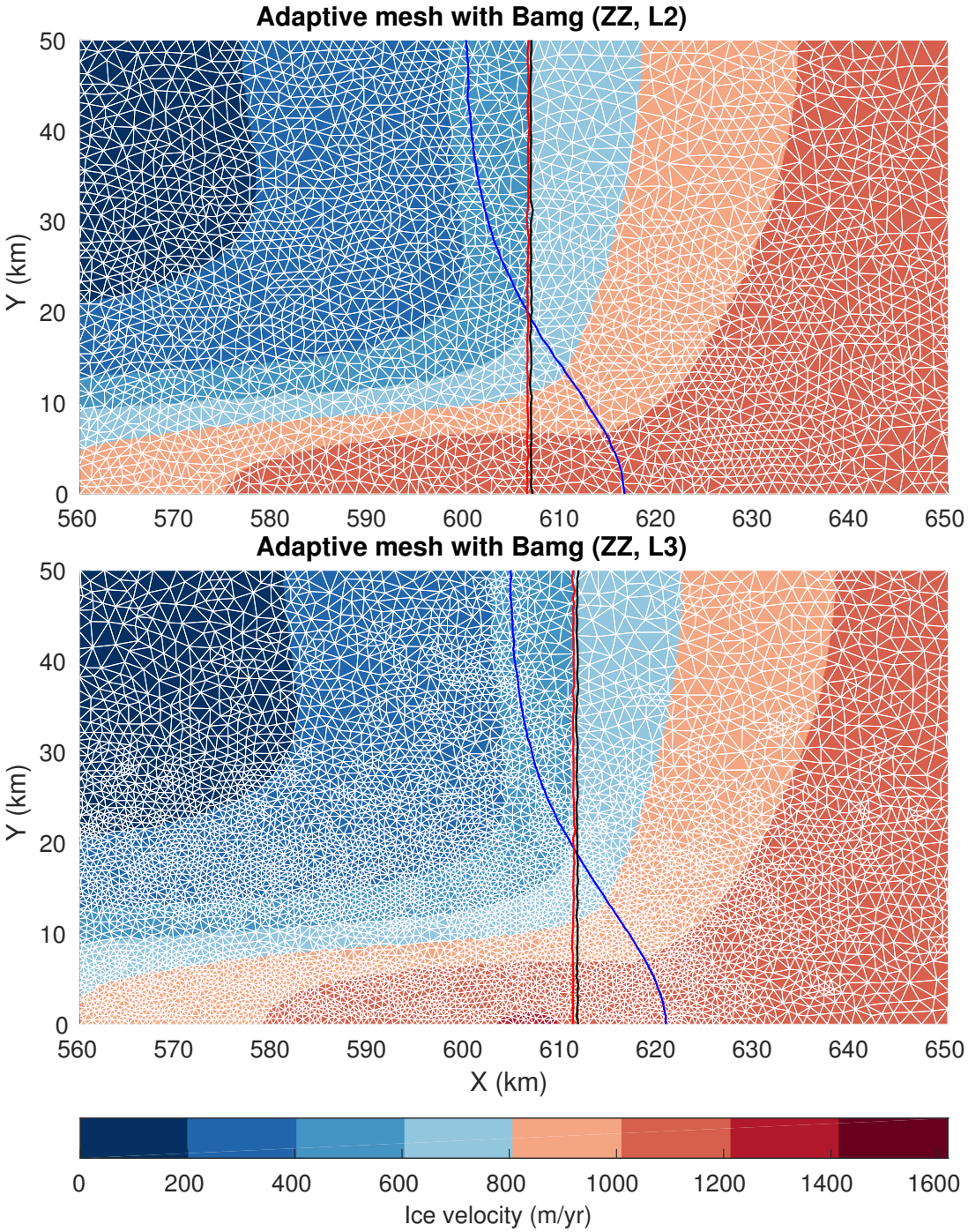

Figure 4.5: Adaptive meshes for the P75S experiment with levels of refinement equal to 2 (L2, top) and 3 (L3, bottom) using the ZZ error estimator for the deviatoric stress tensor. Blue line: grounding line at the end of P75S. Red line: grounding line at the end of P75R. Black line: grounding line at the end of Stnd.

4.3 MISMIP+

The MISOMIP [7] project is an effort of the Climate and Cryosphere[5], a core project of the World Climate Research Programme[6], an international organization that coordinates global climate research. The MISOMIP initiative aims to design idealized numerical setups based on the West Antarctic Ice Sheet, and to compare the behavior of different ice sheet-ocean models in terms of grounding line dynamics and ice discharge induced by ocean-melting forcing. Recent observations show strong correlation between the grounding line retreat and warmer ocean circulations in WAIS region (e.g., [78, 84, 140]), and future projections of sea level rise due to WAIS depend on ice sheet models coupled with ocean models.

The MISOMIP program is based on three model intercomparison projects (MIPs): an updated version of the Ice Shelf-Ocean Model Intercomparison Project (ISOMIP+), a third version of the Marine Ice Sheet Model Intercomparison Project (MISMIP+), and the first version of the Marine Ice Sheet-Ocean Model Intercomparison Project (MISOMIP). Here, we focus only in MISMIP+, where the melting induced by the ocean is parameterized within the ice sheet model.

The MISMIP+ bedrock elevation is defined as:

$$r(x, y) = \max\left(r_x(x) + r_y(y),\, r_{deep}\right), \tag{4.4}$$

with:

$$\begin{aligned} r_x(x) &= r_0 + r_2\left(\frac{x}{\bar{x}}\right)^2 + r_4\left(\frac{x}{\bar{x}}\right)^4 + r_6\left(\frac{x}{\bar{x}}\right)^6, \\ r_y(y) &= \frac{d}{1+\exp\left[-2(y - L_y/2 - w_c)/f_c\right]} + \frac{d}{1+\exp\left[2(y - L_y/2 + w_c)/f_c\right]}, \end{aligned} \tag{4.5}$$

where $r\,(m)$ is the bedrock elevation (positive if above sea level), $x\,(km)$ and $y\,(km)$ are the horizontal coordinates, $r_{deep} = -720\,m$, $r_0 = -150.0\,m$, $r_2 = -728.8\,m$, $r_4 = 343.91\,m$, $r_6 = -50.57\,m$, $\bar{x} = 300\,km$, $d = 500\,m$, $L_y = 80\,km$, $w_c = 24\,km$, and $f_c = 4\,km$. The domain is rectangular ($640 \times 80\,km$) and the ice flux occurs in the x-direction. The bedrock is designed to induce strong buttressing through lateral stress (on the ice shelf) such that the grounding line stabilizes on the bed part with retrograde slope. Figure 4.6 shows the MISMIP+ bedrock elevation. The boundary conditions are defined as:

$$\begin{aligned} u_x &= 0 \text{ at } x = 0\,km; \\ u_y &= 0 \text{ at } y = 0\,km; \\ u_y &= 0 \text{ at } y = 80\,km; \\ 4\mu\frac{\partial u_x}{\partial x} &= \frac{\rho g H^2}{2\rho_w}(\rho_w - \rho) \text{ at } x = 640\,km. \end{aligned} \tag{4.6}$$

[5]CliC, http://www.climate-cryosphere.org
[6]WCRP, https://www.wcrp-climate.org

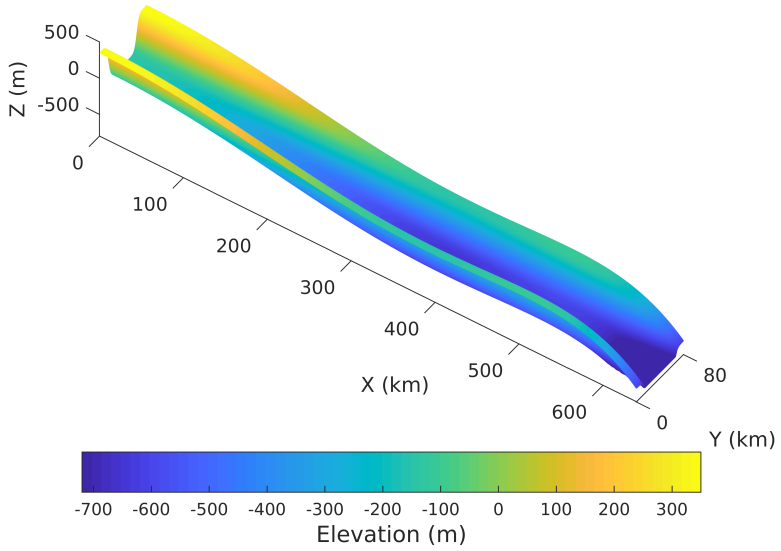

Figure 4.6: Bedrock elevation used in the MISMIP+ experiments.

The physical parameters are presented in Table 4.6. The friction model is the Weertman-type law, Eq. 2.75. The basal melting $\dot{m}_b$ is parameterized as:

$$\dot{m}_b = \dot{m}_{b0} \tanh\left(\frac{H_c}{H_{c0}}\right) \max\left(b_0 - b, 0\right), \tag{4.7}$$

where $\dot{m}_{b0}$ is the melt-rate factor, H_c is the ocean-cavity thickness ($H_c = b - r$), H_{c0} is the reference thickness, b is the ice base (negative if below sea level), and b_0 is the depth above which the melt is zero.

It is important to emphasize that the MISMIP+ bed elevation (Figure 4.6) is calculated directly in code every time AMR core is called (step 'e.5', Algorithm 1). This procedure avoids excessive smoothing of complex bedrock features in refined regions.

The MISMIP+ experiment consists of three phases with different basal melting: Ice0, Ice1 and Ice2, being Ice0 a control simulation, and Ice1 and Ice2r are divided in Ice1r, Ice1ra, Ice1rr and Ice2r, Ice2ra, Ice2rr, respectively. All these phases start from a steady state condition (Stnd), which is reached with no basal melting ($\dot{m}_b = 0$). This steady state condition is characterized by a grounding line position stabilized on a retrograde bed slope at the center of the channel ($y = 40\,km$). The steady state is reached after $20,000\,yr$ starting from a $100\,m$-thick ice stream. Table 4.7 summarizes the experimental phases. The Ice1r experiment induces the loss of buttressing[7] by basal melting applied on the ice shelf (Eq. 4.7). Both Ice1ra and IceIrr start from the end of Ice1r, but in Ice1ra the basal forcing is turned off, while in Ice1rr the basal forcing is kept on. The decrease of buttressing is also considered in Ice2r experiment, where an extensive 'calving event' is simulated by a basal ice shelf melt-rate of $100\,m/yr$ applied at $x > 480\,km$. Similar to Ice1, both Ice2ra and Ice2rr start from the end of Ice2r: in Ice2ra, the basal forcing is turned off; in Ice2rr, the forcing is kept on.

[7]The basal melting produces thinning of the ice shelf, which reduces the buttressing.

Table 4.6: Physical parameters used in MISMIP+ [7].

Parameter	Symbol [unit]	Value
ice density	$\rho\ [kg/m^3]$	918
water density	$\rho_w\ [kg/m^3]$	1028
gravitational acceleration	$g\ [m/s^2]$	9.81
Glen's law exponent	n	3
Glen's law coefficient	$A\ [Pa^{-3}s^{-1}]$	6.338×10^{-25}
bed friction exponent*	m	$1/3$
bed friction coefficient*	$C\ [Pa\, m^{-1/3}s^{1/3}]$	3.160×10^6
surface mass balance	$\dot{m}_s\ [m/yr]$	0.3
seconds per year	$[s/yr]$	$31,556,926$
melt-rate factor	$\dot{m}_{b0}\ [yr^{-1}]$	0.2
depth above which the melt is zero	$b_0\ [m]$	-100
reference ocean-cavity thickness	H_{c0} [m]	75

*Considering a Weertman-type friction law (Eq. 2.75).

Table 4.7: Phases of MISMIP+ [7].

Phases	Basal melting ($\dot{m}_b$)	Description
Ice0	no	100-year control simulation
Ice1r	as given by Eq. 4.7	100-year with melt-induced retreat
Ice1ra	no	900-year simulation from the end of Ice1r
Ice1rr	as given by Eq. 4.7	900-year simulation from the end of Ice1r
Ice2r	$100\, m/yr$ for $x > 480\, km$	100-year with 'calving event'
Ice2ra	no	900-year simulation from the end of Ice2r
Ice2rr	$100\, m/yr$ for $x > 480\, km$	900-year simulation from the end of Ice2r

As performed in MISMIP3d experiments, we also investigate the sensitivity of the grounding line position to refinement criteria based on the element distance, R_{gl}. We choose element distances equal to $R_{gl} = 5$, $R_{gl} = 15$, and $R_{gl} = 30\, km$, and the respective meshes are labeled as AMR R5, AMR R15, and AMR R30. Table 4.8 summarizes the criteria used in MISMIP+. The coarse mesh resolution, common for all uniform and adaptive meshes, is equal to $4\, km$. Here, we refine up to 4 levels of refinement, and the corresponding mesh resolutions are $2\, km$ (1 level), $1\, km$ (2 levels), $0.5\, km$ (3 levels), and $0.25\, km$ (4 levels). Table 4.9 summarizes the correspondence between level of refinement and mesh resolution. We use both Bamg and NeoPZ to run the Stnd experiments. For the perturbation experiments (see Table 4.7), we use only Bamg.

The MISMIP+ bed topography is designed to induce a strong buttressing on the ice stream from the confined ice shelf. It is therefore expected that the results are more sensitive to the mesh refinement compared to simpler bedrock descriptions (e.g., MISMIP3d), since refining the mesh also improves the resolution of the bedrock geometry (valid only for MISMIP+).

Table 4.8: Refinement criteria used in MISMIP+.

Label	Criterion
AMR R5	distance of 5 km to GL
AMR R15	distance of 15 km to GL
AMR R30	distance of 30 km to GL
AMR ZZ	ZZ error estimator for τ

GL=grounding line. τ=deviatoric stress tensor.

Table 4.9: Level of refinement and mesh resolution used in MISMIP+.

Level	Label	Resolution
0 (CM)	L0	4 km
1	L1	2 km
2	L2	1 km
3	L3	500 m
4	L4	250 m

CM=coarse mesh.

Figure 4.8 presents the coarse mesh and three examples of adaptive meshes obtained with Bamg and NeoPZ and different criteria: element distance to the GL, R_{gl} (= 5 km, R5) and error estimator ZZ (see Table 4.8). The figure also shows the grounding line positions obtained with these meshes and with the most refined uniform mesh (250 m resolution). Figure 4.8 provides an example of a case for which the grounding line position remains resolution dependent and refinement criterion dependent. We can note that, using the same criterion based on the element distance to the grounding line (meshes R5), Bamg and NeoPZ produce different meshes, as expected. For Bamg, the mesh transition zone between the lowest and highest resolution is smoother than NeoPZ's mesh, since the resolutions in NeoPZ are obtained stepwise by nested elements. In Figure 4.8, at the center of the domain (y = 40 km), the grounding line position differs by 12 and 13 km between the most refined uniform mesh and the adaptive meshes generated by Bamg and NeoPZ, respectively. Between the coarse mesh and the adaptive meshes, the grounding line position differs by about 10 km (for both Bamg and NeoPZ). When the ZZ criterion is used, the grounding line positions differ by 6 km (17 km) in comparison with the one obtained from the most refined uniform mesh (coarse mesh). Figure 4.13 shows the grounding line positions at the beginning and end of the Ice1r phase for different meshes: coarse mesh, adaptive meshes (L4 AMR ZZ and L3 AMR R5+ZZ) and uniformly refined mesh (L4). We note that the grounding line positions obtained with the adapted meshes are in agreement with those obtained with the most (uniformly) refined mesh.

Figure 4.9 presents a set of results for the grounding line position and ice volume above floatation (VAF) at steady state (Stnd) as a function of mesh resolution. The evolution of the grounded area along all the experimental phases is summarized in Figure 4.11, while the evolution of VAF (Ice1r and Ice1ra phases) is summarized in Figure 4.12. Adaptive mesh

dependency is visible in Figure 4.9. For mesh adaptivity with NeoPZ, grounding line positions obtained with AMR R5 differ from the ones produced by AMR R15 and AMR R30. Virtually AMR R15 and AMR R30 produce the same grounding line positions. For mesh adaptivity with Bamg, AMR R5 and AMR R15 do not improve the position of the grounding line as the resolution increases. We can note that the differences of grounding line positions obtained with mesh adaptivity (with Bamg and NeoPZ) and with uniformly refined meshes are higher in comparison to MISMIP3d. The same adaptive mesh dependency is observed in the VAF values.

To investigate the possible causes of this adaptive mesh dependency, we perform the adaptive mesh refinement using the ZZ error estimator calculated for the deviatoric stress tensor, $\boldsymbol{\tau}$ (Table 4.8). The grounding line positions obtained with AMR ZZ are presented in Figure 4.9. We observe that grounding line positions with AMR ZZ are closer to the ones obtained with uniform meshes, for all mesh resolutions. To understand this AMR ZZ result, we plot the spatial distributions of the ZZ error estimator for the coarse and adaptive meshes (using NeoPZ), as illustrated in Figure 4.10. The ZZ error values are normalized between 0 and 1. For the coarse mesh, we see in Figure 4.10 that the error estimators calculated for the deviatoric stress tensor and ice thickness present high values around the grounding line. In particular, for the ice thickness, the estimator also presents high values in the grounded part of the marine ice sheet, following the high gradient presents in the side walls of the bedrock (see Figure 4.6). For AMR R5 meshes, there are high ZZ error values around the refined region. This is not observed when the refinement criterion used is the ZZ estimator (AMR ZZ), as expected. Using the ZZ criterion induces an equalization in the spatial distribution of the estimated errors, improving the solutions (e.g., grounding line position, see Figure 4.9). In terms of efficiency, AMR ZZ generates fewer elements than AMR R30. At the end of the experiment and for a level of refinement equal to 4 (resolution equal to $250m$), using NeoPZ, AMR R30 mesh has 464,712 elements, while AMR ZZ mesh has 24,428 elements (i.e., only $\sim$ 5% of the number of elements in AMR R30). In Figure 4.7 we see the number of elements generated in the adaptive and uniform meshes.

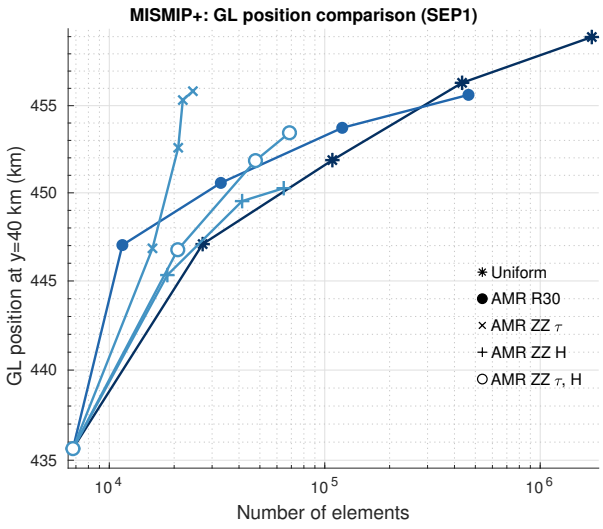

Figure 4.7: Grounding line (GL) position convergence in terms of number of elements. Both uniform and adaptive meshes are shown. AMR ZZ H: ZZ error estimator for the ice thickness. AMR ZZ τ, H: combination of estimators. Mesher used: NeoPZ.

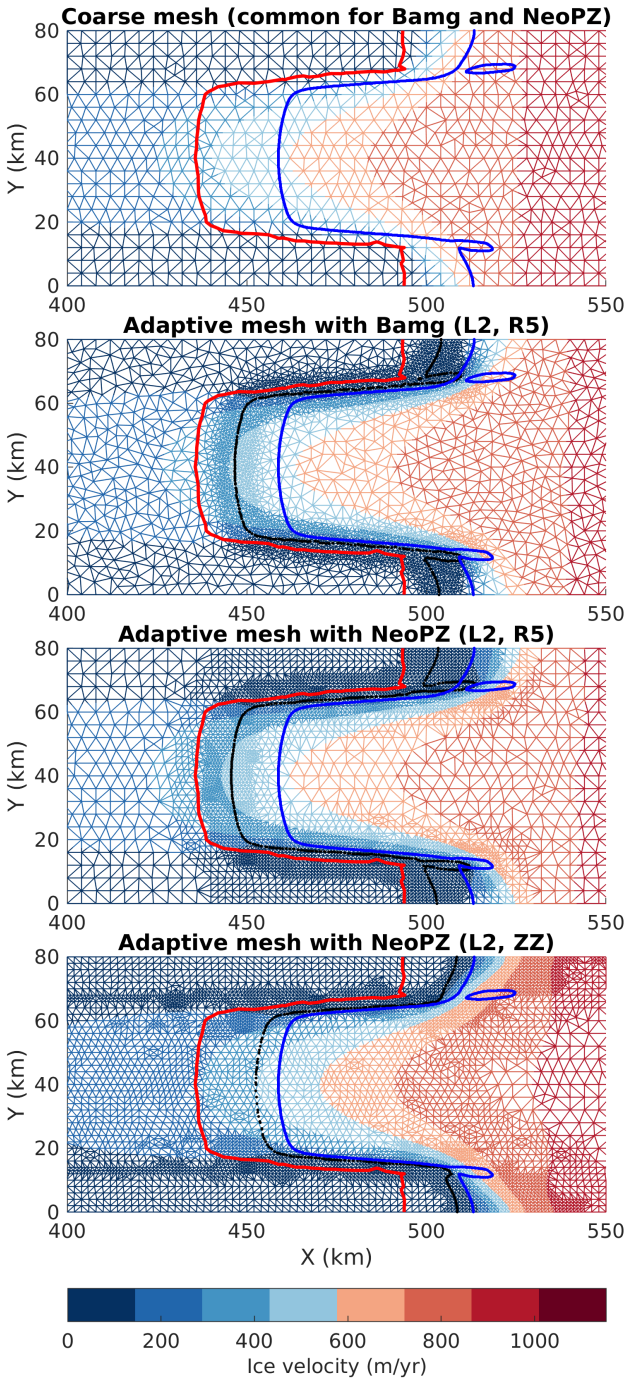

Figure 4.8: Examples of adaptive meshes for the MISMIP+ experiment using different refinement criteria and mesh generators (see Tables 4.8 and 4.9). Red line: grounding line position at steady state obtained with the coarse mesh. Black dots: grounding line position at steady state obtained with each adaptive mesh. Blue line: grounding line position at steady state obtained with the most refined mesh (L4, uniform). The thresholds used in the ZZ criterion are described in the legend of Figure 4.9.

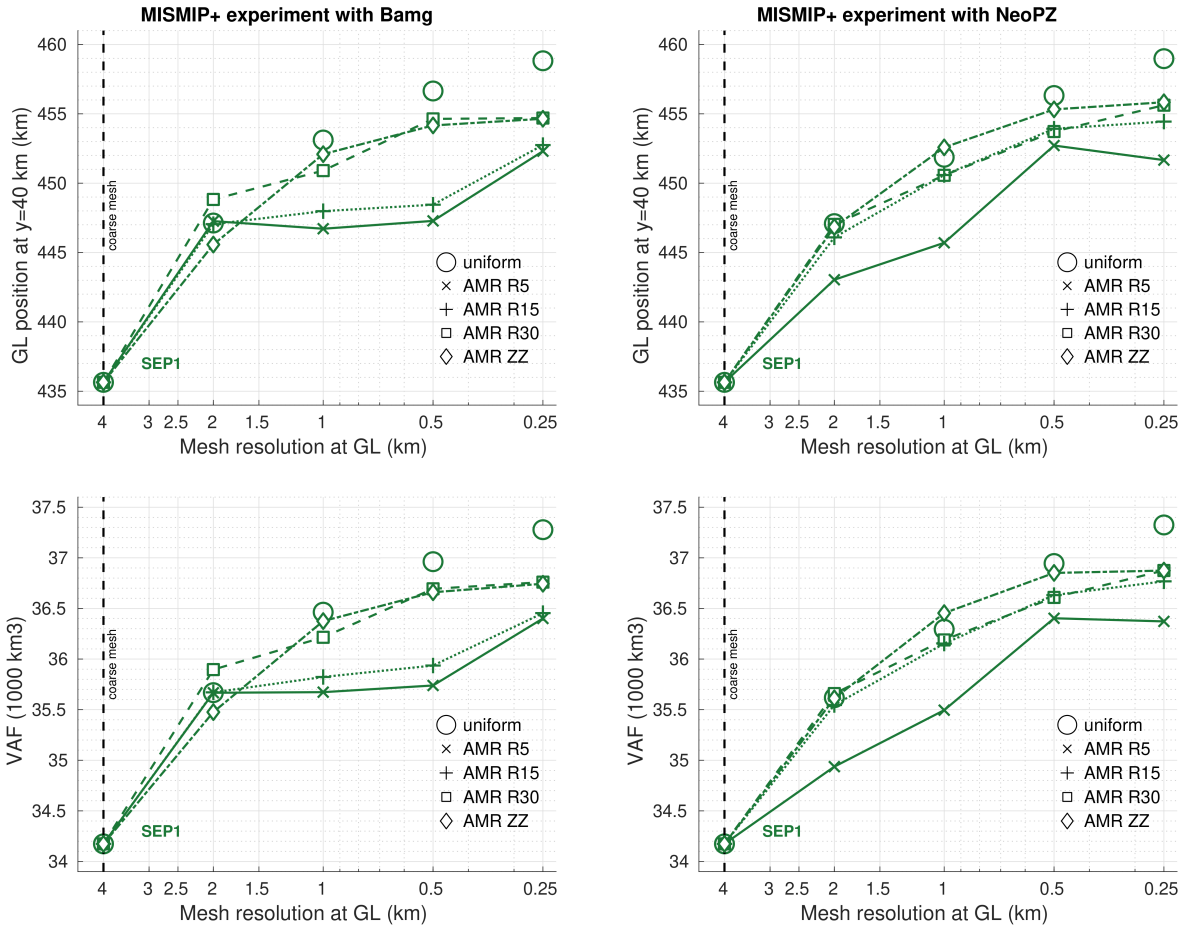

Figure 4.9: Grounding line (GL) position and volume above floatation (VAF) convergence in terms of mesh resolution. Both uniform and adaptive meshes are shown. The mesh resolutions refer to coarse and refined meshes (see Table 4.9). The thresholds for element/group used in the ZZ criterion are, respectively, $\epsilon_{\tau,e}^{max} = 0.08\epsilon_{\tau}^{max}$ (for both Bamg and NeoPZ) and $\epsilon_{\tau,g}^{max} = 0.04\epsilon_{\tau}^{max}$ for NeoPZ and $\epsilon_{\tau,g}^{max} = 0.008\epsilon_{\tau}^{max}$ for Bamg, where ϵ_{τ}^{max} is the maximum error value observed in the coarse mesh.

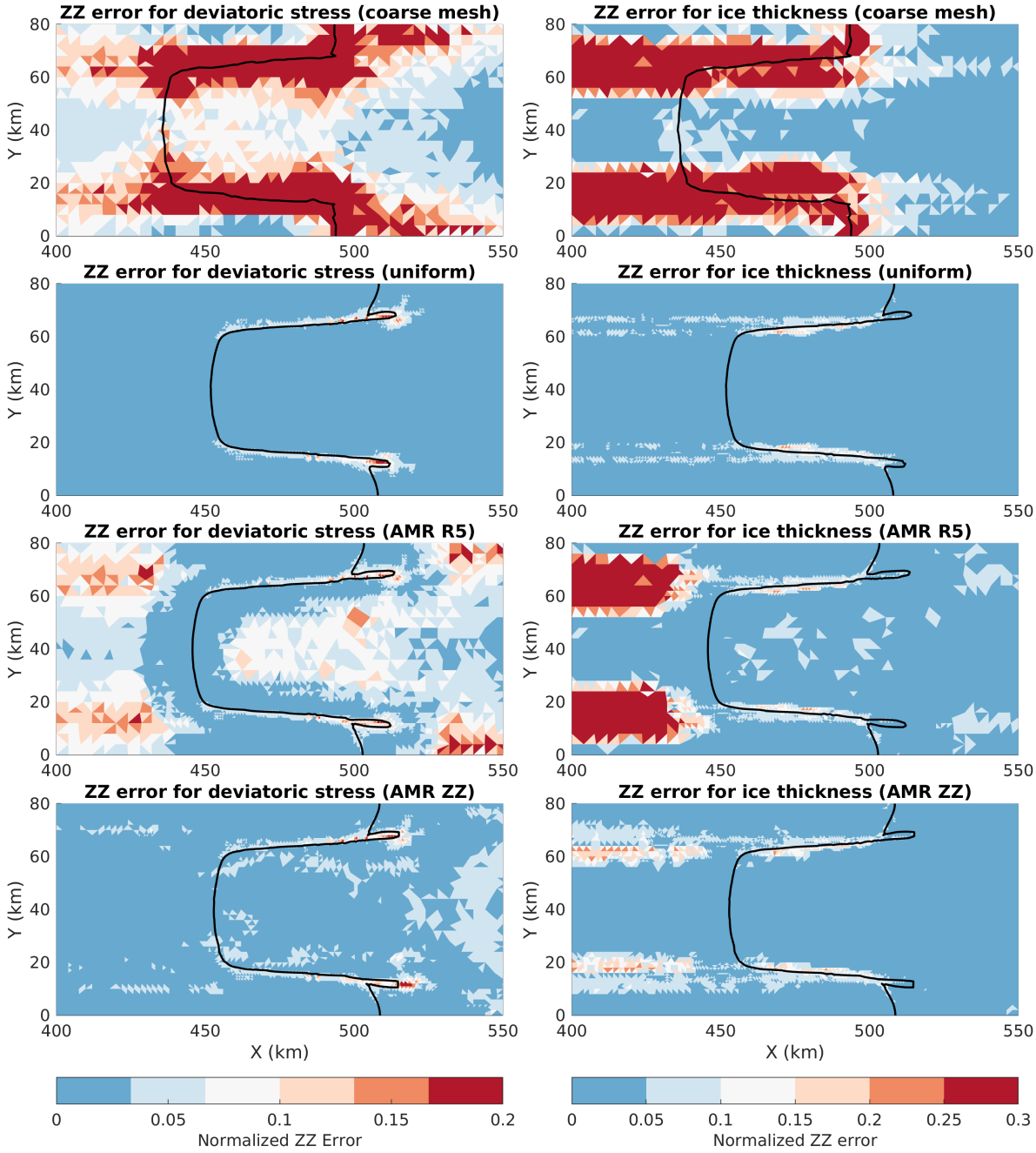

Figure 4.10: Spatial distribution of the ZZ error estimator in the coarse and refined meshes (uniform and adaptive) used in the MISMIP+ experiments. The ZZ error values are normalized between 0 and 1 using the maximum error value observed in the coarse mesh. Black lines are the grounding line positions at steady state obtained with the respective meshes. The refined meshes (uniform and adaptive) are generated by NeoPZ considering level of refinement equal to 2 (L2, see Table 4.9), and the criteria used (R5 and ZZ) are summarized in Table 4.8. The thresholds used in AMR ZZ are described in the legend of Figure 4.9.

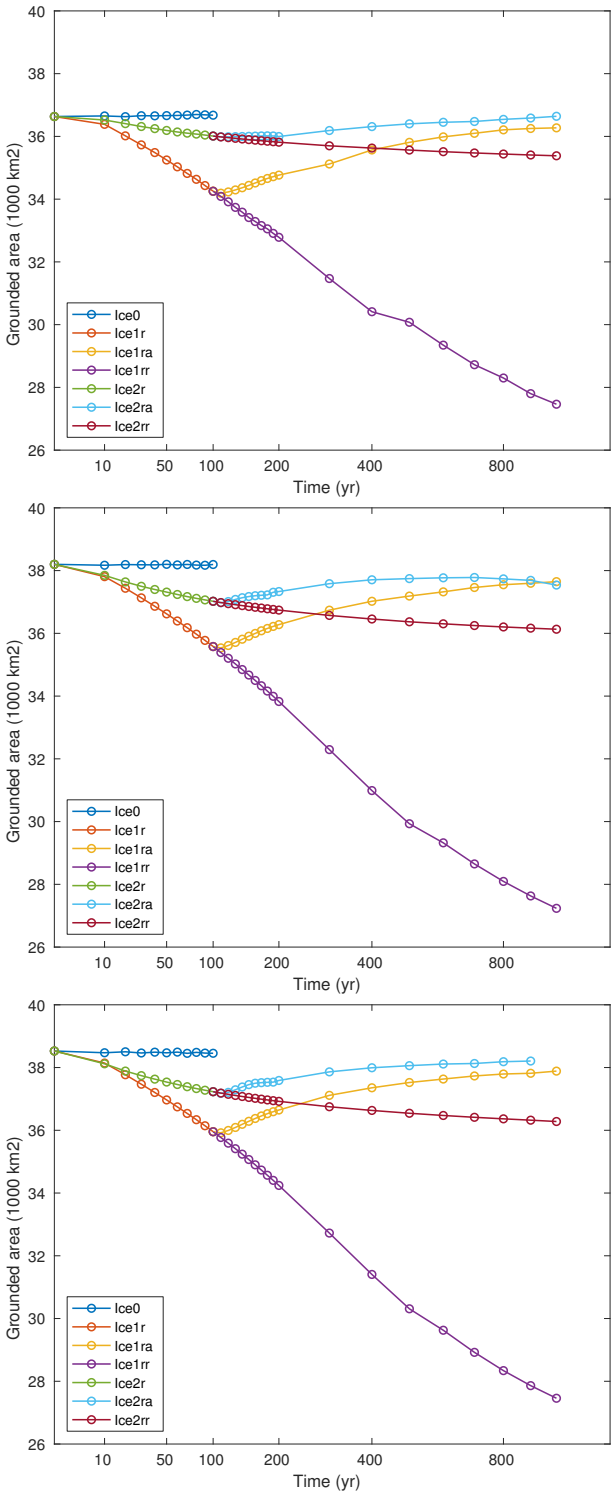

Figure 4.11: Grounded area evolution along the MISMIP+ phases for different meshes: coarse mesh (top), adaptive mesh (L3 AMR R5+ZZ, middle) and uniformly refined mesh (L4, bottom). The MISMIP+ phases are described in Table 4.7. The criterion R5+ZZ means the combination of the ZZ error estimator (deviatoric stress) and element distance to the grounding line (R_{gl} = 5 km, R5). The thresholds used for element/group in the ZZ criterion are, respectively, $\epsilon_{\tau,e}^{max} = 0.16\epsilon_{\tau}^{max}$ and $\epsilon_{\tau,g}^{max} = 0.016\epsilon_{\tau}^{max}$, where ϵ_{τ}^{max} is the maximum error value observed in the coarse mesh. Mesher used: Bamg.

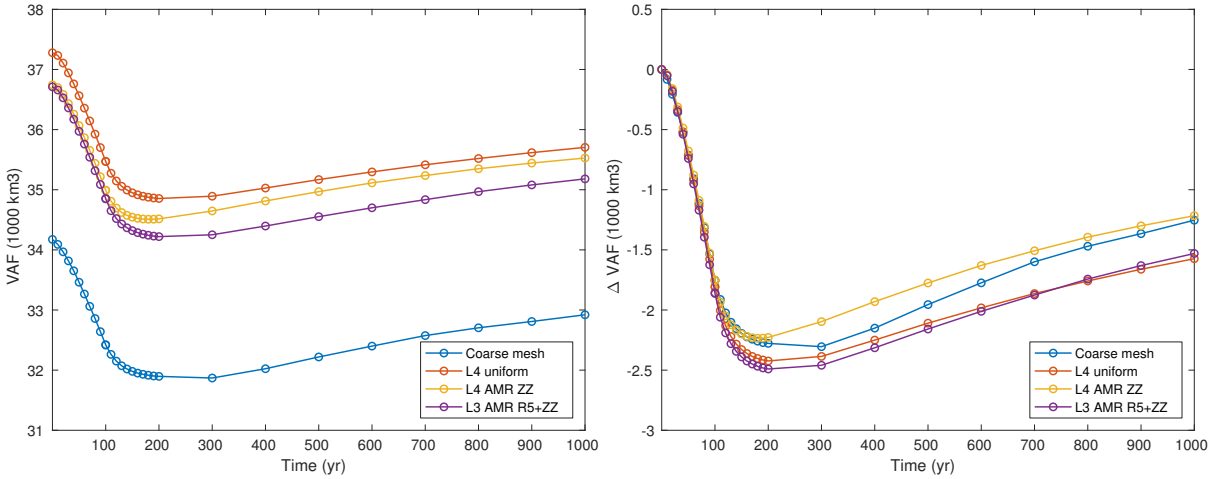

Figure 4.12: Volume above floatation (VAF) evolution along Ice1r and Ice1ra phases for different meshes: coarse mesh, adaptive meshes (L4 ZZ and L3 AMR R5+ZZ) and uniformly refined mesh (L4). The phases are described in Table 4.7. The criterion R5+ZZ means the combination of the ZZ error estimator (deviatoric stress) and element distance to the grounding line ($R_{gl} = 5\,km$, R5). The thresholds used for element/group in the ZZ criterion are, respectively, $\epsilon_{\tau,e}^{max} = 0.08\epsilon_{\tau}^{max}$ and $\epsilon_{\tau,g}^{max} = 0.008\epsilon_{\tau}^{max}$ for AMR ZZ, and $\epsilon_{\tau,e}^{max} = 0.16\epsilon_{\tau}^{max}$ and $\epsilon_{\tau,g}^{max} = 0.016\epsilon_{\tau}^{max}$ for AMR R5+ZZ, where ϵ_{τ}^{max} is the maximum error value observed in the coarse mesh. Mesher used: Bamg.

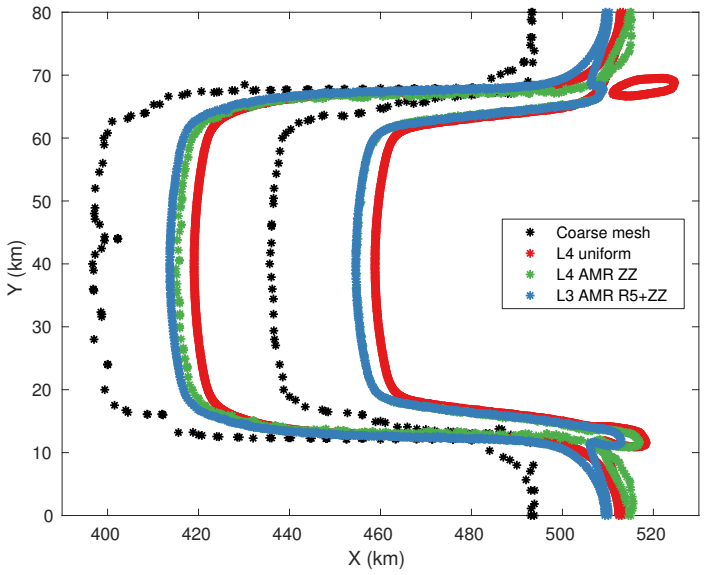

Figure 4.13: Grounding line positions at the beginning and end of the Ice1r phase for different meshes: coarse mesh, adaptive meshes (L4 AMR ZZ and L3 AMR R5+ZZ) and uniformly refined mesh (L4). The phase is described in Table 4.7. The description of the refinement criteria (AMR meshes) are summarized in the legend of Figure 4.12. Mesher used: Bamg.

4.4 Adaptive mesh refinement time performance

To analyze the AMR performance in terms of computational time, we run the experiment Ice1r of MISMIP+ [7]. The experiment starts from the steady state condition and runs forward in time for 100 yr with a basal melt rate applied. The time step is equal to 0.2 yr (computed to fulfill the CFL condition for the highest resolution mesh). The non-linear SSA equations are solved using the Picard scheme and the Multifrontal Massively Parallel sparse direct Solver, MUMPS [4, 5].

The purpose of the experiments described here is to assess the computational overhead when the mesh adaptivity is activated. We initialize all the models using the steady state solution obtained with the same adaptive mesh (level of refinement and criteria) used to carry out the Ice1r experiment. This procedure emulates a common modeling practice (e.g., [27, 89]): the initial conditions are self-consistent with the adaptive mesh, avoiding numerical artifacts during the transient simulation. All the experiments are run in parallel (16 cores) in a 2x Intel Xeon E5-2630 v3 2.40 GHz with 64 GB of RAM.

Table 4.10 presents grounding line positions obtained with different meshes at the end of Ice1r experiment, and the computational time and number of elements required for each mesh, as well as the criterion used. The levels of refinement are labeled as 'L#', e.g., L3 means level 3 (see Table 4.9). Considering the grounding line position obtained from the highest resolution mesh (L4 uniform) as a reference result, we compare the computational cost using uniform and adaptive meshes to obtain the same result within a deviation of 1.5%. In Table 4.10, only L3 uniform, L3 AMR R30, L3 AMR ZZ, and L3 AMR R5+ZZ meshes produce this required accuracy. AMR R30 mesh has at least 25% of the number of elements of the L3 uniform mesh, which represents virtually 80% of the computational time using the uniform mesh. In terms of refinement criteria, AMR ZZ generates 20% of the number of elements in comparison to AMR R30, which means virtually 25% of computational time. Comparing AMR ZZ and L3 uniform, the computational time using the adaptive mesh represents at least 25% of the computational time using the uniform mesh. The performance of Bamg and NeoPZ is similar, and the ratio of computational time and number of elements is virtually equal for both packages.

Figure 4.14 shows the element counts and the solution time for the adaptive meshes normalized against the values for the equivalent uniform meshes. In Figure 4.14, the solution time curve represents the relative savings due to mesh adaptivity, while the gap between the two curves (solution time minus element counts) illustrates the overhead due to the adaptive mesh procedure. We note the mesh adaptivity overhead decreases with the level of refinement and becomes reasonable for level 2 or higher.

Table 4.10: AMR time performance comparison for the Ice1r experiment, MISMIP+.

Level	CPU time (s)	Nb elem.	GL pos. (km)
L0 uniform	40	6,780	396.5
L1 uniform	188	27,706	407.0
L2 uniform	857	107,722	411.9
L3 uniform	1,705	473,446	416.0
L4 uniform	9,035	1,780,012	419.0
L3 AMR R5	498	33,794	405.2
L3 AMR R30	1,376	110,332	413.7
L3 AMR ZZ	369	21,088	415.7
L3 AMR R5+ZZ	807	56,267	413.7

Level = level of refinement. Nb elem. = number of elements.
GL pos. = grounding line position at the end of the Ice1r experiment,
MISMIP+. Mesher used: Bamg.
AMR R5+ZZ = combination of the criteria ZZ error estimator
(deviatoric stress tensor) and element distance to the GL ($R_{gl} = 5\,km$, R5).
The thresholds for element/group used in the ZZ criterion
are, respectively, $\epsilon_{\tau,e}^{max} = 0.16\epsilon_{\tau}^{max}$ and$\epsilon_{\tau,g}^{max} = 0.016\epsilon_{\tau}^{max}$ for AMR ZZ,
and $\epsilon_{\tau,e}^{max} = 0.48\epsilon_{\tau}^{max}$ and$\epsilon_{\tau,g}^{max} = 0.08\epsilon_{\tau}^{max}$ for AMR R5+ZZ,
where ϵ_{τ}^{max} is the maximum error value observed in the coarse mesh.

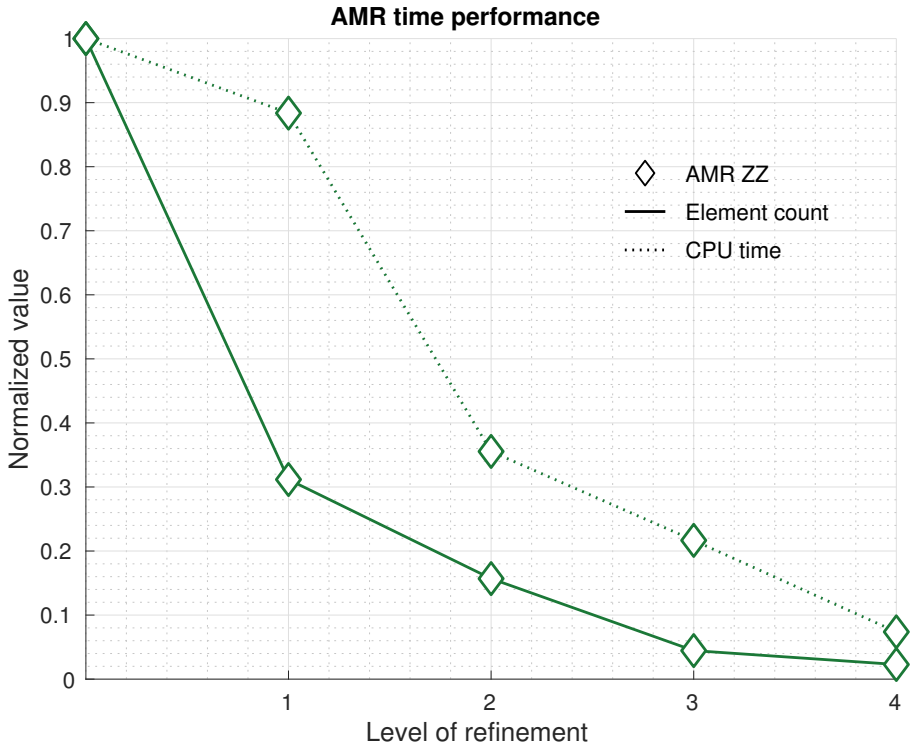

Figure 4.14: Number of elements and CPU time for adaptive meshes using the ZZ error estimator (AMR ZZ). The number of elements and CPU time are normalized by the respective values of the uniformly refined meshes. The normalized CPU time curve represents the mesh adaptivity savings, while the difference between the two curves represents the adaptive mesh procedure cost. Mesher used: Bamg. The thresholds for element/group used in the AMR ZZ are, respectively, $\epsilon_{\tau,e}^{max} = 0.64\epsilon_{\tau}^{max}$ and $\epsilon_{\tau,g}^{max} = 0.32\epsilon_{\tau}^{max}$ for L1, $\epsilon_{\tau,e}^{max} = 0.24\epsilon_{\tau}^{max}$ and $\epsilon_{\tau,g}^{max} = 0.08\epsilon_{\tau}^{max}$ for L2, $\epsilon_{\tau,e}^{max} = 0.16\epsilon_{\tau}^{max}$ and $\epsilon_{\tau,g}^{max} = 0.016\epsilon_{\tau}^{max}$ for L3, $\epsilon_{\tau,e}^{max} = 0.048\epsilon_{\tau}^{max}$ and $\epsilon_{\tau,g}^{max} = 0.0064\epsilon_{\tau}^{max}$ for L4, where ϵ_{τ}^{max} is the maximum error value observed in the coarse mesh.

4.5 Discussion: MISMIP3d and MISMIP+ results

In this work, we describe the implementation of an adaptive mesh refinement approach in the Ice Sheet System Model (ISSM) as well as the performance of our implementation in terms of accuracy of the simulated grounding line position and simulation time. We investigate the adaptive meshes performance using a heuristic criterion based on the distance to the grounding line [27, 39, 57, 62], and we compare with an error estimator (ZZ, [161]) based on the a posteriori analysis of the transient solutions (e.g., [27, 57, 62]).

We rely on two different mesh generators, Bamg [66] and NeoPZ [34], that have different properties. It is therefore expected that their solutions are not identical. This explains the difference observed in the grounding line positions compared to uniform meshes for the three sub-element parameterizations (e.g., the MISMIP3d setup, Figure 4.1).

NeoPZ generates nested meshes, which reduces errors in the interpolation step and is useful to assess mesh adaptivity performance in comparison to uniformly refined mesh. Bamg's algorithm works differently: the fact that some vertices' positions change produces at least two side effects: (1) induced errors in the interpolation process; (2) positive or negative impact on the convergence of the solutions. The weight of the first side effect can be reduced using higher element distance to the grounding line (R_{gl}), for which the highest resolution is applied, and increasing the length of the mesh transition zone between fine and coarse elements. Higher-order interpolative schemes can be also used, as pointed out by Goldberg and colleagues [57], to avoid solution diffusion. In ISSM, the interpolation scheme is carried out by $\mathscr{P}_0$ and $\mathscr{P}_1$ Lagrange polynomials, and we suspect these are enough for our adaptive mesh procedure. The weight of the second side effect depends on the problem considered. We suspect that for grounding line dynamics this effect has overall a positive impact, once updating vertex positions is somewhat similar to the moving mesh technique, although the grounding line is not explicitly defined in our approach as in other studies (e.g., [153]). This argument is based on the results shown here, for both MISMIP3d and MISMIP+ setups. Some mesh packages and finite element libraries related to NeoPZ are Deal II [13], Hermes [154], libMesh [87], and HP90 [32]. Mesh generators related to Bamg are MMG [29], Yams [46], and Gmsh [52]. Then, we expect that the results shown in this work would be reproduced with these related packages.

The results from MISMIP3d suggest that, independently of the sub-element parameterization and refinement level, refining elements within a 5 km region with highest resolution around the grounding line is enough to generate solutions (grounding line position and grounding line reversibility) similar to the ones produced by uniformly refined meshes. This holds for Bamg and NeoPZ (Figure 4.1). Cornford and colleagues [27] presented similar results for MISMIP3d using SSA equations through BISICLES, a finite-volume-based ice sheet model. Based on the MISMIP3d experiment, they concluded that refining four cells on either side of the grounding line was enough to achieve results similar to uniform meshes for all levels of refinement. Here, the grounding line reversibility is also achieved by applying the ZZ error estimator.

For MISMIP+, a minimal distance of 30 km for the highest resolution around the grounding line is necessary to accurately capture the grounding line position (Figure 4.9). Nevertheless, there is a residual between grounding line positions from adaptive and uniform meshes. This adaptive mesh dependency can be explained by the bed topography of MISMIP+ (Figure 4.6); the high gradient in the side walls induces numerical errors on the gradients of the velocity

field (deviatoric stress tensor, near the grounding zone) and ice thickness (on grounded ice), as illustrated by the spatial distribution of the a posteriori error estimator used here (Figure 4.10). For the MISMIP3d setup, the highest values of the error estimate concentrate only around the grounding line, which explains why a few kilometers of high resolution near the grounding line improve its position.

Figures 4.1 and 4.9 present a picture of the impact of mesh resolution in integrated quantities like the ice volume above floatation (VAF). The VAF curves follow the grounding line position behavior, presenting the same adaptive mesh dependency in the MISMIP+ setup. Therefore, the accuracy of VAF depends on the accuracy of the grounding line dynamics. Since VAF changes represent potential sea level rise, we highlight that the grounding line movement should be accurately tracked in ice sheet models. This is illustrated in Figures 4.11 and 4.12, where the evolution of the grounded area and VAF along the MISMIP+ experiments are shown, respectively. The amount of changes on these integrated quantities depends on the mesh resolution.

Since numerical errors are not only concentrated near the grounding line for the MISMIP+ setup, an error estimator is likely more appropriate to understand the error structure of the problem, to guide the refinement and to reduce the error estimates along the domain, improving AMR performance. This explains why a simple test with the AMR ZZ produces better convergence with much fewer elements than mesh adaptivity based on the heuristic criterion (element distance to the grounding line, Figure 4.9). Related works have used proxies of error estimators: Goldberg *et al.* (2009, [57]) used the jumps in strain rate between adjacent cells; Gudmundsson *et al.* (2012, [62]) used the second derivative of the ice thickness; Cornford *et al.* (2013, [27]) used the Laplacian of the velocity field, and Gillet-Chaulet *et al.* (2017, [53]) used the estimator proposed by Frey and Alauzet (2005, [47]), whose metric is based on a priori interpolation error calculated by the field's Hessian matrix (second derivative). The ZZ used here is a true a posteriori error estimator based on the recovered gradient [2], widely used in the finite element community [3, 60] and suitable to be implemented in ice sheet models, including those based on finite volumes or finite differences. As the MISMIP+ bed geometry is more realistic than MISMIP3d, we can expect similar results for real glaciers, i.e., high numerical errors present in regions not necessarily adjacent to the grounding line.

Further analysis with ZZ or another error estimator should be developed to improve the mesh adaptivity criterion used in ice sheet modeling. An important issue to be investigated is the interpolation of real bed topography directly from a dataset every time the mesh is adapted. This interpolation increases bed resolution according to mesh adaptation, which reduces the smoothness of the bed in the model (since real beds are not necessarily smooth). The reduction of the bed smoothness induces some numerical errors and counterbalances the effect of mesh adaptation, increasing adaptive mesh dependency. Real bed topographies should be analyzed in benchmark models as well as in real ice sheet domains. Our current adaptive mesh refinement implementation interpolates the bed elevation from the coarse mesh, except for the MISMIP+ experiment, for which we hard-coded the calculation of the bed topography directly in the code (in this case, the adaptive mesh approach reduces the smoothness of the bed in the model, but as there is no small-scale bed topography, the numerical error based on the ZZ error estimator for the ice thickness is reduced). The interpolation from a dataset will be implemented in ISSM in the future. Based on this discussion and the results shown in this study, we recommend adaptive

Table 4.11: AMR criteria comparison for MISMIP+ experiment.

Level	Criteria	GL pos. (km)	Nb elem.
L0	(coarse mesh)	435.6	6,780
L1	AMR ZZ	446.8	15,864
L1	AMR R5+ZZ	446.7	15,976
L1	Uniform	447.0	27,120
L2	AMR ZZ	452.6	20,891
L2	AMR R5+ZZ	452.2	22,692
L2	Uniform	451.9	108,480
L3	AMR ZZ	455.3	21,936
L3	AMR R5+ZZ	455.6	42,617
L3	Uniform	456.3	433,920
L4	AMR ZZ	455.8	24,428
L4	AMR R5+ZZ	455.4	192,149
L4	Uniform	459.0	1,735,680

Level = level of refinement. GL pos. = grounding line position at the end of the experiment. Nb elem. = number of elements. AMR R5+ZZ = combination of the criteria ZZ error estimator (deviatoric stress tensor) and element distance to the grounding line ($R_{gl} = 5\,km$, R5). Mesher used: NeoPZ. The thresholds used in the ZZ criterion are described in the legend of Figure 4.9.

mesh refinement with the combination of the heuristic criterion (using a minimal distance, e.g., 5 km) with an associated error estimator. Our recommendation is based on the following: we know a priori that applying high resolution around the grounding line would reduce the error caused by the basal friction discretization within the elements. In fact, applying only an error estimator does not guarantee that the elements around the grounding line are refined until the highest (desired) resolution. We noted this for the MISMIP+ setup (see the last mesh in Figure 4.8). On the other hand, only imposing fine mesh resolution near the grounding line does not ensure that the grounding line position is correctly captured because the extension of the grounding zone [136] depends on the physical parameters of the ice sheet. Interestingly, for the MISMIP+ setup, the combination of the heuristic criterion with the ZZ error estimator (AMR R5+ZZ) and the AMR ZZ produce similar results (as shown in Table 4.11), which does not guarantee that it would be the case for real ice sheets. Therefore, for real ice sheets, we suspect that using both criteria (R5+ZZ) should work properly (also, see Figure 4.12; R5+ZZ generates ΔVAF evolution similar to ones produced by the most refined mesh, L4 uniform). Tests varying AMR parameters (distance to the grounding line, maximum thresholds for the error estimator, level of refinement, etc.) should be carried before any ice sheet simulation to optimize the mesh adaptivity performance in terms of both solutions and computational time.

The grounding zone is not the only place where adaptive meshes can be applied. Ice front and calving dynamics [149] as well as shear margins in ice streams [64] are examples for which adaptive meshes can improve numerical solutions with reduced computational efforts. In ISSM,

the mesh adaptivity can be applied to these regions through extension of Algorithm 2. Other experiments testing the adaptive mesh approach to refine in the ice front region show promising results [132].

Our mesh adaptivity performance analysis shows that the computational time in adaptive mesh refinement simulations reaches up to 1 order of magnitude less in comparison to models based on uniformly refined meshes. Computational time and solution accuracy of mesh adaptivity depend on the physical problem and the refinement criterion used. In this work, even with hundreds of elements generated (e.g., meshes AMR R30), the computational time is satisfactory. This is observed for both NeoPZ and Bamg. Further analysis should be carried out to check the performance in real ice sheets and in higher computational scale (thousand of elements), but the results presented in this study suggest that our adaptive mesh refinement implementation strategy is adapted to the modeling questions being investigated. Our mesh adaptivity computation time compares to Cornford *et al.* (2013, [27]), in which adaptive mesh refinement simulations spent approximately one-third of CPU time needed in simulations performed by uniformly refined meshes.

Chapter 5

Conclusions and future works

We implemented dynamic mesh adaptivity into ISSM and tested its performance on two different experiments with different refinement criteria. The comparison between Bamg and NeoPZ shows that they present similar performance, and the choice of which to be used is up to the user. Moreover, users using Bamg (or similar mesh generator) should pay attention in the minimal extension of the mesh transition zone to reduce numerical errors (e.g., in the interpolation step). NeoPZ (or similar package) is more suitable with error estimators, since the refinement of elements with high numerical errors is straightforward. Besides that, there is no error during the interpolation step. Based on the adaptive mesh sensitivity observed here, we conclude that mesh adaptivity in marine ice sheet simulation without an error estimator should be avoided, mainly in setups where bedrock induces complex stress distributions and/or strong buttressing. In real bedrock topographies, where small scale features may play an important role, an error estimator is suitable to guide the adaptive mesh refinement. Further research should be carried out in order to evaluate mesh adaptivity performance in real bed geometries. Our recommendation to improve the adaptive mesh refinement performance while minimizing computational effort is the combination of the heuristic criteria, applying a minimal distance around the grounding line (e.g., 5 km), with an error estimator. The numerical experiments performed with the ZZ error estimator show a significant potential, mostly due to its simple implementation and performance. The mesh adaptivity technique in ISSM can be extended to others physical processes such that the evolution of marine ice sheets and, consequently the sea level rise, can be accurately modeled and projected.

As future works and extensions of this thesis, we write :

1. Numerical modeling of real marine ice sheets (e.g., WAIS) using adaptive meshes;
2. Application of adaptive mesh refinement to other places, like ice front dynamics, ice stream margins, hydrology, etc;
3. Extension of adaptive mesh refinement to 3D meshes, enabling the use of high order approximations;
4. Further analysis of the ZZ error estimator in real bedrock topographies and real ice sheets.

Bibliography

[1] M. Ainsworth and J. T. Oden. A posteriori error estimation in finite element analysis. *Computer Methods in Applied Mechanics and Engineering*, 142(1):1–88, 1997.

[2] M. Ainsworth and J. T. Oden. *A Posterori Error Estimation in Finite Element Analysis*. Pure and Applied Mathematics: A Wiley Series of Texts, Monographs and Tracts. Wiley-Interscience, New York, NY, USA, 1st edition, 2000.

[3] M. Ainsworth, J. Z. Zhu, A. W. Craig, and O. C. Zienkiewicz. Analysis of the Zienkiewicz–Zhu a-posteriori error estimator in the finite element method. *International Journal for Numerical Methods in Engineering*, 28(9):2161–2174, 1989.

[4] P. R. Amestoy, I. S. Duff, J.-Y. L'Excellent, and J. Koster. A fully asynchronous multifrontal solver using distributed dynamic scheduling. *SIAM Journal on Matrix Analysis and Applications*, 23(1):15–41, 2001.

[5] P. R. Amestoy, A. Guermouche, J.-Y. L'Excellent, and S. Pralet. Hybrid scheduling for the parallel solution of linear systems. *Parallel Computing*, 32(2):136–156, 2006. Parallel Matrix Algorithms and Applications (PMAA'04).

[6] D. A. Anderson, J. C. Tannehill, and R. H. Pletcher. *Computational Fluid Mechanics and Heat Transfer*. Series in computational methods in mechanics and thermal sciences. McGraw-Hill Book Company, USA, 1984.

[7] X. S. Asay-Davis, S. L. Cornford, G. Durand, B. K. Galton-Fenzi, R. M. Gladstone, G. H. Gudmundsson, T. Hattermann, D. M. Holland, D. Holland, P. R. Holland, D. F. Martin, P. Mathiot, F. Pattyn, and H. Seroussi. Experimental design for three interrelated marine ice sheet and ocean model intercomparison projects: MISMIP v. 3 (MISMIP+), ISOMIP v. 2 (ISOMIP+) and MISOMIP v. 1 (MISOMIP1). *Geoscientific Model Development*, 9(7):2471–2497, 2016.

[8] I. Babuška and W. C. Rheinboldt. A-posteriori error estimates for the finite element method. *International Journal for Numerical Methods in Engineering*, 12(10):1597–1615, 1978.

[9] I. Babuška and W. C. Rheinboldt. Adaptive approaches and reliability estimations in finite element analysis. *Computer Methods in Applied Mechanics and Engineering*, 17-18:519–540, 1979.

[10] S. Balay, S. Abhyankar, M. F. Adams, J. Brown, P. Brune, K. Buschelman, L. Dalcin, A. Dener, V. Eijkhout, W. D. Gropp, D. Kaushik, M. G. Knepley, D. A. May, L. C. McInnes, R. T. Mills, T. Munson, K. Rupp, P. Sanan, B. F. Smith, S. Zampini, H. Zhang, and H. Zhang. PETSc Web page. `http://www.mcs.anl.gov/petsc`, 2018.

[11] S. Balay, W. D. Gropp, L. C. McInnes, and B. F. Smith. Efficient management of parallelism in object oriented numerical software libraries. In E. Arge, A. M. Bruaset, and H. P. Langtangen, editors, *Modern Software Tools in Scientific Computing*, pages 163–202. Birkhäuser Press, 1997.

[12] J. L. Bamber, R. E. M. Riva, B. L. A. Vermeersen, and A. M. LeBrocq. Reassessment of the potential sea-level rise from a collapse of the West Antarctic Ice Sheet. *Science*, 324(5929):901–903, 2009.

[13] W. Bangerth, R. Hartmann, and G. Kanschat. deal.II - a general-purpose object-oriented finite element library. *ACM Trans. Math. Softw.*, 33(4), August 2007.

[14] H. H. C. Barboza, A. L. Bortoli, J. C. Simões, R. D. Cunha, and M. Braun. Bidimensional numerical simulation of the Lange Glacier, King George Island, Antarctica. *Pesquisa Antártica Brasileira*, 4:67–76, 2004.

[15] M. J. Berger and P. Colella. Local adaptive mesh refinement for shock hydrodynamics. *Journal of Computational Physics*, 82(1):64–84, 1989.

[16] E. Berthier, T. A. Scambos, and C. A. Shuman. Mass loss of Larsen B tributary glaciers (Antarctic Peninsula) unabated since 2002. *Geophysical Research Letters*, 39(13):1–6, 2012.

[17] R. A. Bindschadler, S. Nowicki, A. Abe-Ouchi, A. Aschwanden, H. Choi, J. Fastook, G. Granzow, R. Greve, G. Gutowski, U. Herzfeld, C. Jackson, J. Johnson, C. Khroulev, A. Levermann, W. H. Lipscomb, M. A. Martin, M. Morlighem, B. R. Parizek, D. Pollard, S. F. Price, D. Ren, F. Saito, T. Sato, H. Seddik, H. Seroussi, K. Takahashi, R. Walker, and W. L. Wang. Ice-sheet model sensitivities to environmental forcing and their use in projecting future sea level (the SeaRISE project). *Journal of Glaciology*, 59(214):195–224, 2013.

[18] H. Blatter. Velocity and stress-fields in grounded glaciers: A simple algorithm for including deviatoric stress gradients. *Journal of Glaciology*, 41(138):333–344, 1995.

[19] J. H. Bondzio, H. Seroussi, M. Morlighem, T. Kleiner, M. Rückamp, A. Humbert, and E. Y. Larour. Modelling calving front dynamics using a level-set method: application to Jakobshavn Isbræ, West Greenland. *The Cryosphere*, 10(2):497–510, 2016.

[20] J. Brondex, O. Gagliardini, F. Gillet-Chaulet, and G. Durand. Sensitivity of grounding line dynamics to the choice of the friction law. *Journal of Glaciology*, 63(241):854–866, 2017.

[21] W. F. Budd, P. L. Keage, and N. A. Blundy. Empirical studies of ice sliding. *Journal of Glaciology*, 23(89):157–170, 1979.

[22] J. L. D. Calle, P. R. B. Devloo, and S. M. Gomes. Implementation of continuous hp-adaptive finite element spaces without limitations on hanging sides and distribution of approximation orders. *Computers & Mathematics with Applications*, 70(5):1051–1069, 2015.

[23] V. A. Chugunov and A. V. Wilchinsky. Modelling of a marine glacier and ice-sheet-ice-shelf transition zone based on asymptotic analysis. *Annals of Glaciology*, 23:59–67, 1996.

[24] J. A. Church, P. U. Clark, A. Cazenave, J. M. Gregory, S. Jevrejeva, A. Levermann, M. A. Merrifield, G. A. Milne, R. S. Nerem, P. D. Nunn, A. J. Payne, W. T. Pfeffer, D. Stammer, and A. S. Unnikrishnan. Sea Level Change. In T. F. Stocker, D. Qin, G.-K. Plattner, M. Tignor, S. K. Allen, J. Boschung, A. Nauels, Y. Xia, V. Bex, and P. M. Midgley, editors, *Climate Change 2013: The Physical Science Basis. Contribution of Working Group I to the Fifth Assessment Report of the Intergovernmental Panel on Climate Change*, pages 1137–1216. Cambridge University Press, Cambridge, United Kingdom and New York, NY, USA, 2013.

[25] G. K. C. Clarke. Subglacial processes. *Annual Review of Earth and Planetary Sciences*, 33(1):247–276, 2005.

[26] J. Cohen, J. A. Screen, J. C. Furtado, M. Barlow, D. Whittleston, D. Coumou, J. Francis, K. Dethloff, D. Entekhabi, J. Overland, and J. Jones. Recent Arctic amplification and extreme mid-latitude weather. *Nature Geoscience*, 7:627–637, 2014.

[27] S. L. Cornford, D. F. Martin, D. T. Graves, D. F. Ranken, A. M. Le Brocq, R. M. Gladstone, A. J. Payne, E. G. Ng, and W. H. Lipscomb. Adaptive mesh, finite volume modeling of marine ice sheets. *Journal of Computational Physics*, 232(1):529 – 549, 2013.

[28] K. Cuffey and W. S. B. Paterson. *The Physics of Glaciers*. Elsevier, Oxford, 4th edition, 2010.

[29] C. Dapogny, C. Dobrzynski, and P. Frey. Three-dimensional adaptive domain remeshing, implicit domain meshing, and applications to free and moving boundary problems. *Journal of Computational Physics*, 262:358–378, 2014.

[30] B. J. Davies, N. R. Golledge, N. F. Glasser, J. L. Carrivick, S. R. M. Ligtenberg, N. E. Barrand, M. R. van den Broeke, M. J. Hambrey, and J. L. Smellie. Modelled glacier response to centennial temperature and precipitation trends on the Antarctic Peninsula. *Nature Climate Change*, 4:993–998, 2014.

[31] R. M. DeConto and D. Pollard. Contribution of Antarctica to past and future sea-level rise. *Nature*, 531:591–597, 2016.

[32] L. Demkowicz, K. Gerdes, C. Schwab, A. Bajer, and T. Walsh. HP90: A general and flexible Fortran 90 hp-FE code. *Computing and Visualization in Science*, 1(3):145–163, 1998.

[33] P. Devloo, J. T. Oden, and T. Strouboulis. Implementation of an adaptive refinement technique for the SUPG algorithm. *Computer Methods in Applied Mechanics and Engineering*, 61(3):339–358, 1987.

[34] P. R. B. Devloo. PZ: An object oriented environment for scientific programming. *Computer Methods in Applied Mechanics and Engineering*, 150(1):133–153, 1997. Symposium on Advances in Computational Mechanics.

[35] T. S. Dotto, R. Kerr, M. M. Mata, M. Azaneu, I. Wainer, E. Fahrbach, and G. Rohardt. Assessment of the structure and variability of Weddell Sea water masses in distinct ocean reanalysis products. *Ocean Science*, 10(3):523–546, 2014.

[36] T. K. Dupont and R. B. Alley. Assessment of the importance of ice-shelf buttressing to ice-sheet flow. *Geophysical Research Letters*, 32(4), 2005.

[37] G. Durand, O. Gagliardini, B. de Fleurian, T. Zwinger, and E. Le Meur. Marine ice sheet dynamics: Hysteresis and neutral equilibrium. *Journal of Geophysical Research: Earth Surface*, 114(F3):1–10, 2009.

[38] G. Durand, O. Gagliardini, L. Favier, T. Zwinger, and E. Le Meur. Impact of bedrock description on modeling ice sheet dynamics. *Geophysical Research Letters*, 38(20):1–6, 2011.

[39] G. Durand, O. Gagliardini, T. Zwinger, E. Le Meur, and R. C. A. Hindmarsh. Full stokes modeling of marine ice sheets: influence of the grid size. *Annals of Glaciology*, 50(52):109–114, 2009.

[40] P. Dutrieux, J. De Rydt, A. Jenkins, P. R. Holland, H. K. Ha, S. H. Lee, E. J. Steig, Q. Ding, E. P. Abrahamsen, and M. Schröder. Strong sensitivity of Pine Island Ice-Shelf melting to climatic variability. *Science*, 343(6167):174–178, 2014.

[41] L. Favier, G. Durand, S. L. Cornford, G. H. Gudmundsson, O. Gagliardini, F. Gillet-Chaulet, T. Zwinger, A. J. Payne, and A. M. Le Brocq. Retreat of Pine Island Glacier controlled by marine ice-sheet instability. *Nature Climate Change*, 4:117–121, 2014.

[42] L. Favier, O. Gagliardini, G. Durand, and T. Zwinger. A three-dimensional full stokes model of the grounding line dynamics: effect of a pinning point beneath the ice shelf. *The Cryosphere*, 6(1):101–112, 2012.

[43] J. Feldmann and A. Levermann. Collapse of the West Antarctic Ice Sheet after local destabilization of the Amundsen Basin. *Proceedings of the National Academy of Sciences*, 112(46):14191–14196, 2015.

[44] A. Fowler. *Mathematical Geoscience*. Interdisciplinary Applied Mathematics. Springer-Verlag London, Berlin, Germany, 1th edition, 2011.

[45] P. Fretwell, H. D. Pritchard, D. G. Vaughan, J. L. Bamber, N. E. Barrand, R. Bell, C. Bianchi, R. G. Bingham, D. D. Blankenship, G. Casassa, G. Catania, D. Callens, H. Conway, A. J. Cook, H. F. J. Corr, D. Damaske, V. Damm, F. Ferraccioli, R. Forsberg,

S. Fujita, Y. Gim, P. Gogineni, J. A. Griggs, R. C. A. Hindmarsh, P. Holmlund, J. W. Holt, R. W. Jacobel, A. Jenkins, W. Jokat, T. Jordan, E. C. King, J. Kohler, W. Krabill, M. Riger-Kusk, K. A. Langley, G. Leitchenkov, C. Leuschen, B. P. Luyendyk, K. Matsuoka, J. Mouginot, F. O. Nitsche, Y. Nogi, O. A. Nost, S. V. Popov, E. Rignot, D. M. Rippin, A. Rivera, J. Roberts, N. Ross, M. J. Siegert, A. M. Smith, D. Steinhage, M. Studinger, B. Sun, B. K. Tinto, B. C. Welch, D. Wilson, D. A. Young, C. Xiangbin, and A. Zirizzotti. Bedmap2: improved ice bed, surface and thickness datasets for Antarctica. *The Cryosphere*, 7(1):375–393, 2013.

[46] P. Frey. Yams a fully automatic adaptive isotropic surface remeshing procedure. Technical report, INRIA, 11 2001.

[47] P. J. Frey and F. Alauzet. Anisotropic mesh adaptation for CFD computations. *Computer Methods in Applied Mechanics and Engineering*, 194(48):5068–5082, 2005. Unstructured Mesh Generation.

[48] Chad A. G., D. E. Gwyther, and D. D. Blankenship. Antarctic mapping tools for Matlab. *Computers & Geosciences*, 104:151–157, 2017.

[49] O. Gagliardini, J. Brondex, F. Gillet-Chaulet, L. Tavard, V. Peyaud, and G. Durand. Brief communication: Impact of mesh resolution for MISMIP and MISMIP3d experiments using Elmer/Ice . *The Cryosphere*, 10(1):307–312, 2016.

[50] O. Gagliardini, D. Cohen, P. Råback, and T. Zwinger. Finite-element modeling of subglacial cavities and related friction law. *Journal of Geophysical Research: Earth Surface*, 112(F2):1–11, 2007.

[51] O. Gagliardini, T. Zwinger, F. Gillet-Chaulet, G. Durand, L. Favier, B. de Fleurian, R. Greve, M. Malinen, C. Martín, P. Råback, J. Ruokolainen, M. Sacchettini, M. Schäfer, H. Seddik, and J. Thies. Capabilities and performance of Elmer/Ice, a new-generation ice sheet model. *Geoscientific Model Development*, 6(4):1299–1318, 2013.

[52] C. Geuzaine and J.-F. Remacle. Gmsh: A 3-D finite element mesh generator with built-in pre- and post-processing facilities. *International Journal for Numerical Methods in Engineering*, 79(11):1309–1331, 2009.

[53] F. Gillet-Chaulet, L. Tavard, N. Merino, V. Peyaud, J. Brondex, G. Durand, and O. Gagliardini. Anisotropic mesh adaptation for marine ice-sheet modelling. In *EGU General Assembly 2017*, volume 19. Geophysical Research Abstracts, Vienna, Austria, 2017.

[54] R. M. Gladstone, V. Lee, A. Vieli, and A. J. Payne. Grounding line migration in an adaptive mesh ice sheet model. *Journal of Geophysical Research: Earth Surface*, 115(F4):1–19, 2010.

[55] R. M. Gladstone, R. C. Warner, B. K. Galton-Fenzi, O. Gagliardini, T. Zwinger, and R. Greve. Marine ice sheet model performance depends on basal sliding physics and sub-shelf melting. *The Cryosphere*, 11(1):319–329, 2017.

[56] J. W. Glen. The creep of polycrystalline ice. *Proceedings of the Royal Society of London A: Mathematical, Physical and Engineering Sciences*, 228(1175):519–538, 1955.

[57] D. Goldberg, D. M. Holland, and C. Schoof. Grounding line movement and ice shelf buttressing in marine ice sheets. *Journal of Geophysical Research: Earth Surface*, 114(F4):1–23, 2009.

[58] N. R. Golledge, D. E. Kowalewski, T. R. Naish, R. H. Levy, C. J. Fogwill, and E. G. W. Gasson. The multi-millennial antarctic commitment to future sea-level rise. *Nature*, 526:421–438, 2015.

[59] G. H. Golub and C. F. Van Loan. *Matrix Computations*. The Johns Hopkins University Press, Baltimore, MD, USA, 3rd edition, 1996.

[60] T. Grätsch and K.-J. Bathe. A posteriori error estimation techniques in practical finite element analysis. *Computers & Structures*, 83(4):235–265, 2005.

[61] R. Greve and H. Blatter. *Dynamics of Ice Sheets and Glaciers*. Advances in Geophysical and Environmental Mechanics and Mathematics. Springer-Verlag Berlin Heidelberg, Berlin, Germany, 1th edition, 2009.

[62] G. H. Gudmundsson, J. Krug, G. Durand, L. Favier, and O. Gagliardini. The stability of grounding lines on retrograde slopes. *The Cryosphere*, 6(6):1497–1505, 2012.

[63] S. Hallegatte, C. Green, R. J. Nicholls, and J. Corfee-Morlot. Future flood losses in major coastal cities. *Nature Climate Change*, 3:802–806, 2013.

[64] M. Haseloff, C. Schoof, and O. Gagliardini. A boundary layer model for ice stream margins. *Journal of Fluid Mechanics*, 781:353–387, 2015.

[65] F. Hecht. A few snags in mesh adaptation loops. In B. W. Hanks, editor, *Proceedings of the 14th International Meshing Roundtable*, pages 301–311. Springer-Verlag Berlin Heidelberg, Germany, 2005.

[66] F. Hecht. BAMG: Bidimensional Anisotropic Mesh Generator. Technical report, FreeFem++, 12 2006.

[67] K. Herterich. On the flow within the transition zone between ice sheet and ice shelf. In C. J. van der Veen and J. Oerlemans, editors, *Dynamics of the West Antarctic Ice Sheet*, volume 4 of *Glaciology and Quaternary Geology*, pages 185–202. Springer, Dordrecht, The Netherlands, 1987.

[68] R. C. A. Hindmarsh. Qualitative dynamics of marine ice sheets. In W. R. Peltier, editor, *Ice in the Climate System*, pages 67–99, Berlin, Heidelberg, 1993. Springer Berlin Heidelberg.

[69] J. Hinkel, D. Lincke, A. T. Vafeidis, M. Perrette, R. J. Nicholls, R. S. J. Tol, X. Marzeion, B.and Fettweis, C. Ionescu, and A. Levermann. Coastal flood damage and adaptation costs under 21st century sea-level rise. *Proceedings of the National Academy of Sciences*, 111(9):3292–3297, 2014.

[70] J. Hoffman, J. Jansson, R. V. de Abreu, N. C. Degirmenci, N. Jansson, K. Müller, M. Nazarov, and J. H. Spühler. Unicorn: Parallel adaptive finite element simulation of turbulent flow and fluid–structure interaction for deforming domains and complex geometry. *Computers & Fluids*, 80:310–319, 2013. Selected contributions of the 23rd International Conference on Parallel Fluid Dynamics ParCFD2011.

[71] P. F. Hoffman, D. S. Abbot, Y. Ashkenazy, D. I. Benn, J. J. Brocks, P. A. Cohen, G. M. Cox, J. R. Creveling, Y. Donnadieu, D. H. Erwin, I. J. Fairchild, D. Ferreira, J. C. Goodman, G. P. Halverson, M. F. Jansen, G. Le Hir, G. D. Love, F. A. Macdonald, A. C. Maloof, C. A. Partin, G. Ramstein, B. E. J. Rose, C. V. Rose, P. M. Sadler, E. Tziperman, A. Voigt, and S. G. Warren. Snowball Earth climate dynamics and Cryogenian geology-geobiology. *Science Advances*, 3(11), 2017.

[72] J. W. Holt, D. D. Blankenship, D. L. Morse, D. A. Young, M. E. Peters, S. D. Kempf, T. G. Richter, D. G. Vaughan, and H. F. J. Corr. New boundary conditions for the West Antarctic Ice Sheet: Subglacial topography of the Thwaites and Smith glacier catchments. *Geophysical Research Letters*, 33(9), 2006.

[73] R. L. Hooke. *Principles of Glacier Mechanics*. Cambridge University Press, New York, NY, USA, 2nd edition, 2005.

[74] K. Hutter. *Theorical Glaciology*. Mathematical Approaches to Geophysics. D. Reidel Publishing Company, Dordrecht, The Netherlands, 1983.

[75] P. Huybrechts. A 3-d model for the Antarctic Ice Sheet: a sensitivity study on the glacial-interglacial contrast. *Climate Dynamics*, 5(2):79–92, 1990.

[76] P. Huybrechts. *The Antarctic Ice Sheet and environmental change: a three-dimensional modelling study*. PhD thesis, Vrije Universiteit of Brussel, 1992.

[77] A. Iken. The effect of the subglacial water pressure on the sliding velocity of a glacier in an idealized numerical model. *Journal of Glaciology*, 27(97):407–421, 1981.

[78] S. S. Jacobs, A. Jenkins, C. F. Giulivi, and P. Dutrieux. Stronger ocean circulation and increased melting under Pine Island Glacier ice shelf. *Nature Geoscience*, 4:519–523, 2011.

[79] S. Jevrejeva, A. Grinsted, and J. C. Moore. Upper limit for sea level projections by 2100. *Environmental Research Letters*, 9(10):104008, 2014.

[80] L. M. Jong, R. M. Gladstone, B. K. Galton-Fenzi, and M. A. King. Simulated dynamic regrounding during marine ice sheet retreat. *The Cryosphere*, 12(7):2425–2436, 2018.

[81] G. Jouvet and C. Gräser. An adaptive Newton multigrid method for a model of marine ice sheets. *Journal of Computational Physics*, 252:419 – 437, 2013.

[82] G. Karypis and V. Kumar. A fast and high quality multilevel scheme for partitioning irregular graphs. *SIAM Journal on Scientific Computing*, 20(1):359–392, 1998.

[83] M. C. Kennicutt, S. L. Chown, J. J. Cassano, D. Liggett, L. S. Peck, R. Massom, S. R. Rintoul, J. Storey, D. G. Vaughan, T. J. Wilson, and et al. A roadmap for Antarctic and Southern Ocean science for the next two decades and beyond. *Antarctic Science*, 27(1):3–18, 2015.

[84] S. A. Khan, K. H. Kjær, M. Bevis, J. L. Bamber, J. Wahr, K. K. Kjeldsen, A. A. Bjørk, N. J. Korsgaard, L. A. Stearns, M. R. van den Broeke, L. Liu, N. K. Larsen, and I. S. Muresan. Sustained mass loss of the northeast Greenland ice sheet triggered by regional warming. *Nature Climate Change*, 4:292–299.

[85] A. Khazendar, C. P. Borstad, B. Scheuchl, E. Rignot, and H. Seroussi. The evolving instability of the remnant Larsen B Ice Shelf and its tributary glaciers. *Earth and Planetary Science Letters*, 419:199 – 210, 2015.

[86] S. Kimura, A. Jenkins, P. Dutrieux, A. Forryan, A. C. Naveira Garabato, and Y. Firing. Ocean mixing beneath Pine Island Glacier ice shelf, West Antarctica. *Journal of Geophysical Research: Oceans*, 121(12):8496–8510, 2016.

[87] B. S. Kirk, J. W. Peterson, R. H. Stogner, and G. F. Carey. libMesh : a C++ library for parallel adaptive mesh refinement/coarsening simulations. *Engineering with Computers*, 22(3-4):237–254, 2006.

[88] E. Larour, H. Seroussi, M. Morlighem, and E. Rignot. Continental scale, high order, high spatial resolution, ice sheet modeling using the Ice Sheet System Model (ISSM). *Journal of Geophysical Research: Earth Surface*, 117(F1):1–20, 2012.

[89] V. Lee, S. L. Cornford, and A. J. Payne. Initialization of an ice-sheet model for present-day Greenland. *Annals of Glaciology*, 56(70):129–140, 2015.

[90] G. R. Leguy, X. S. Asay-Davis, and W. H. Lipscomb. Parameterization of basal friction near grounding lines in a one-dimensional ice sheet model. *The Cryosphere*, 8(4):1239–1259, 2014.

[91] P. Lemke, J. Ren, R. B. Alley, I. Allison, J. Carrasco, G. Flato, Y. Fujii, G. Kaser, P. Mote, R. H. Thomas, and T. Zhang. Observations: Changes in snow, ice and frozen ground. In S. Solomon, D. Qin, M. Manning, Z. Chen, M. Marquis, K. B. Averyt, M. Tignor, and H. L. Miller, editors, *Climate Change 2007: The Physical Science Basis. Contribution of Working Group I to the Fourth Assessment Report of the Intergovernmental Panel on Climate Change*, pages 337–384. Cambridge University Press, Cambridge, United Kingdom and New York, NY, USA, 2007.

[92] R. Lestringant. A two-dimensional finite-element study of flow in the transition zone between an ice sheet and an ice shelf. *Annals of Glaciology*, 20:67–72, 1994.

[93] M. Lichter, A. T. Vafeidis, R. J. Nicholls, and G. Kaiser. Exploring data-related uncertainties in analyses of land area and population in the "Low-Elevation Coastal Zone" (LECZ). *Journal of Coastal Research*, 27(4):757–768, 2011.

[94] D. MacAyeal. Large-scale ice flow over a viscous basal sediment: Theory and application to ice stream b, antarctica. *Journal of Geophysical Research: Solid Earth*, 94(B4):4071–4087, 1989.

[95] P. A. Mayewski, K. A. Maasch, D. Dixon, S. B. Sneed, R. Oglesby, E. Korotkikh, M. Potocki, B. Grigholm, K. Kreutz, A. V. Kurbatov, N. Spaulding, J. C. Stager, K. C. Taylor, E. J. Steig, J. White, N. A. N. Bertler, I. Goodwin, J. C. Simões, R. Jaña, S. Kraus, and J. Fastook. West Antarctica's sensitivity to natural and human-forced climate change over the holocene. *Journal of Quaternary Science*, 28(1):40–48, 2012.

[96] J. H. Mercer. West Antarctic Ice Sheet and CO2 greenhouse effect: a threat of disaster. *Nature*, 271:321–325, 1978.

[97] C. R. Meyer, A. S. Downey, and A. W. Rempel. Freeze-on limits bed strength beneath sliding glaciers. *Nature Communications*, 9(3242), 2018.

[98] D. H. Michael. The separation of a viscous liquid at a straight edge. *Mathematika*, 5(1):82–84, 1958.

[99] L. W. Morland. Thermomechanical balances of ice sheet flows. *Geophysical & Astrophysical Fluid Dynamics*, 29:237–266, 1984.

[100] L. W. Morland. Unconfined ice shelf flow. In C.J. van der Veen and J. Oerlemans, editors, *Dynamics of the West Antarctic Ice Sheet*, volume 4 of *Glaciology and Quaternary Geology*, pages 99–116. Springer, Dordrecht, The Netherlands, 1987.

[101] M. Morlighem. *Ice sheet properties inferred by combining numerical modeling and remote sensing data*. PhD thesis, Ecole Centrale Paris, 2011. https://tel.archives-ouvertes.fr/tel-00697004.

[102] M. Morlighem, E. Rignot, H. Seroussi, E. Larour, H. Ben Dhia, and D. Aubry. Spatial patterns of basal drag inferred using control methods from a full-stokes and simpler models for Pine Island Glacier, West Antarctica. *Geophysical Research Letters*, 37(14):1–6, 2010.

[103] M. Morlighem, H. Seroussi, E. Larour, and E. Rignot. Inversion of basal friction in Antarctica using exact and incomplete adjoints of a higher-order model. *Journal of Geophysical Research: Earth Surface*, 118(3):1746–1753, 2013.

[104] J. Mouginot, E. Rignot, and B. Scheuchl. Sustained increase in ice discharge from the Amundsen Sea Embayment, West Antarctica, from 1973 to 2013. *Geophysical Research Letters*, 41(5):1576–1584, 2014.

[105] I. Muszynski and G. E. Birchfield. A coupled marine ice-stream – ice-shelf model. *Journal of Glaciology*, 33(113):3–15, 1987.

[106] I. J. Nias, S. L. Cornford, and A. J. Payne. New mass-conserving bedrock topography for Pine Island Glacier impacts simulated decadal rates of mass loss. *Geophysical Research Letters*, 45(7):3173–3181, 2018.

[107] R. J. Nicholls, S. E. Hanson, J. A. Lowe, R. A. Warrick, X. Lu, and A. J. Long. Sea-level scenarios for evaluating coastal impacts. *Wiley Interdisciplinary Reviews: Climate Change*, 5(1):129–150, 2014.

[108] S. Nowicki, R. A. Bindschadler, A. Abe-Ouchi, A. Aschwanden, E. Bueler, H. Choi, J. Fastook, G. Granzow, R. Greve, G. Gutowski, U. Herzfeld, C. Jackson, J. Johnson, C. Khroulev, E. Larour, A. Levermann, W. H. Lipscomb, M. A. Martin, M. Morlighem, B. R. Parizek, D. Pollard, S. F. Price, D. Ren, E. Rignot, F. Saito, T. Sato, H. Seddik, H. Seroussi, K. Takahashi, R. Walker, and W. L. Wang. Insights into spatial sensitivities of ice mass response to environmental change from the SeaRISE ice sheet modeling project i: Antarctica. *Journal of Geophysical Research: Earth Surface*, 118(2):1002–1024, 2013.

[109] S. M. J. Nowicki and D. J. Wingham. Conditions for a steady ice sheet–ice shelf junction. *Earth and Planetary Science Letters*, 265(1):246–255, 2008.

[110] J. F. Nye. The distribution of stress and velocity in glaciers and ice-sheets. *Proceedings of the Royal Society of London A: Mathematical, Physical and Engineering Sciences*, 239(1216):113–133, 1957.

[111] J. T. Oden, G. F. Carey, and E. B. Becker. *Finite Elements*, volume 1. Prentice-Hall, Englewood, NJ, USA, 1981.

[112] J. T. Oden, T. Strouboulis, and P. Devloo. Adaptive finite element methods for the analysis of inviscid compressible flow: Part i. fast refinement/unrefinement and moving mesh methods for unstructured meshes. *Computer Methods in Applied Mechanics and Engineering*, 59(3):327–362, 1986.

[113] S. Osher and J. A. Sethian. Fronts propagating with curvature-dependent speed: Algorithms based on Hamilton-Jacobi formulations. *Journal of Computational Physics*, 79(1):12 – 49, 1988.

[114] B. R. Parizek, K. Christianson, S. Anandakrishnan, R. B. Alley, R. T. Walker, R. A. Edwards, D. S. Wolfe, G. T. Bertini, S. K. Rinehart, R. A. Bindschadler, and S. M. J. Nowicki. Dynamic (in)stability of Thwaites Glacier, West Antarctica. *Journal of Geophysical Research: Earth Surface*, 118(2):638–655, 2013.

[115] F. Pattyn. A new three-dimensional higher-order thermomechanical ice sheet model: Basic sensitivity, ice stream development, and ice flow across subglacial lakes. *Journal of Geophysical Research*, 108(B8):1–15, 2003.

[116] F. Pattyn. Sea-level response to melting of Antarctic ice shelves on multi-centennial timescales with the fast Elementary Thermomechanical Ice Sheet model (f.ETISh v1.0). *The Cryosphere*, 11(4):1851–1878, 2017.

[117] F. Pattyn, A. Huyghe, S. De Brabander, and B. De Smedt. Role of transition zones in marine ice sheet dynamics. *Journal of Geophysical Research: Earth Surface*, 111(F2):1–10, 2006.

[118] F. Pattyn, L. Perichon, G. Durand, L. Favier, O. Gagliardini, R. C. A. Hindmarsh, T. Zwinger, T. Albrecht, S. Cornford, D. Docquier, J. J. Fürst, D. Goldberg, G. H. Gudmundsson, A. Humbert, M. Hütten, P. Huybrechts, G. Jouvet, T. Kleiner, E. Larour, D. Martin, M. Morlighem, A. J. Payne, D. Pollard, M. Rückamp, O. Rybak, H. Seroussi, M. Thoma, and N. Wilkens. Grounding-line migration in plan-view marine ice-sheet models: results of the ice2sea MISMIP3d intercomparison. *Journal of Glaciology*, 59(215):410–422, 2013.

[119] F. Pattyn, C. Schoof, L. Perichon, R. C. A. Hindmarsh, E. Bueler, B. de Fleurian, G. Durand, O. Gagliardini, R. Gladstone, D. Goldberg, G. H. Gudmundsson, P. Huybrechts, V. Lee, F. M. Nick, A. J. Payne, D. Pollard, O. Rybak, F. Saito, and A. Vieli. Results of the Marine Ice Sheet Model Intercomparison Project, MISMIP. *The Cryosphere*, 6(3):573–588, 2012.

[120] M. Petrini, F. Colleoni, N. Kirchner, A. L. C. Hughes, A. Camerlenghi, M. Rebesco, R. G. Lucchi, E. Forte, R. R. Colucci, and R. Noormets. Interplay of grounding-line dynamics and sub-shelf melting during retreat of the Bjørnøyrenna Ice Stream. *Scientific Reports*, 8(7196):1–9, 2018.

[121] E. L. Poelking, A. M. Andrade, G. B. T. G. Vieira, C. E. G. R. Schaefer, and E. I. Fernandes Filho. Variações da frente da geleira Polar Club, Península Potter (ilha Rei George, Antártica Marítima) entre 1986 e 2011. *Revista Brasileira de Meteorologia*, 29:379–388, 09 2014.

[122] D. Pollard and R. M. DeConto. Modelling West Antarctic Ice Sheet growth and collapse through the past five million years. *Nature*, 458:329–332, 2009.

[123] D. Pollard and R. M. DeConto. Description of a hybrid ice sheet-shelf model, and application to Antarctica. *Geoscientific Model Development*, 5(5):1273–1295, 2012.

[124] S. C. B. Raper and R. J. Braithwaite. Glacier volume response time and its links to climate and topography based on a conceptual model of glacier hypsometry. *The Cryosphere*, 3(2):183–194, 2009.

[125] J. Reinders and J. Jeffers. *High Performance Parallelism Pearls*, volume 2. Morgan Kaufmann, Waltham, MA, USA, 2015.

[126] R. R. Ribeiro, E. Ramirez, J. C. Simões, and A. Machaca. 46 years of environmental records from the Nevado Illimani glacier group, Bolivia, using digital photogrammetry. *Annals of Glaciology*, 54(63):272–278, 2013.

[127] E. Rignot, G. Casassa, P. Gogineni, W. Krabill, A. Rivera, and R. Thomas. Accelerated ice discharge from the Antarctic Peninsula following the collapse of Larsen B ice shelf. *Geophysical Research Letters*, 31(18):1–4, 2004.

[128] E. Rignot, J. Mouginot, M. Morlighem, H. Seroussi, and B. Scheuchl. Widespread, rapid grounding line retreat of Pine Island, Thwaites, Smith, and Kohler glaciers, West Antarctica, from 1992 to 2011. *Geophysical Research Letters*, 41(10):3502–3509, 2014.

[129] C. Ritz, T. L. Edwards, G. Durand, A. J. Payne, V. Peyaud, and R. C. A. Hindmarsh. Potential sea-level rise from Antarctic Ice-Sheet instability constrained by observations. *Nature*, 528:115–118, 2015.

[130] C. Ritz, V. Rommelaere, and C. Dumas. Modeling the evolution of Antarctic Ice Sheet over the last 420,000 years: Implications for altitude changes in the Vostok region. *Journal of Geophysical Research: Atmospheres*, 106(D23):31943–31964, 2001.

[131] G. H. Roe, M. B. Baker, and F. Herla. Centennial glacier retreat as categorical evidence of regional climate change. *Nature Geoscience*, 10:95–101, 2017.

[132] T. D. Santos, P. R. B. Devloo, J. C. Simões, M. Morlighem, and H. Seroussi. Adaptive mesh refinement applied to grounding line and ice front dynamics. In *EGU General Assembly 2018*, volume 20. Geophysical Research Abstracts, Vienna, Austria, 2018.

[133] C. Schoof. On the mechanics of ice-stream shear margins. *Journal of Glaciology*, 50(169):208–218, 2004.

[134] C. Schoof. The effect of cavitation on glacier sliding. *Proceedings of the Royal Society of London A: Mathematical, Physical and Engineering Sciences*, 461(2055):609–627, 2005.

[135] C. Schoof. A variational approach to ice stream flow. *Journal of Fluid Mechanics*, 556:227–251, 2006.

[136] C. Schoof. Ice sheet grounding line dynamics: Steady states, stability, and hysteresis. *Journal of Geophysical Research: Earth Surface*, 112(F3):1–19, 2007.

[137] C. Schoof. Marine ice-sheet dynamics. Part 1. the case of rapid sliding. *Journal of Fluid Mechanics*, 573:27–55, 2007.

[138] H. Seroussi, M. Morlighem, E. Larour, E. Rignot, and A. Khazendar. Hydrostatic grounding line parameterization in ice sheet models. *The Cryosphere*, 8(6):2075–2087, 2014.

[139] H. Seroussi, M. Morlighem, E. Rignot, J. Mouginot, E. Larour, M. Schodlok, and A. Khazendar. Sensitivity of the dynamics of Pine Island Glacier, West Antarctica, to climate forcing for the next 50 years. *The Cryosphere*, 8(5):1699–1710, 2014.

[140] H. Seroussi, Y. Nakayama, E. Larour, D. Menemenlis, M. Morlighem, E. Rignot, and A. Khazendar. Continued retreat of Thwaites Glacier, West Antarctica, controlled by bed topography and ocean circulation. *Geophysical Research Letters*, 44(12):6191–6199, 2017.

[141] J. A. Sethian. Evolution, implementation, and application of level set and fast marching methods for advancing fronts. *Journal of Computational Physics*, 169(2):503 – 555, 2001.

[142] A. Shepherd, E. R. Ivins, G. A, V. R. Barletta, M. J. Bentley, S. Bettadpur, K. H. Briggs, D. H. Bromwich, R. Forsberg, N. Galin, M. Horwath, S. Jacobs, I. Joughin, M. A. King, J. T. M. Lenaerts, J. Li, S. R. M. Ligtenberg, A. Luckman, S. B. Luthcke, M. McMillan, R. Meister, G. Milne, J. Mouginot, A. Muir, J. P. Nicolas, J. Paden, A. J. Payne, H. Pritchard, E. Rignot, H. Rott, L. S. Sørensen, T. A. Scambos, B. Scheuchl, E. J. O. Schrama, B. Smith, A. V. Sundal, J. H. van Angelen, W. J. van de Berg, M. R. van den Broeke, D. G. Vaughan, I. Velicogna, J. Wahr, P. L. Whitehouse, D. J. Wingham, D. Yi, D. Young, and H. J. Zwally. A reconciled estimate of ice-sheet mass balance. *Science*, 338(6111):1183–1189, 2012.

[143] J. C. Simões. Glossário da língua portuguesa da neve, do gelo e termos correlatos. *Pesquisa Antártica Brasileira*, 4:119–154, 2004.

[144] J. C. Simões, U. F. Bremer, F. E. Aquino, and F. A. Ferron. Morphology and variations of glacial drainage basins in the King George Island ice field, Antarctica. *Annals of Glaciology*, 29:220–224, 1999.

[145] J. C. Simões, N. Dani, U. F. Bremer, F. E. Aquino, and J. Arigony-Neto. Small cirque glaciers retreat on Keller Peninsula, Admiralty Bay, King George Island, Antarctica. *Pesquisa Antártica Brasileira*, 4:49–56, 2004.

[146] L. A. Stearns and C. J. van der Veen. Friction at the bed does not control fast glacier flow. *Science*, 361(6399):273–277, 2018.

[147] B. Szabó and I. Babuška. *Finite Element Analysis*. John Wiley & Sons, USA, 1991.

[148] R. Thomas. The dynamics of marine ice sheet. *Journal of Glaciology*, 24(90):167–177, 1979.

[149] J. Todd, P. Christoffersen, T. Zwinger, P. Råback, N. Chauché, D. Benn, A. Luckman, J. Ryan, N. Toberg, D. Slater, and A. Hubbard. A full-Stokes 3-d calving model applied to a large Greenlandic glacier. *Journal of Geophysical Research: Earth Surface*, 123(3):410–432, 2018.

[150] V. C. Tsai, A. L. Stewart, and A. F. Thompson. Marine ice-sheet profiles and stability under Coulomb basal conditions. *Journal of Glaciology*, 61(226):205–215, 2015.

[151] D. G. Vaughan, J. C. Comiso, I. Allison, J. Carrasco, G. Kaser, R. Kwok, P. Mote, T. Murray, F. Paul, J. Ren, E. Rignot, O. Solomina, K. Steffen, and T. Zhang. Observations: Cryosphere. In T. F. Stocker, D. Qin, G.-K. Plattner, M. Tignor, S. K. Allen, J. Boschung, A. Nauels, Y. Xia, V. Bex, and P. M. Midgley, editors, *Climate Change 2013: The Physical Science Basis. Contribution of Working Group I to the Fifth Assessment Report of the Intergovernmental Panel on Climate Change*, pages 317–382. Cambridge University Press, Cambridge, United Kingdom and New York, NY, USA, 2013.

[152] D. G. Vaughan, H. F. J. Corr, F. Ferraccioli, N. Frearson, A. O'Hare, D. Mach, J. W. Holt, D. D. Blankenship, D. L. Morse, and D. A. Young. New boundary conditions for the West Antarctic Ice Sheet: Subglacial topography beneath Pine Island Glacier. *Geophysical Research Letters*, 33(9), 2006.

[153] A. Vieli and A. J. Payne. Assessing the ability of numerical ice sheet models to simulate grounding line migration. *Journal of Geophysical Research: Earth Surface*, 110(F1):1–18, 2005.

[154] P. Šolín, J. Červený, and I. Doležel. Arbitrary-level hanging nodes and automatic adaptivity in the hp-FEM. *Mathematics and Computers in Simulation*, 77(1):117–132, 2008.

[155] J. Weertman. On the sliding of glaciers. *Journal of Glaciology*, 3(21):33–38, 1957.

[156] J. Weertman. Stability of the junction of an ice sheet and an ice shelf. *Journal of Glaciology*, 13(67):3–11, 1974.

[157] A. V. Wilchinsky and V. A. Chugunov. Ice-stream-ice-shelf transition: theoretical analysis of two-dimensional flow. *Annals of Glaciology*, 30:153–162, 2000.

[158] A. V. Wilchinsky and V. A. Chugunov. Modelling ice flow in various glacier zones. *Journal of Applied Mathematics and Mechanics*, 65(3):479 – 493, 2001.

[159] D. J. Wingham, D. W. Wallis, and A. Shepherd. Spatial and temporal evolution of Pine Island Glacier thinning, 1995–2006. *Geophysical Research Letters*, 36(17):1–5, 2009.

[160] O. C. Zienkiewicz and R. L. Taylor. *The Finite Element Method*, volume 1. Butterworth-Heinemann, Woburn, MA, USA, 5th edition, 2000.

[161] O. C. Zienkiewicz and J. Z. Zhu. A simple error estimator and adaptive procedure for practical engineerng analysis. *International Journal for Numerical Methods in Engineering*, 24(2):337–357, 1987.

[162] O. C. Zienkiewicz and J. Z. Zhu. The superconvergent patch recovery and a posteriori error estimates. Part 1: The recovery technique. *International Journal for Numerical Methods in Engineering*, 33(7):1331–1364, 1992.

[163] O. C. Zienkiewicz and J. Z. Zhu. The superconvergent patch recovery and a posteriori error estimates. Part 2: Error estimates and adaptivity. *International Journal for Numerical Methods in Engineering*, 33(7):1365–1382, 1992.

Appendix A

Finite element method: a brief overview

The understanding of many physical problems requires the solution of partial differential equations that represents, in general, physical laws of conservations (mass, momentum, energy, etc). The analytical solution of these differential equations is restricted to simple domains and regular boundary conditions and forces. The solutions on real domains with non-regular boundary conditions and external forces are only obtained using numerical methods, e.g., finite differences, finite volumes, finite elements, etc. Here, we describe a brief introduction to finite element method, following the works of [111, 147, 2, 160].

The finite element method is a numerical scheme for obtaining approximate solutions to boundary-value problems [111, p.1]. In this method, the domain is divided into finite number of subdomains, the finite elements, and the approximate solution is constructed over these elements using variational concepts. To illustrate the main idea of the method, we start with a simple boundary-value problem [111, p.2]:

$$\begin{cases} -u'' + u = x \\ 0 \leq x \leq 1 \\ u(0) = 0 \\ u(1) = 0 \end{cases}, \tag{A.1}$$

where $u'' = d^2u/dx^2$.

The variational statement (also known as the 'weak statement') of problem A.1 is setting as: find a function u that both the differential equation and the boundary conditions are satisfied in a 'weak formulation' (a weighted average). The weak formulation is obtained by multiplying the differential equation by a test function v and then integrating it over the domain. For the simple problem A.1, we have:

$$\int_0^1 (-u'' + u)\, v \, dx = \int_0^1 xv \, dx \tag{A.2}$$

The function $v = v(x)$ is also referred as 'weight' function, and it could be any function that is well behaved in terms of integrals, that is, the integrals of the weak form A.2 exist[1]. For simplicity, we denote the set of such functions by H; we specify that the functions $v \in H$ are

[1]In fact, the specification of test functions is crucial to the finite element method theory.

smooth[2] and have zero values at $x = 0$ and $x = 1$. Then, the complete variational or weak statement of problem A.1 is: find u such that

$$\begin{cases} \displaystyle\int_0^1 (-u'' + u)\, v \, dx = \int_0^1 xv \, dx \\ \qquad\qquad\qquad\qquad \text{for all } v \in H \\ \qquad\qquad\qquad\qquad u(0) = 0 \\ \qquad\qquad\qquad\qquad u(1) = 0 \end{cases}. \tag{A.3}$$

We highlight two important points:

1. The weak formulation A.3 and the original (strong) formulation A.1 are equivalent: the solution of A.1 is the only solution of A.3;

2. The specification of the test functions (the set H) is a crucial component for constructing an acceptable weak formulation.

The point 2 leads a reformulation of the weak form A.3. In fact, the test function v in A.3 may not belong to the same set of functions $\bar{H}$ to which the solution u belongs. The set $\bar{H}$ is called as the 'class of trial functions' of problem A.3. The fact that H and $\bar{H}$ are not the same produces a non-symmetric formulation. For computational or theoretical purposes, a symmetric formulation is more suitable. We obtain an alternative symmetric weak formulation applying the integration-by-parts on the weak form A.3, considering that u and v are sufficiently smooth:

$$\int_0^1 -u''v \, dx = \int_0^1 u'v' \, dx - (u'v) \Big|_0^1 . \tag{A.4}$$

Considering that the test functions v vanish at the endpoints of the domain, we have that:

$$\int_0^1 -u''v \, dx = \int_0^1 u'v' \, dx, \tag{A.5}$$

for all admissible test functions v. This results in the following alternative variational problem: find $u \in H_0^1$ such that:

$$\begin{cases} \displaystyle\int_0^1 (u'v' + uv) \, dx = \int_0^1 xv \, dx \\ \qquad\qquad\qquad\qquad \text{for all } v \in H_0^1 \\ \qquad\qquad\qquad\qquad u(0) = 0 \\ \qquad\qquad\qquad\qquad u(1) = 0 \end{cases}. \tag{A.6}$$

where H_0^1 is a set of functions such that any function $v \in H_0^1$ has derivatives of order 1 which are square-integrable on the interval $0 \leq x \leq 1$ (superscript 1), and that $v(0) = v(1) = 0$ (subscript 0). We note that the same order of derivatives in both trial (u) and test (v) functions are present in this alternative weak formulation (A.6), then we can set $H = \bar{H} = H_0^1$. This leads to a symmetric formulation[3]. It is important to highlight that the point 1 described above still

[2] 'Smooth' means that the function derivatives are always continuous.

[3] The symmetry is clear below.

holds for this new weak formulation: any solution satisfying the original problem A.1 satisfies the weak form A.6. However, we have progressively weakened the smoothness requirements on the solution u, since the weak form A.4 contains second derivative whereas the form A.6 contains only the first derivative of u. We shall refer to form A.6 as the (desired) variational or weak formulation of the problem A.1.

The set H_0^1 of test and trial functions is defined such that the integral in the form A.6 exists, i.e., limiting to functions that satisfy the boundary conditions and are regular on the domain ensures that the integral makes sense. If u and v are irregular, certainly their derivatives are even less regular and then the integration of the term $u'v'$ may not exist. The choice of functions which derivatives of order 1 are square-integrable is based on the following: assuming that $v = u$, then v'^2 must be smooth enough for its integral to be calculated. The condition of square integrability is more restrictive than that of integrability. For example, the function $v(x) = x^{-1/2}$ is integrable over $0 \leq x \leq 1$ but v^2 is not. Functions satisfying this condition are said to have square-integrable first derivatives. Therefore, any function v belongs to H_0^1 if

$$\begin{aligned} \int_0^1 (v')\ dx < \infty \\ v(0) = 0 \\ v(1) = 0 \end{aligned} \tag{A.7}$$

Two additional properties of the set H_0^1 play an important role in the construction of approximation of solution u:

1. H_0^1 is a linear space. This means that any linear combination of functions in H_0^1 also belongs to H_0^1; e.g., if $v_1 \in H_0^1$ and $v_2 \in H_0^1$, then defining $v_3 = \alpha \cdot v_1 + \beta \cdot v_2$, we have $v_3 \in H_0^1$, for arbitrary constants α and β;

2. H_0^1 is infinite-dimensional. This means that any function $v \in H_0^1$ is only uniquely defined by an infinite number of parameters; e.g., in the Fourier Series Theory, we can write a function $v(x)$ as $v(x) = \sum_{i=1}^{\infty} \beta_i \Psi_i(x)$, where $\Psi_i(x) = \sqrt{2} \sin i\pi x$, $i = 1, 2, 3, \ldots$, and β_i are scalar coefficients; then, the function $v(x)$ is defined through infinite parameters β_i.

Through these 2 properties of H_0^1, we can represent any test function $v \in H_0^1$ as a linear combination:

$$v(x) = \sum_{i=1}^{\infty} \beta_i \Phi_i(x), \tag{A.8}$$

where $\Phi_i(x)$ are given to have this representation of v. A set of functions $\{\Phi_1, \Phi_2, \Phi_3, \ldots\}$ with this property is called 'basis' of H_0^1, and the functions Φ_i are called 'basis functions'.

If the series A.8 is truncated, we have a finite representation of v:

$$v_N(x) = \sum_{i=1}^{N} \beta_i \Phi_i(x), \tag{A.9}$$

where N is any arbitrary positive integer. The N basis functions $\{\Phi_1, \Phi_2, \ldots, \Phi_N\}$ define an N-dimensional subspace $H_0^{1,N}$ of H_0^1.

The Galerkin's method seeks an approximate solution to the weak form A.6 in a finite-dimensional $H_0^{1,N}$ of the space H_0^1 rather than in the entire space H_0^1. That means that we are seeking for an approximate solution u_N in the subspace $H_0^{1,N}$ (i.e., $u_N \in H_0^{1,N}$) of such form:

$$u_N(x) = \sum_{i=1}^{N} \alpha_i \Phi_i(x). \tag{A.10}$$

Then, the variational statement of the approximate problem is: find $u_N \in H_0^{1,N}$ such that:

$$\begin{cases} \displaystyle\int_0^1 \left(u_N' v_N' + u_N v_N\right)\, dx = \int_0^1 x v_N\, dx \\ \qquad\qquad \text{for all } v_N \in H_0^{1,N} \\ u_N(0) = 0 \\ u_N(1) = 0 \end{cases}. \tag{A.11}$$

Although the boundary conditions $u_N(0) = 0$ and $u_N(1) = 0$ in the variational statement are redundant, since this specification is included in the space $H_0^{1,N}$ (definition A.7), we are keeping them here as a reminder of the boundary-problem.

The approximate solution u_N is completely determined once the N coefficients α_i in A.10 are known, since the N basis functions Φ_i of $H_0^{1,N}$ are known in advance and the coefficient β_i of the test function v_N are arbitrary. The coefficients α_i are called 'degrees of freedom' of the weak statement A.11. Introducing A.9 and A.10 into the weak form A.11, we have:

$$\begin{gathered} \displaystyle\int_0^1 \left[\frac{d}{dx}\left(\sum_{i=1}^{N} \beta_i \Phi_i\right)\frac{d}{dx}\left(\sum_{j=1}^{N} \alpha_j \Phi_j\right) + \left(\sum_{i=1}^{N} \beta_i \Phi_i\right)\left(\sum_{j=1}^{N} \alpha_j \Phi_j\right)\right] dx \\ = \int_0^1 x \sum_{i=1}^{N} \beta_i \Phi_i\, dx \\ \text{for all } \beta_i,\ i = 1,\ 2,\ \ldots,\ N \end{gathered}. \tag{A.12}$$

Factoring A.12 in terms of coefficients β_j yields:

$$\begin{gathered} \displaystyle\sum_{i=1}^{N} \beta_i \left\{\sum_{j=1}^{N} \left[\int_0^1 \left(\Phi_i' \Phi_j' + \Phi_i \Phi_j\right)\, dx\right] \alpha_j - \int_0^1 x \Phi_i\, dx\right\} = 0 \\ \text{for all } \beta_i,\ i = 1,\ 2,\ \ldots,\ N \end{gathered}. \tag{A.13}$$

Rewriting A.13 in a more compact form yields:

$$\begin{gathered} \displaystyle\sum_{i=1}^{N} \beta_i \left(\sum_{j=1}^{N} K_{ij} \alpha_j - F_i\right) = 0 \\ \text{for all } \beta_i,\ i = 1,\ 2,\ \ldots,\ N \end{gathered}, \tag{A.14}$$

where:

$$\begin{aligned} K_{ij} &= \int_0^1 \left(\Phi_i' \Phi_j' + \Phi_i \Phi_j\right) \, dx \\ F_i &= \int_0^1 x \Phi_i \, dx \\ i,\, j &= 1,\, 2,\, \ldots,\, N \end{aligned} \quad , \tag{A.15}$$

where $\mathbf{K} = K_{ij}$ and $\mathbf{F} = F_i$ are commonly called 'stiffness matrix' and 'load vector', respectively, for problem A.11 and for basis functions $\Phi_i \in H_0^{1\,N}$. Since the basis functions Φ_i are known, both $\mathbf{K}$ and $\mathbf{F}$ can be computed by A.15. Parameters β_i can be chosen in such a way that a linear system arises:

$$\begin{aligned} \sum_{j=1}^{N} K_{ij} \alpha_j - F_i = 0 \\ i = 1,\, 2,\, \ldots,\, N \end{aligned} \quad . \tag{A.16}$$

As the basis functions Φ_i have been chosen to be independent, equations A.16 are also independent. Thus, the stiffness matrix $\mathbf{K}$ is invertible, which means that $\boldsymbol{\alpha} = \alpha_j$ are uniquely determined by inverting $\mathbf{K}$:

$$\boldsymbol{\alpha} = \mathbf{K}^{-1}\mathbf{F}. \tag{A.17}$$

Once the coefficients $\boldsymbol{\alpha}$ are determined, the approximate solution u_N is defined by introducing A.17 in A.10.

We highlight that the stiffness matrix $\mathbf{K}$ obtained above is symmetric since (through its definition A.15):

$$K_{ij} = \Phi_i' \Phi_j' + \Phi_i \Phi_j = K_{ji} = \Phi_j' \Phi_i' + \Phi_j \Phi_i. \tag{A.18}$$

The symmetry of $\mathbf{K}$ here occurs due to the weak formulation A.6 and to the fact the spaces of trial functions and test functions are the same. It is clear that if we had used the previous weak form A.3, $\mathbf{K}$ would not be symmetric.

We can point out some reasons about the choice of a symmetric variational formulation:

1. The symmetric formulation, in general, leads to a symmetric stiffness matrix, which means a reducing in the computational effort for obtaining the unknown coefficients and, consequently, the approximate solution of the problem;

2. It can be shown that, using a symmetric formulation, the Galerkin's method provides the best possible approximation of the solution u in the subspace $H_0^{1,\,N}$;

3. In the symmetric formulation, both spaces of the trial and test functions coincide. Therefore, only one set of basis functions Φ_i of the subspace $H_0^{1,\,N}$ need to be built.

Another important observation is that the quality of the approximation u_N depends completely on the choice of the basis functions Φ_i, or in a general aspect, of the subspace $H_0^{1,\,N}$. Once the basis are chosen, the determination of the coefficients α_i is a computational task.

The systematic construction of basis functions are not explicitly provided by Galerkin's method, mainly in cases where irregular geometries are present (in 2D/3D). A general and systematic technique for constructing the basis functions are given by the finite element method: the basis functions Φ_i are defined piecewise over subregions of the domain called 'finite elements'. In general, the basis Φ_i are chosen to be very simple functions such as low order polynomials.

The first step in the finite element method is dividing the domain (Ω) $0 \leq x \leq 1$ in a finite number of elements, Ω_i, $i = 1, 2, \ldots$, whose lengths are denoted by h_i. The elements are linked by a shared point called as 'vertex' (also as 'node'). The collection of elements and vertices is referred as a 'mesh' or 'geometric mesh'. As an example, one can divide the domain in four elements of equal sizes (then $h_i = h = 1/4$, $i = 1, \ldots, 4$) such that the vertices' coordinates are:

$$\begin{matrix} x_i = (i-1) \cdot 1/4 \\ i = 1, 2 \ldots, 5 \end{matrix} . \tag{A.19}$$

Then, the elements are defined as:

$$\begin{matrix} \Omega_i = \{x_i, x_{1+1}\} \\ i = 1, 2 \ldots, 4 \end{matrix} . \tag{A.20}$$

Once the geometric mesh is defined, we can generate the basis functions on this mesh. The main criteria of the finite element method are such that the basis functions Φ_i should be:

- Generated by simple functions defined element by element over the mesh;
- Smooth enough to be members of the space H_0^1;
- Chosen in such a way that the parameters α_i defining the approximate solution u_N are exactly the values of $u_N(x)$ at the vertices (nodes).

Following these criteria, a set of basis functions can be defined as:

$$\Phi_i(x) = \begin{cases} (x - x_i)/h_i & \text{for } x_i \leq x \leq x_{i+1} \\ (x_{i+2} - x)/h_{i+1} & \text{for } x_{i+1} \leq x \leq x_{i+2} \\ 0 & \text{for } x \leq x_i \text{ and } x \geq x_{i+2} \end{cases} . \tag{A.21}$$

with $i = 1, 2, 3$ and $h_i = x_{i+1} - x_i$ the elements' lengths. The first derivatives of the basis functions are:

$$\Phi_i'(x) = \begin{cases} 1/h_i & \text{for } x_i < x < x_{i+1} \\ -1/h_{i+1} & \text{for } x_{i+1} < x < x_{i+2} \\ 0 & \text{for } x < x_i \text{ and } x > x_{i+2} \end{cases} . \tag{A.22}$$

It is not hard to verify that these basis $\Phi_i(x)$, $i = 1, 2, 3$ follow the criteria shown above. Once the basis are defined, we can return to the Galerkin's approximation of the variational boundary-value problem. Since the basis is chosen such that $\alpha_i = u_i$, the approximate solution u_N is written as:

$$u_N(x) = \sum_{i=1}^{N} u_i \Phi_i(x), \tag{A.23}$$

where $N = 3$ in this case.

The first step is the computation of the stiffness matrix A.15 (also called 'assembly'), which can be integrated element-by-element:

$$\begin{aligned} K_{ij} &= \int_{x_1}^{x_2} \left(\Phi_i' \Phi_j' + \Phi_i \Phi_j \right) \, dx \\ &+ \int_{x_2}^{x_3} \left(\Phi_i' \Phi_j' + \Phi_i \Phi_j \right) \, dx \\ &+ \int_{x_3}^{x_4} \left(\Phi_i' \Phi_j' + \Phi_i \Phi_j \right) \, dx \\ &+ \int_{x_4}^{x_5} \left(\Phi_i' \Phi_j' + \Phi_i \Phi_j \right) \, dx \\ &= \sum_{e=1}^{4} \int_{\Omega_e} \left(\Phi_i' \Phi_j' + \Phi_i \Phi_j \right) \, dx \\ &= \sum_{e=1}^{4} K_{ij}^e \\ i, \, j &= 1, \, 2, \, 3 \end{aligned} \quad , \tag{A.24}$$

where Ω_e are the domains of each element $e = 1, \, 2, \, 3, \, 4$ and:

$$K_{ij}^e = \int_{\Omega_e} \left(\Phi_i' \Phi_j' + \Phi_i \Phi_j \right) \, dx \tag{A.25}$$

is the element's stiffness matrix. Next step is the load vector computation, which is done by a similar way element-by-element:

$$\begin{aligned} F_i &= \sum_{e=1}^{4} \int_{\Omega_e} x \Phi_i \, dx \\ F_i &= \sum_{e=1}^{4} F_i^e \\ i &= 1, \, 2, \, 3 \end{aligned} \quad , \tag{A.26}$$

where:

$$F_i^e = \int_{\Omega_e} x \Phi_i \, dx \tag{A.27}$$

is the element's load vector.

The last computational is the integration of the element's stiffness matrix and element's load vector. This integration procedure can be done through some numerical integration technique (e.g., Gaussian quadrature), which is essential mainly in 2D/3D elements. In our example, the

integration process through each element yields:

$$\begin{aligned}\mathbf{K}^1 &= \frac{1}{24}\begin{bmatrix} 98 & 0 & 0 \\ 0 & 0 & 0 \\ 0 & 0 & 0 \end{bmatrix}, \mathbf{K}^2 = \frac{1}{24}\begin{bmatrix} 98 & -95 & 0 \\ -95 & 98 & 0 \\ 0 & 0 & 0 \end{bmatrix}, \\ \mathbf{K}^4 &= \frac{1}{24}\begin{bmatrix} 0 & 0 & 0 \\ 0 & 0 & 0 \\ 0 & 0 & 98 \end{bmatrix}, \mathbf{K}^3 = \frac{1}{24}\begin{bmatrix} 0 & 0 & 0 \\ 0 & 98 & -95 \\ 0 & -95 & 98 \end{bmatrix},\end{aligned} \tag{A.28}$$

and:

$$\begin{aligned}\mathbf{F}^1 &= \frac{1}{96}\begin{bmatrix} 2 \\ 0 \\ 0 \end{bmatrix}, \mathbf{F}^2 = \frac{1}{96}\begin{bmatrix} 4 \\ 5 \\ 0 \end{bmatrix}, \\ \mathbf{F}^4 &= \frac{1}{96}\begin{bmatrix} 0 \\ 0 \\ 10 \end{bmatrix}, \mathbf{F}^3 = \frac{1}{96}\begin{bmatrix} 0 \\ 7 \\ 8 \end{bmatrix},\end{aligned} \tag{A.29}$$

where $\mathbf{K}^e = K^e_{ij}$ and $\mathbf{F}^e = F^e_i$. Then, the global stiffness matrix $\mathbf{K}$ and global load vector $\mathbf{F}$ are given by the assembly process:

$$\mathbf{K} = \mathbf{K}^1 + \mathbf{K}^2 + \mathbf{K}^3 + \mathbf{K}^4, \mathbf{F} = \mathbf{F}^1 + \mathbf{F}^2 + \mathbf{F}^3 + \mathbf{F}^4, \tag{A.30}$$

which yields to:

$$\begin{aligned}\mathbf{K} &= \frac{1}{24}\begin{bmatrix} 196 & -95 & 0 \\ -95 & 196 & -95 \\ 0 & -95 & 196 \end{bmatrix}, \\ \mathbf{F} &= \frac{1}{96}\begin{bmatrix} 6 \\ 12 \\ 18 \end{bmatrix}.\end{aligned} \tag{A.31}$$

The linear system is

$$\frac{1}{24}\begin{bmatrix} 196 & -95 & 0 \\ -95 & 196 & -95 \\ 0 & -95 & 196 \end{bmatrix}\begin{bmatrix} u_1 \\ u_2 \\ u_3 \end{bmatrix} = \frac{1}{96}\begin{bmatrix} 6 \\ 12 \\ 18 \end{bmatrix}. \tag{A.32}$$

whose solution is:

$$\mathbf{u} = \begin{bmatrix} u_1 \\ u_2 \\ u_3 \end{bmatrix} = \begin{bmatrix} 0.0352 \\ 0.0569 \\ 0.0505 \end{bmatrix}. \tag{A.33}$$

Finally, the approximate solution $u_N(x)$ of the boundary-value problem A.1 is:

$$u_N(x) = 0.0352\Phi_1(x) + 0.0569\Phi_2(x) + 0.0505\Phi_3(x), \tag{A.34}$$

where functions $\Phi_i(x)$ are given by A.21. A comparison between the exact solution of problem A.1 and the approximate solution A.34 is shown in Figure A.1.

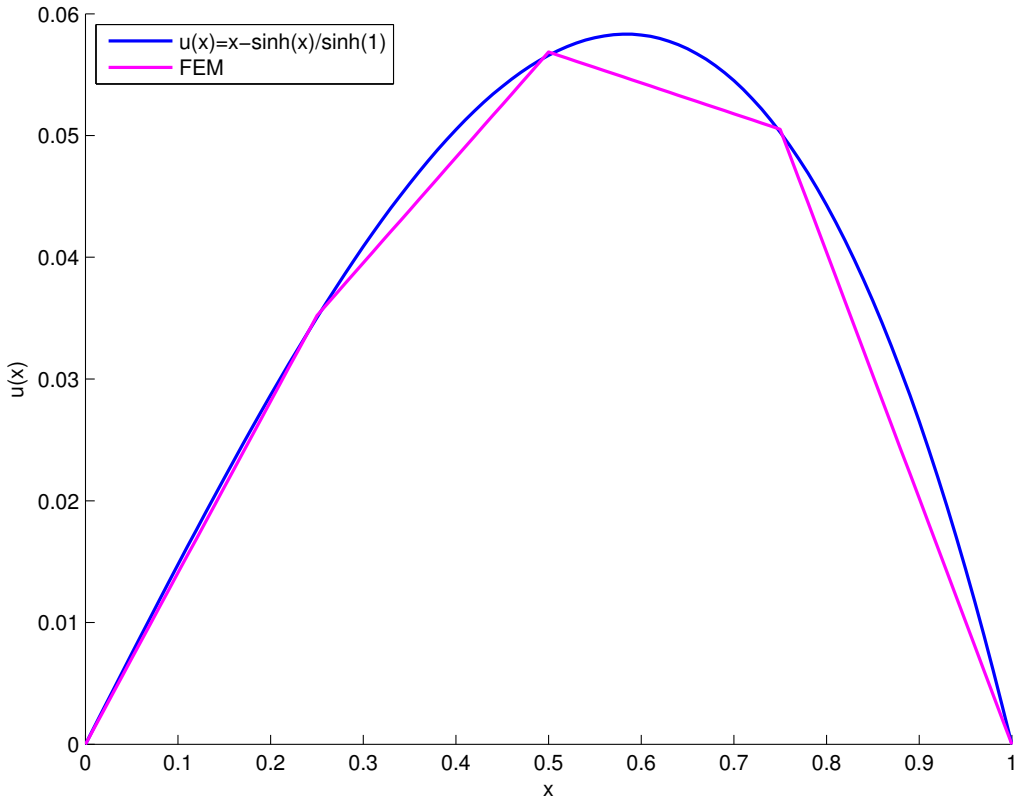

Figure A.1: Comparison between the exact solution and approximate solution of the boundary-value problem A.1. The approximate solution $u_N(x)$ is given by A.34.